



universität
wien

DISSERTATION / DOCTORAL THESIS

Titel der Dissertation /Title of the Doctoral Thesis

„Neuronal mechanisms implementing a hierarchy of
rhythmic movements in *C. elegans*“

verfasst von / submitted by

Oriana Ylida Salazar Thula, M.Sc.

angestrebter akademischer Grad / in partial fulfilment of the requirements for the degree of

Doctor of Philosophy (PhD)

Wien, 2022 / Vienna 2022

Studienkennzahl lt. Studienblatt /
degree programme code as it appears on the student
record sheet:

UA 794 685 490

Dissertationsgebiet lt. Studienblatt /
field of study as it appears on the student record sheet:

Molekulare Biologie

Betreut von / Supervisor:

Univ.-Prof. Dr. Manuel Zimmer

Table of Contents

Acknowledgements	3
1. Authorship and contributions	5
2. Summary	6
<i>Abstract</i>	6
<i>Zusammenfassung</i>	7
3. Introduction	8
3.1 <i>The organization of behavior</i>	8
3.2 <i>Behavioral hierarchies, past and present</i>	9
3.3 <i>Interrogation of neurobiological implementations of hierarchies</i>	10
3.4 <i>Locomotion and Central Pattern Generation</i>	11
3.5 <i>C. elegans, an ideal subject for the study of behavioral hierarchies and CPGs</i>	13
3.5.1 <i>Anatomy and function of the C. elegans nervous system</i>	14
3.5.2 <i>Neuronal population dynamics in C. elegans</i>	24
3.6 <i>Aims of this thesis</i>	25
4. Results	27
4.1. <i>Identifying candidate neurons to implement a behavioral hierarchy in C. elegans</i>	27
4.1.1. <i>Expanded experimental imaging setup allows for Whole-Nervous-System interrogation</i>	27
4.1.2. <i>Level I: Nervous-system-wide representation of behavior at the uppermost hierarchy level</i>	29
4.1.3. <i>Identifying candidate neuronal drivers for hierarchical levels II and III</i>	31
4.2. <i>B- and SMD motor neurons are required for propagated bends and head casts, respectively</i>	39
4.3. <i>Level I and II interaction: Upper hierarchical level toggles activity of middle- and lower-level neurons</i> ...	42
4.4. <i>Level II and III interaction: Investigating the relationship between SMD and B-MN activities</i>	43
4.4.1. <i>Correlations between B-MN and SMD and propagated-bends and head-casts</i>	43
4.4.2. <i>Phase nesting of B-MN and SMD activity</i>	45
4.4.3. <i>How are propagated bends and head casts coupled? Investigating the role of gap junction proteins in SMDV and VBO1 activity</i>	46
4.5. <i>Level I and II Interactions: Do lower hierarchical levels influence the global forward-reverse-turn cycle?</i> 52	
4.6. <i>Investigating network mechanisms of SMD modulation</i>	55
4.6.1. <i>Investigating network mechanisms of SMD modulation in REV command state</i>	56
4.6.2 <i>Mechanisms of SMD modulation in turn command state</i>	57
4.6.3. <i>Investigating network mechanisms of SMD modulation in FWD command state</i>	61
5. Discussion	63
5.1 <i>Research aims and key findings</i>	63
5.2. <i>Slow and global vs. fast and local dynamics</i>	64
5.3. <i>A hierarchy of states</i>	65
5.4. <i>Neuronal underpinnings of hierarchical relationships</i>	65
5.5. <i>Modulation of the hierarchy</i>	67

5.6. Modulation by the hierarchy.....	69
5.7. A model for Central Pattern Generation in forward locomotion.....	70
5.8. The hierarchical control of CPGs.....	71
5.9. Motor neurons that multitask.....	73
5.10. The regulation of behavioral state transitions.....	74
5.11. Further limitations and future perspectives.....	74
6. Materials and methods.....	78
6.1. Animal culture and animal strains.....	78
6.2. Population behavior assays.....	82
6.3. Ca ²⁺ imaging in immobilized animals.....	83
6.4. Simultaneous imaging of neuronal activity and behavior.....	85
6.5. Neuronal time series extraction from immobilized pan-neuronal imaging experiments.....	86
6.6. Neuronal identification (pan-neuronal imaging).....	87
6.7. Principal Component Analysis (PCA; immobilized pan-neuronal imaging).....	88
6.8. Neuronal time series extraction and behavior analysis (freely moving imaging).....	89
6.9. Propagation analysis and head-bend type classification (behavior assays and freely moving imaging)...	90
6.10. Quantifications and statistical analyses.....	90
6.10.1 Command state identification and quantification of command state durations (immobilized pan-neuronal imaging).....	91
6.10.2 Mean activity difference quantification.....	91
6.10.3 Peak frequency quantification (immobilized pan-neuronal imaging and freely moving imaging)....	91
6.10.4 Covariogram analysis (immobilized pan-neuronal imaging).....	93
6.10.5 Post-reversal SMD peak identification, amplitude quantification.....	94
6.10.6 Coincident peak categorization and quantification (<i>acc-1</i> immobilized imaging).....	95
6.10.7 Triggered averages of SMD activity.....	95
6.10.8 Cycle period quantifications (immobilized panneuronal and freely moving imaging).....	95
6.10.9 Reconstruction quality for neuronal subsets (pan-neuronal imaging).....	96
6.10.10 Polar histogram statistics.....	96
7. References.....	97

Acknowledgements

There are so many people to thank for their scientific and personal contributions to this journey. First, I'd like to thank my supervisor, **Manuel**, for his scientific support, enthusiasm and guidance, without which this thesis would not have been possible. You have taught me to always strive for excellence and I am glad to have had such an example of scientific rigor, critical thinking and excitement for science. Thank you for always fostering an environment where we could all do great science and have a lot of fun in the process.

Thank you to all the present and past members of the Zimmer lab. I'm so happy I got to know all of you! Defending is hard when you have such amazing colleagues to say goodbye to. **Harris**, I was lucky to have worked with such an amazing scientist and I'll always have fond memories of us staying in the lab late, ordering food to the IMP, doing experiments, discussing ideas and laughing together. I admire your brilliance, your work ethic and your dedication. Thank you for bringing out the best in me. **Ulises** and **Itamar**, I am grateful for our friendship, our scientific and not-scientific discussions and our coffee excursions. Thank you for being there in the good and bad times, for broadening my horizons, for the always-interesting chats, and for being examples of smart, dedicated, and passionate scientists. Thank you **Tina, Harris, Susanne, Annika, Julia** and **Rich**, for teaching me all I needed to know in the lab and for making it such a welcoming environment. Special thanks to **Rich** for his constant support, for all the fun, and for reminding me that things are not always as bad as they may seem. Thank you, **Kerem**, for your support especially during the writing of this thesis, your infectious laugh and your exemplary chillness. For their companionship, I'd like to thank current lab members **Anton, Charlie, Fabio, Itamar, Jalaja, Johannes, Josefine, Julia, Lukas, Mara, Paul, Pedro, Rich, Stephanie**, and **Ulises**; and past lab members **Tina, Susanne, Ingrid, Harris, Annika, Saul, Luka, Rebecca, Lars, Daniel, Tomas Eichler, Tomas Kazmar, Niklas, Marc**, and anyone I've overlapped with during the last 6 years and 4 (+2) months that I may have missed.

I'm also very grateful to my thesis committee members, **Prof. Luisa Cochella, Wulf Haubensak** and **Max Jösch** for their valuable input throughout my PhD.

Gracias a los Amiguitos, **Ana, Ulises y Lesly**, for all the food we made and shared, the conversations, the laughs, the music, and for showing up when I really needed it. Thank you, **Igor**, for being a wonderful friend and the co-founder of the unofficial VBCinema Club. I'm glad 100% of my time in Vienna has been shared with you. Thank you, **Dhaarsi**, for all the fun times, for being an example of dedication and perseverance, and for infecting me with the SuperCycle bug. Thank you to

Karina, Ivanna, and Fionna, for being my hype women. Gracias a las **Femigrantes** por enriquecer mi vida; por el espacio para crear, aprender, discutir y mejorar.

This thesis is dedicated to a few important people that are not here to thank personally. To my great-grandmother **Idilia**, my grandma **Grace** and my aunt **Kathy**, who were a constant source of love and encouragement in my life and always believed I'm smarter than I am. Their support helped me believe I can do anything, and I wish they were here for the end of this chapter. To my late father **Richard**, who gifted me the most loving family I could have had, and to my step-father **Rafael**, whose love and parenting, though cut short, I'll always be grateful for.

Most importantly, I'd like to thank and dedicate this thesis to my mother, **Aleya**, and my brother, **Juan Andrés**. This thesis exists because of my mother's dedication to our education; any milestone I reach will be reached thanks to her love and sacrifice. Gracias, mamá, por tu apoyo y amor constante e incondicional, y por ser mi ejemplo a seguir. There are no words to express my gratitude towards my brother, who's been my biggest supporter, role model and companion since day one. Thank you for your love, for your support, and for never failing to make me laugh. Admiro tu gran corazón, tu inteligencia y tu sentido del humor. Gracias siempre, los amo.

An enormous thank you to **Mosti**, who has been there with me throughout this PhD. Thank you for everything. You are my biggest cheerleader, my rock, and you inspire me to be better every day. I am grateful for your love, care and unwavering support when things were difficult, and for having shared so many great moments together. I can't imagine having done this without you by my side.

1. Authorship and contributions

Text and figures cited and used from own work

Texts and figure panels in this thesis have in large parts been adapted or taken from the publication titled "Nested neuronal dynamics orchestrate a behavioral hierarchy across timescales" that I, Oriana Salazar Thula, have prepared together with co-first author Harris S. Kaplan, Niklas Khoss and Manuel Zimmer.

Contributions

All my gratitude to those whose work contributed to the experiments and data analysis presented in this thesis. Harris S. Kaplan performed all behavior assays and freely-moving Ca^{2+} imaging experiments, as well as writing code for the covariogram-, behavioral-, and freely-moving Ca^{2+} imaging analysis (Figs. 4.8-4.9, 4.14-4.17b, 4.18-4.19, 4.24a-b, 4.25, 4.28-4.29). Data preparation and data analysis of freely-moving AIB::hisCl inhibition, *tdc-1* and *lgc-55* mutant imaging was done by Harris and I. The acquisition of following whole-brain imaging datasets was done with the help of following students, which I supervised: Internship student Lars Kopel acquired most *acc-1 lgc-47*, *acc-1 lgc-47* and RIB::hisCl whole-brain imaging recordings, some recordings were acquired by me; *acc-1* data preparation was done by Lars, *acc-1* data analysis was done by Lars and I (Fig. 4.31). Data preparation and analysis of *lgc-47*, *acc-1 lgc-47* and RIB::hisCl recordings was done by me. Internship student Josefine Sophie Meyer and I acquired and prepared the *unc-9* whole-brain imaging data for analysis (Fig. 4.23); data analysis was done by me. Additionally, MSc student Rebecca Kresnik acquired *unc-7 unc-9* mutant whole-brain imaging recordings and performed the data preparation/curation. Data analysis was done by me. I acquired all immobilized whole-nervous-system imaging data, whole-brain RIS::hisCl, VNC_{ACh} ::hisCl and SMD::hisCl whole-brain imaging data, as well as performed all data preparation/curation of these datasets. I wrote the code for all immobilized Ca^{2+} imaging analysis and performed all analyses of immobilized imaging data.

2. Summary

Abstract

It has long been proposed by ethologists that animal behavior is organized hierarchically across timescales, where longer-lasting behavioral sequences consist of distinct, faster-timescale behavioral motifs. Our previous work found such a behavioral hierarchy in the roundworm *C. elegans*, where food search behavior mainly consists of switches between forward- and backward-directed locomotion. Crucially, within the forward locomotion state, we found dorsal/ventral body undulations and faster-timescale head flicks nested within them. This thesis investigates the neuronal mechanisms underlying this behavioral organization. Specifically, I aimed to identify the neurons that drive these behaviors, how the hierarchy is implemented in the nervous system and how neuronal activity is modulated depending on the overarching behavioral state. To do so, I employed pan-neuronal imaging of immobilized worms at single-cell resolution, combined with genetic perturbations and acute neuronal inhibition.

Our findings reveal how neuronal circuits dynamically organize behavior in a hierarchical manner: On a slower timescale, global network activity drives the alternation of forward/backward movement commands. Within the forward state, motor neuron oscillators drive full-body undulations to propel the animal forward. Additionally, faster-frequency neuronal oscillations drive head flicks within specific phases of the body undulation cycle, a relationship we term phase-nesting. These behaviors are driven by the activity of the SMD and DB motoneurons. The fact that they are active even in the absence of patterned input strongly suggests their involvement in intrinsic central pattern generation. Further, our data suggests that the SMD neurons are modulated by the overarching behavioral state, causing different behaviors. Finally, their activity can be altered by perturbing chemical and electrical neurotransmission.

In conclusion, this work shows that phase-nested oscillations are a recurring motif of the *C. elegans* nervous system, and that neurons are modulated to implement different behaviors within the framework of a behavioral hierarchy.

Zusammenfassung

Ethologen gehen seit langem davon aus, dass das Verhalten von Tieren über Zeitskalen hinweg hierarchisch organisiert ist, wobei länger andauernde Verhaltenssequenzen aus verschiedenen, schneller ablaufenden Verhaltensmotiven bestehen. In unserer früheren Arbeit haben wir eine solche Verhaltenshierarchie beim Fadenwurm *C. elegans* gefunden, dessen Verhalten bei der Nahrungssuche hauptsächlich aus dem Wechsel zwischen vorwärts- und rückwärtsgerichteter Fortbewegung besteht. Entscheidend ist, dass wir innerhalb der vorwärtsgerichteten Fortbewegung dorsale/ventrale Körperwellen und darin eingebettete Kopfbewegungen mit schnellerer Zeitskala gefunden haben. In dieser Arbeit werden die neuronalen Mechanismen untersucht, die dieser Verhaltensorganisation zugrunde liegen. Insbesondere wollte ich die Neuronen identifizieren, die diese Verhaltensweisen steuern, und herausfinden, wie die Hierarchie im Nervensystem umgesetzt wird und wie die neuronale Aktivität in Abhängigkeit vom übergeordneten Verhaltenszustand moduliert wird. Zu diesem Zweck verwendete ich pan-neuronale Bildgebung von immobilisierten Würmern mit Einzelzellauflösung, kombiniert mit genetischen Störungen und akuter neuronaler Hemmung.

Unsere Ergebnisse zeigen, wie neuronale Schaltkreise das Verhalten dynamisch in hierarchischer Weise organisieren: Auf einer langsameren Zeitskala steuert die globale Netzwerkaktivität den Wechsel zwischen Vorwärts- und Rückwärtsbewegungen. Im Vorwärtszustand treiben die Oszillatoren der Motoneuronen Ganzkörperwellen an, um das Tier vorwärts zu bewegen. Darüber hinaus treiben neuronale Oszillationen mit höherer Frequenz Kopfbewegungen in bestimmten Phasen des Körperwellenzyklus an, eine Beziehung, die wir als "phase nesting" bezeichnen. Diese Verhaltensweisen werden durch die Aktivität der SMD- und DB-Motoneuronen gesteuert. Die Tatsache, dass sie auch in Abwesenheit von gemustertem Input aktiv sind, deutet stark darauf hin, dass sie an der intrinsischen zentralen Mustergenerierung beteiligt sind. Darüber hinaus deuten unsere Daten darauf hin, dass die SMD-Neuronen durch den übergreifenden Verhaltenszustand moduliert werden und unterschiedliche Verhaltensweisen hervorrufen. Schließlich kann ihre Aktivität durch Störung der chemischen und elektrischen Neurotransmission verändert werden.

Zusammenfassend zeigt diese Arbeit, dass phasenverschachtelte Oszillationen ein wiederkehrendes Motiv des Nervensystems von *C. elegans* sind, und, dass die Neuronen moduliert werden, um verschiedene Verhaltensweisen im Rahmen einer Verhaltenshierarchie zu realisieren.

3. Introduction

3.1 The organization of behavior

Animal behavior is carried out over a wide span of timescales, from muscle contractions at the sub-second scale, to migratory flights lasting several days (Gill et al. 2009). The nervous system generates the neuronal activity to drive individual actions, as well as coordinating them across timescales to orchestrate behavioral strategies. Individual behaviors— as well as the neuronal networks that drive them— are studied extensively, and great efforts are made to map neuronal connections, characterize neuronal activity, and uncover the relationship between neuronal network activity to specific behaviors. It has been suggested that a greater understanding of how behavior works will be reached from distilling general explanatory principles of behavior at a higher level, rather than from the aforementioned efforts (R. Dawkins 1976). Although both approaches have value, such principles would help us understand how the nervous system not only drives individual actions, but how these actions are coordinated across timescales to orchestrate behavioral strategies.

But what does it mean to ‘understand behavior’? Dawkins proposed to look for principles to explain the mechanism of behavior on a ‘software’ level. This is reminiscent of Marr’s levels of analysis, who argued that we should analyze information processing systems – as is the nervous system – at different levels: Level 1 refers to the computational problem a system is solving, Level 2 is the algorithm used to solve the problem, and Level 3 corresponds to how the algorithm is implemented physically (Marr 1982). These levels of understanding should not be confused with the behavioral hierarchies that Dawkins proposed; we believe that a behavioral hierarchy would correspond to Marr’s Level 2, the understanding of the algorithm a system uses to solve a problem. So, to ‘understand behavior’ in Dawkins’ sense would correspond to understanding the computational problems a system is solving (Level 1) and the algorithms used to solve it (Level 2), without focusing on the details of their implementation (the ‘hardware’ implementation, Level 3). On the other hand, Marr argued that we must understand information processing systems at all three levels of analysis to reach true understanding.

Hierarchical organization has been proposed as a candidate principle for understanding behavior, and, more generally, the complexity of the brain, be it in the analysis of sensory data, the storage and retrieval of information, or the recognition of patterns in incoming data (M. Dawkins 1971). Briefly, a hierarchy can be described as a complex system that is composed of interrelated subsystems, which are themselves also composed of hierarchical sub-subsystems, and so forth, until a level of ‘elementary’ subsystems is reached (Simon 1962). What counts as ‘elementary’ is arbitrary and often defined by how ‘trivial’ further partitioning would be.

Hierarchies can be found almost everywhere we look: biological organisms are made up of organs, built by tissues, built by cells, composed of organelles; galaxy filaments are made up of superclusters, composed of galaxy clusters, composed of galaxy groups (such as the Local Group),

which host galaxies (such as the Milky Way); in language, sentences are composed of phrases, built by words, which can be further partitioned into morphemes, and phonemes. Thus, it has been theorized that hierarchical control could even form the foundations of a theory to ‘understand the nature of life itself’ (Pattee 1973).

3.2 Behavioral hierarchies, past and present

Classical and modern ethological studies

A hierarchy is, in essence, a set of relationships; in a hierarchy, elements are grouped into levels, according to other elements that have a higher rank than them. Simon succinctly defines a hierarchy as a system of subsystems, where each subsystem is composed of a ‘boss’ and a set of subordinate elements; the ‘bosses’ of each subsystem are in turn the subordinate elements of the hierarchy (Simon 1962). Hierarchies can be cataloged as ‘overlapping’ and ‘non-overlapping’. Non-overlapping hierarchies are straightforward: in such a hierarchy, each element only has one ‘boss’ (R. Dawkins 1976). An example of a non-overlapping hierarchy is the hierarchy of taxonomic rank, since a species is part of only one genus, a genus is part of one family, a family is part of only one order, and so on. In contrast, overlapping hierarchies contain at least one element that has more than one ‘boss’, for example in a motor hierarchy, a muscle group that is required for different movements can be accessed by more than one behavioral state (R. Dawkins 1976).

Ethological studies have proposed that inter-timescale coordination of behaviors can be achieved through a hierarchy, with longer-lasting motor programs or behavioral states at upper levels, and shorter-timescale motor actions at lower levels; and that these actions only occur in the context of a particular longer-timescale behavioral state or motor program (R. Dawkins 1976). For example, Nikolaas Tinbergen posited that the behavior of an animal could be organized in independent ‘instincts’, each of which consists of a hierarchical system of ‘centers’ or ‘nervous mechanisms’ (Tinbergen 1951; Hinde 1953). Famously, Tinbergen described the behavior of the three-spined stickleback as hierarchical: the reproductive instinct is made up of sub-behaviors like nest-building or defensive fighting; which themselves consist of sub-actions like digging or biting (Tinbergen 1951). This hierarchy was non-overlapping, such that actions within a sub-behavior are not executed within the context of a different sub-behavior. Shortly after, Hinde also used Tinbergen’s framework to describe behavior in the Great Tit as hierarchical (Hinde 1953). It is worth noting that already in 1940, Kortlandt had reported a complex hierarchical organization in the behavior of European cormorants, but this contribution did not garner the same attention as Tinbergen’s later would (Kortlandt 1956).

More recently, modern studies of the structure of behavior in detail have found hierarchies in the behavior of a variety of species. Analysis of the temporal structure of zebra finch song suggests a hierarchical organization of songs, which are composed of a series of motifs or clusters, in turn made up of sequences of syllables. Syllables show an alignment to the global tempo (Glaze and Troyer 2006).

Depth imaging of mouse behavior and machine learning revealed that mouse behavior is highly structured and it can be parsed into stereotyped, sub-second motifs that are organized in a predictable fashion. Further, different behaviors are not composed of different sets of movements, but rather of different combinations and different transition probabilities of these sub-second motifs (Wiltschko et al. 2015). Similarly, an analysis of the zebrafish locomotor repertoire using unsupervised behavioral clustering revealed that larval zebrafish locomotion can be categorized into 13 swim bout types that are arranged into specific sequences depending on the context. The authors observed a hierarchical structure in behavior, with clustering at different temporal levels and where each level is composed of different combinations of the basic behavioral building blocks of the lower level (Marques et al. 2018). Lastly, a 2016 study looked into the organization of the behavioral repertoire of *Drosophila melanogaster* over a longer timescale, with the intention to test whether hierarchical organization could explain the temporal structure of fly behavior better than other models. This study found that behavior in the fly can be decomposed into stereotyped motions and that behavior exhibits longer time scales, consistent with a behavioral hierarchy (Berman, Bialek, and Shaevitz 2016). A hierarchical organization entails that sub-behaviors that are part of the same partition occur closer in time than sub-behaviors from different behavioral partitions, such that the assumption of a hierarchical organization can help predict future actions. Crucially, this study made no a priori assumptions about the structure of the data, and found that a hierarchical representation of actions optimally predicted the future behavioral state. Thus, a hierarchy of behaviors across timescales underlie *Drosophila* locomotion.

3.3 Interrogation of neurobiological implementations of hierarchies

The studies presented so far have quantitatively described the temporal structure of behavior, and suggested the organization of some behaviors to be hierarchical. However, hierarchically described behavior need not be driven by hierarchically organized neural mechanisms. For example, the temporal structure of zebra finch song has been described as hierarchically organized (as mentioned above, (Glaze and Troyer 2006)), but intracellular recordings of the premotor nucleus HVC– the song production circuit in zebra finches– found evidence that its song is produced by a feedforward chain of synaptically connected neurons, which argues against hierarchical control mechanisms (Long, Jin, and Fee 2010).

Have researchers found indications of a hierarchical control of behavior in other organisms? Studies in *Drosophila* point in that direction: one study looking at the control of grooming behavior in flies activated neurons that drive individual grooming movements to test whether triggering specific grooming movements would suppress others, which was the case (Seeds et al. 2014). This study showed that a hierarchy of suppression, and not a feedforward chain of activation, underlies the neuronal control of *Drosophila* grooming behavior. Other evidence that behavioral hierarchies arise from neural control mechanisms comes from global neuronal activity recordings of a large portion of the *Drosophila* brain

while flies were behaving (walking, grooming, flailing) (Schaffer et al. 2021). This study found that the activity of most neurons recorded correlated with instantaneous running, while smaller clusters of neurons correlated with running on longer timescales than individual running bouts (the so-called ‘tendency to run’). Similarly, many neurons correlated with vigorous ‘flailing’ behavior, while specific clusters correlated with the less vigorous grooming behavior. Moreover, the authors found that neuronal clusters participate in the global behavior-related dynamics and also show residual activity independent from the locomotor state. This study suggests that brainwide dynamics represent vigorous behavioral states, probably involving many muscles and neurons, while spatially restricted clusters of neurons represent more localized behaviors, such as grooming, and behavior at longer timescales, such as the tendency to run. This paper suggests that different time scales of behavior are represented in the *Drosophila* brain, and that neuronal representations of behavior are nested across spatial scales, hinting at a hierarchy in neuronal activity in *Drosophila*.

Further evidence for neural implementations of hierarchical control of behavior come from studies of the orofacial movements for exploration in rats. It has long been known that rat exploration involves the orchestration of rhythmic movements of the head, nose and whiskers (Welker 1964). Pioneering work from the Kleinfeld lab showed that breathing and whisking are nested behaviors, and that the whisking rhythm is phase-locked to the breathing rhythm, such that its phase is reset by every breath (Moore et al. 2013). The authors identified a brainstem area with neurons that drive the whisking rhythm– in addition to the already identified pre-Bötzinger complex that generates the breathing rhythm (Smith et al. 1991; Rekling and Feldman 1998) – and showed that they are separable oscillators. Further, they found a unilateral connection from the breathing oscillator to the whisking oscillator, hinting at a hierarchical control mechanism. Thus, the authors discovered phase-locked oscillators that drive phase-locked behaviors, and suggest that hierarchical control underlies the orchestration of whisking and breathing. Later work elegantly showed that nose and head movements are also coordinated with the breathing rhythm (Kurnikova et al. 2017). These studies and others suggest that the inspiratory rhythm acts as a “master clock”, orchestrating orofacial behaviors, and further hint at a possible role of the breathing rhythm in binding the perception of sensory information from tactile and olfactory input sources (Kleinfeld et al. 2014). Unfortunately, these studies have not investigated how the activity of breathing and whisking oscillators interact with each other, and more broadly, with global brain patterns. Broadly speaking, how different activity patterns interact to orchestrate behavior across timescales is poorly studied so far.

3.4 Locomotion and Central Pattern Generation

Many of the studies detailed above have described a hierarchical organization of behavior in the context of rhythmic motor patterns, such as whisking/breathing, and swimming (Welker 1964; Smith et al. 1991; Rekling and Feldman 1998; Moore et al. 2013; Kleinfeld et al. 2014; Kurnikova et

al. 2017; Marques et al. 2018). Some of the most evolutionarily conserved behaviors have a rhythmic nature, like breathing, feeding, and locomotion. The orchestration of their rhythmic muscle contractions is oftentimes crucial for survival (Eve Marder et al. 2001). And in a less-essential-for-survival, but still important, way, the production of rhythms in music are hypothesized to have a social bonding function (Savage et al. 2020; Tarr et al. 2015; T. Wang 2015). So, while a behavioral hierarchy seems like a clever solution to the orchestration of behaviors across timescales, an additional challenge is to generate rhythmic neuronal activity to drive rhythmic movement sequences reliably and adaptively.

Historically, it has been proposed that rhythmic muscle contractions can be generated by (a) reflex chains (Loeb 1918) and (b) Central Pattern Generators (Delcomyn 1980). Reflex chains are self-explanatory: A sequence of successive movements is generated by an initial stimulus activating a neuron, whose activity acts as a stimulus for a consecutive neuron, and so forth. This chain of neuronal activation is fueled by proprioceptive feedback and generates patterned neuronal activity. In contrast, Central Pattern Generators are neurons or circuits that intrinsically produce rhythmic neuronal activity in the absence of patterned timing information from descending inputs or sensory feedback. These concepts are not per se mutually exclusive; it is possible that CPGs generate oscillatory activity that requires their entrainment through proprioceptive feedback for coherent locomotion. In fact, though experimental preparations of isolated neuronal circuits can generate rhythmic activity reminiscent of behavioral patterns, characteristics of the pattern— such as frequency, cycle period and amplitude— are often markedly different than in intact animals (Eve Marder et al. 2001; Fox, Soll, and Wu 2006; Goulding 2009). Thus, CPG circuits can generate rhythmic output in the absence of patterned, time-varying sensory input, while often being strongly influenced by sensory inputs in the behaving animal. CPG circuits fulfill at least two functions: rhythm generation and pattern generation. Mechanisms of rhythm generation relate to those that create regularly repeating activity or basic rhythmicity, like a clock, and are often found in single neurons or small groups of neurons within a CPG circuit (Kiehn 2011). Pattern generation refers to the generation of rhythmic patterns that recruit muscle groups in the correct order and in the temporal relationships that are observed during locomotion, including for example the alternation of opposing muscle groups (Kiehn 2011; Bucher et al. 2015). Pattern generation is thus achieved by all the neurons participating in a CPG network. Thus, neurons and circuits can be distinguished by their rhythm- and/or pattern-generating ability.

Pattern generation can be classified into cell-autonomous and network-based burst mechanisms. Cell-autonomous mechanisms are based on the properties of intrinsically oscillatory cells. The membranes of these “pacemaker neurons” have specific ion channel compositions that produce oscillations in their membrane potentials (Eve Marder 2011). For example, intrinsic oscillatory activity can result from hyperpolarization-activated inward currents or low-threshold activated inward currents, which spontaneously depolarize the membrane potential. Hyperpolarizing outward currents from voltage- or calcium-gated channels can follow this depolarization, they restore the membrane potential to its inactive phase, and the cycle can begin again (Bucher et al. 2015). On the other hand, in network-

based pattern generation, rhythmic activity results from the synaptic interactions of neurons that may or may not be oscillatory on their own (Satterlie 1985). Oftentimes, network-based rhythm generation relies on reciprocal synaptic inhibition, which generates out-of-phase oscillations and thus alternating activity to drive the sequential activation of different muscle groups. This organization is termed a ‘half-center’ oscillator, and it can but need not contain intrinsically oscillatory neurons (Brown 1914).

Invertebrate CPG circuits have been studied in detail and have been invaluable for understanding CPG mechanisms. Neuronal ensembles have been shown to generate rhythmic activity without sensory feedback in the locust (Wilson 1961), but arguably the most well studied CPG circuit is the stomatogastric ganglion (STG) of lobsters and crabs. The STG is a ganglion in the stomach composed of about 30 neurons, which generates two characteristic rhythms for constricting pyloric muscles to filter food and for grinding the gastric mill teeth to pulverize it (Clemens et al. 1998). Studies showed that completely isolated CPG circuits of the stomatogastric ganglion of the lobster can produce fictive motor patterns *in vitro* (Prinz, Thirumalai, and Marder 2003) similar to those observed *in vivo* (Clemens et al. 1998). This property of the circuit makes it possible to study rhythmic pattern generation in preparations where the stomatogastric ganglion is separated from the animal and freely accessible for electrophysiological and neuromodulatory characterization, yielding comprehensive studies on CPGs and modulation. Decades of research on these circuits have elucidated their mechanisms of rhythm and pattern generation, the development of its activity patterns, the role of inhibition in rhythm generation, how robust these circuits are to perturbations, and its neuromodulation (Richards, Miller, and Marder 1999; Eisen and Marder 1984; Haley, Hampton, and Marder 2018; Powell et al. 2021; E. Marder and Eisen 1984; Hooper and Marder 1987; Ayali and Harris-Warrick 1999, and many more).

The *crustacean* stomatogastric ganglion may be the neuronal network that has been described the most thoroughly so far. However, *crustaceans* are accessible only to the studies of isolated ganglia and also lack the genetic tools to study the molecular characteristics of their neurons. Ideally, one would not only study CPG function in isolation, but would also understand how CPG activity is embedded into longer-lasting representations of behavioral sequences. Thus, studying the inter-timescale coordination of CPG activity to the global nervous system dynamics requires the study of CPGs in intact preparations.

3.5 *C. elegans*, an ideal subject for the study of behavioral hierarchies and CPGs

The soil nematode *C. elegans* is a powerful model organism for interrogating the neuronal underpinnings of a behavioral hierarchy, and for exploring how CPGs are embedded into such slower timescale representations of behavioral sequences. *C. elegans* worms are small, only 1mm in size, yet they display a rich repertoire of behaviors such as sleep, food search, defecation, nictation, among others (Croll 1975; Raizen et al. 2008; Lee et al. 2011). *C. elegans* is –perhaps only– numerically very simple: hermaphrodites have a total of 959 somatic cells, whose development has been described from the

fertilized egg until adulthood, and they can be identified from animal to animal (Sulston and Horvitz 1977). It has 302 neurons whose synaptic connections have been mapped (J. G. White et al. 1986; B. L. Chen, Hall, and Chklovskii 2006; Varshney et al. 2011; Cook et al. 2019; Witvliet et al. 2021). *C. elegans* neurons are thought to be nearly isopotential; they mostly show graded synaptic transmission in lieu of sodium-dependent action potentials (Bargmann 1998; Goodman et al. 1998; Lindsay, Thiele, and Lockery 2011), with a few, recently reported exceptions (Q. Liu et al. 2018; Jiang et al. 2022). Nevertheless, these properties and the fact that calcium triggers synaptic vesicle release make calcium dynamics a good proxy for neuronal activity and synaptic communication. Since *C. elegans* is transparent and has a limited number of neurons, fluorescent calcium indicators can be used to study neuronal activity in the intact organism, both nervous-system-wide with single-cell resolution, and also in freely moving animals (Kato et al. 2015; Nguyen et al. 2016; Venkatachalam et al. 2016). Lastly, its genetic tractability makes genetic manipulations and transgene expression straightforward, while recent single-cell gene expression datasets have made gene expression profiles available for all 118 neuron classes (Lorenzo et al. 2020; Taylor et al. 2021).

3.5.1 Anatomy and function of the *C. elegans* nervous system

General description of C. elegans behavior and locomotion

As mentioned previously, *C. elegans* displays a rich behavioral repertoire that is not limited to mating, sleeping, and searching for food. Perhaps the most well studied of these behaviors is food search, which is composed of forward-directed locomotion, interspersed with backward-directed locomotion (termed ‘reversals’) and dorsal or ventral turns immediately after reversals (termed ‘reorientation turns’) (Stephen E. Von Stetina, Treinin, and Miller 2006). Reorientation turns are biased, such that about 70% of reversals will end in a ventral turn, and 30% in a dorsal turn (Kato et al. 2015). Deep post-reversal turns are called omega turns because of the shape the worm takes when performing them (the head nears the tail, making a shape similar to the greek letter Ω). These individual behaviors occur in a specific order— forward locomotion is followed by reversals and reversals usher in post-reversal turns— such that it can be viewed as an action sequence (Gray, Hill, and Bargmann 2005; Faumont, Lindsay, and Lockery 2012; Kato et al. 2015). Behavioral analyses and modeling studies suggest that worms switch between forward- or backward crawling stochastically (Roberts et al. 2016).

C. elegans moves forward by propagating undulatory muscle contractions that go from head to tail. These are alternating dorsal and ventral body bending waves against the direction of locomotion. Additionally, worms move their head and/or nose independently from the body bending waves that propel the animals forward (Croll 1975). These types of head movements occur only within forward locomotion and are actively inhibited during backward-directed locomotion (Hart, Sims, and Kaplan 1995), suggesting that head movements have a function specifically during forward locomotion.

Observing behavior at longer timescales, we can identify further temporal structure in food search behavior: when exploring a bacterial food source, worm locomotion is described as either ‘roaming’ or ‘dwelling. Dwelling consists of mostly short forward movement with many head-waving movements, short reversals and shallow angle turns; roaming is dominated by long bouts of fast forward movement and few reversals (Fujiwara, Sengupta, and McIntire 2002; Ben Arous, Laffont, and Chatenay 2009; Flavell et al. 2013; Shtonda and Avery 2006). When *C. elegans* animals are removed from food, they engage in two consecutive locomotion states: First, they engage in a local search state (also called “area-restricted search”) comprising long-lasting, high-angle turns and omega bends. After about 15 minutes, they switch to a global search state with forward-directed locomotion and a suppression of turning (Hills, Brockie, and Maricq 2004; Wakabayashi, Kitagawa, and Shingai 2004; Gray, Hill, and Bargmann 2005). It has been suggested that the stereotyped switch between these states enables effective foraging (Calhoun, Chalasani, and Sharpee 2014; Salvador et al. 2014).

Behavioral hierarchies in C. elegans

C. elegans behavior can be observed at many timescales: behavioral states such as quiescence, feeding and exploration can last several minutes, motor actions such as forward and reverse crawling last seconds to minutes, and body bends and head movements occur at the sub-second scale. Valuable studies focus on the neural control of behavior at the sub-second scale (Gao et al. 2018; Shen et al. 2016; Wen et al. 2012; Xu et al. 2018; Fouad et al. 2018), the transition between motor programs (Kato et al. 2015; Kawano et al. 2011; Z. Li et al. 2014; Piggott et al. 2011), or on the transitions between longer-lasting behavioral states (Flavell et al. 2013; Nichols et al. 2017). These studies would be well complemented by interrogations on how behavior is orchestrated at multiple timescales.

The possibility of hierarchical organization of behavior in *C. elegans* is explored in a few select studies. Tinbergen had proposed that a decision hierarchy constrains the behaviors an animal could choose to perform, and that this hierarchy is established by the animal’s hormonal state and influenced by external and internal signals (Tinbergen 1951). It has been observed that worms exhibit distinct gaits when on land (crawling) or on water (swimming), that are under the control of neuromodulators dopamine and serotonin (A. Vidal-Gadea et al. 2011). When on land, worms perform behaviors such as defecation, egg-laying, food ingestion, and foraging (fast movements of the anterior tip of the worm) (Croll 1975; Hart, Sims, and Kaplan 1995; Pierce-Shimomura et al. 2008; Raizen et al. 2008; Lee et al. 2011). Researchers investigated whether transitions between distinct physical environments can affect the production of different motor programs in *C. elegans*. The study showed that swimming inhibits the production of several land-associated behaviors, and exposure to dopamine can revert their inhibition in swimming worms (A. G. Vidal-Gadea and Pierce-Shimomura 2012). This study is perhaps the first indication that longer-lasting behavioral states (swimming vs. crawling) constrain the production of motor actions (egg-laying, defecation...) in *C. elegans* and suggest that worm behavior is under hierarchical control. A few years later, the Brown lab explored whether structure can be revealed in

worm locomotion using data compression algorithms on recordings of spontaneous crawling, with the motivation to uncover structure that could be missed by the naked eye (Gomez-Marin, Stephens, and Brown 2016). This detailed analysis of the temporal structure of worm posture indeed suggested spontaneous *C. elegans* locomotion to be hierarchically organized. Although behavioral analyses alone cannot tell whether the underlying neuronal processes controlling behavior are hierarchical, the resources and experimental possibilities that *C. elegans* research offers pose an ideal starting point to explore this question.

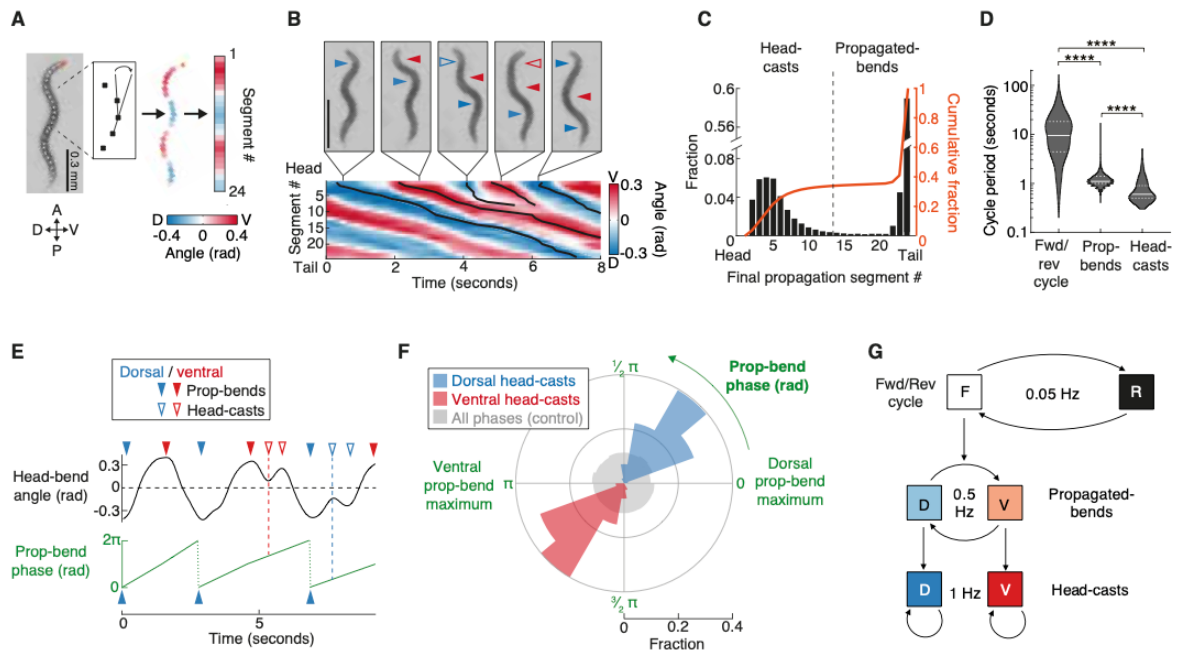


Figure 3.1. A multi-timescale behavioral hierarchy. (From Kaplan et al, 2020) **(A)** Body angle measurement. A: anterior, P: posterior, V: ventral, D: dorsal. **(B)** Lower: example posture timeseries kymogram. Head-bend propagations traced by black lines. Upper: worm images with propagated-bends (filled arrows) and head-casts (open arrows) indicated. Scale bar, 0.4 mm. **(C)** Fractional and cumulative distributions of each head-bend's most posterior propagation segment. $n = 45,129$ head bends pooled from 28 assays, ~ 20 animals per assay. **(D)** Violin plot showing median and 1st and 3rd quartiles of cycle periods for forward/reverse (forward + reverse bout duration, $n=1,259$), propagated-bend ($n=25,817$), and head-cast cycles ($n=341$) pooled from 14 assays, ~ 20 animals per assay. $****p < 0.0001$, Mann-Whitney Test. **(E)** Example head-bend angle timeseries illustrating propagated-bend phase measurement. Red and blue dashed lines indicate initial head-cast phases, quantified in **(F)**. **(F)** Fractional distributions of initial head-casts binned according to their propagated-bend oscillation phases. $n = 427$ dorsal and 194 ventral head-casts pooled from 21 animals. $p < 10^{-6}$ for both distributions, indicating the probability that each is drawn from the full data distribution shown in grey. **(G)** Hierarchical model of behavior with corresponding cycle frequencies from **(D)**.

In our recent work (Kaplan et al. 2020), we set out to describe a behavioral hierarchy with the goal of uncovering the neuronal mechanisms that implement it. To this end, we recorded and tracked animals at high resolution to measure motor programs and associated gaits (Fig. 3.1a). We skeletonized the worm's body in each video frame and measured 24 bend angles along the skeleton. This results in a representation of worm posture over time, termed kymogram (Fig. 3.1a-b). Kymograms represent the worm's posture at each time point as well as the evolution of bending across body segments. We focused on forward locomotion, which consists of dorsal and ventral body bending waves (Fig. 3.1b). These

bends originate in the head and propagate posteriorly. We found two types: “propagated-bends”, where the bend propagated all the way to the tail; and intervening head movements, termed “head-casts”, that terminated anterior to the mid-body (Fig. 3.1c) (for data supporting that head-casts are a distinct motor action and not simply aborted propagated bends, see (Kaplan et al. 2020)). Forward crawling consisted mostly of propagated-bends, with interspersed head-cast episodes. The cycles of head-cast oscillations were faster than propagated bends’, and including the switches between forward- and backward crawling, we found behaviors spanning three timescales (Fig. 3.1d) (Kaplan et al. 2020). Moreover, head-casts are lateralized, such that head-casts in the dorsal direction followed dorsal propagated-bends, and ventral head-casts succeeded ventral propagated-bends (Kaplan et al. 2020). We looked into this relationship further by calculating the phase of the propagated-bend cycle and visualizing when dorsal/ventral head-casts occur within it, and found that head-casts are restricted to specific phases of the propagated-bend cycle, a relationship we termed ‘phase-nesting’ (Fig. 3.1e-f) (Kaplan et al. 2020). This phase dependence suggests that head-cast occurrence is constrained by the propagated-bend cycle. The relationships between these behaviors, where head casts occur at specific phases of the propagated-bend cycle, and propagated bends occur within the forward locomotion program, suggest that worm locomotion is hierarchically organized (Fig. 3.1g) (Kaplan et al. 2020).

Anatomy of C. elegans Nervous System

The nervous system of *C. elegans* comprises 302 neurons, categorized into 118 classes. Because *C. elegans* is bilaterally symmetric, many of its neurons are organized into bilateral left/right pairs (for example, the AVA class is made up of AVAL and AVAR) (J. G. White et al. 1986; Hobert, Johnston, and Chang 2002). This symmetric organization is also reflected in their morphology and connectivity, such that neurons of a bilateral pair will often have interchangeable functions (for an example of an exception, see (Cochella and Hobert 2012)). Its neurons are distributed among ganglia in the head and tail of the worm and along its ventral nerve cord (VNC). The head and tail ganglia contain sensory, inter- and some motor neurons, while the VNC extends along the anterior-posterior axis of the worm and contains mainly motor neurons.

Forward- and backward-directed movement is driven by signals from different interneuron pools: AVB and PVC interneurons activate the B-type forward-active motor neurons (described below), and AVA, AVD and AVE interneurons promote backward movement by activating A-type motor neurons (Chalfie and White 1988; Stephen E. Von Stetina, Treinin, and Miller 2006). The activity of these interneurons determines the direction of movement, but does not drive the propagation of body bending waves from head to tail for forward locomotion (or from tail to head for reversals). Wave propagation is thought to be facilitated by proprioception (Wen et al. 2012; Xu et al. 2018).

Head movements are coordinated by the head motor circuit, which consists of 11 motor neuron classes that innervate the anterior (head and neck) muscles. These include several excitatory (cholinergic) motor neuron classes, among them the SMD class, and one inhibitory (GABAergic) motor

neuron class, the RME class (Altun et al. 2009; Gray, Hill, and Bargmann 2005; J. G. White et al. 1986). Next, I will introduce specific inter- and motor neuron classes involved in the control of *C. elegans* locomotion which are of importance to this thesis.

Interneurons of importance to this study

The AVA neuron class

AVA is a premotor interneuron class which can be viewed as a bottleneck or relay between other interneurons and the VNC motor neurons (J. G. White et al. 1986). AVA activates the A-type motor neurons (A-MNs), which drive the muscle activation required for backward-directed locomotion (more information on the A-MNs below). Optogenetic activation of AVA results in backward locomotion, and AVA ablation or inhibition results in practically no backward locomotion (Schmitt et al. 2012; Chalfie et al. 1985; Pokala et al. 2014). Calcium imaging recordings of head ganglia neurons showed that AVA is active concomitantly with other backward-active neurons such as AVE, AIB and RIM (Kato et al. 2015). Further, AVA inhibition leads to pauses in locomotion followed by post-reversal reorientation turns, and AVA inhibition leads to the silencing of A-MNs, but not of other backward-locomotion interneurons (Pokala et al. 2014; Kato et al. 2015). These observations show that AVA activity is crucial for the execution of the backward movement command, rather than the generation of the command itself.

The AIB neuron class

AIB is a command interneuron class whose activity plays a role in backward locomotion and reversal execution. AIB has been shown to play a role in long-lasting reversals and in the up-regulation of reorientation (omega) turns, and AIB laser ablation decreased the frequency of reversals (Gray, Hill, and Bargmann 2005). In optogenetic experiments, AIB inhibition reduced reversal frequencies, while AIB activation triggered reversal events (Kocabas et al. 2012; Y. Wang et al. 2020). Furthermore, optogenetic activation of AIB was reported to trigger reversals (Kocabas et al. 2012; Y. Wang et al. 2020) and optogenetic inhibition resulted in lower reversal frequencies (Kocabas et al. 2012). These results are in line with whole-brain imaging experiments, where AIB is co-active with reversal interneurons AVA, AVE and RIM (Kato et al. 2015). A recent study reported that AIB inhibition abolished reorientation turns in freely-moving animals, thus, older and more recent studies implicate AIB in reversal-to-turn transitions (Gray, Hill, and Bargmann 2005; Y. Wang et al. 2020).

The RIM neuron class

RIM is a motor-interneuron involved in backward locomotion. Its activity in immobilized, whole-brain imaging recordings correlates to reversal command-active neurons AVA, AVE and AIB (Kato et al. 2015). However, studies on freely-moving animals paint a more complex picture: RIM inhibition and ablation experiments resulted in increases in reversal frequency (Gray, Hill, and

Bargmann 2005; W. Li et al. 2011; Piggott et al. 2011), while other studies reported that its activation triggered reversal behavior (Gordus et al. 2015). In line with this, freely-moving calcium imaging of RIM showed a correlation between RIM activity and reversal speed (Kato et al. 2015), but other studies reported a downregulation of RIM activity during reversals (Piggott et al. 2011). In addition to this, RIM has been implicated in the generation of variable behavioral responses to external stimuli (Gordus et al. 2015). Nevertheless, the role of RIM in the context of anterior-touch-triggered reversals— anterior touch stimuli elicit a backwards escape response— is clear: RIM-ablated animals are defective in reversals in response to anterior touch and in the suppression of head oscillations during backward locomotion (Alkema et al. 2005). RIM is one of the few tyraminerpic *C. elegans* neurons; tyramine release inhibits head/neck muscles and the forward-active AVB command interneuron class (Alkema et al. 2005; Pirri et al. 2009; Pirri and Alkema 2012). Tyramine release activates tyramine-gated chloride channel LGC-55, which are expressed in head/neck muscles and head motor neurons such as SMD and RMD (Alkema et al. 2005; Pirri et al. 2009; Pirri and Alkema 2012). Thus, the RIM neurons play a role in stabilizing the reversal state and suppressing head oscillations during backward locomotion.

The RIB neuron class

RIB is a command interneuron that plays a clear role in forward locomotion. It is part of the forward locomotion circuit, it is active during forward locomotion and optogenetic activation promotes forward locomotion speed, while ablation greatly decreases it (J. G. White et al. 1986; Gray, Hill, and Bargmann 2005; Z. Li et al. 2014; Kato et al. 2015). RIB activity seems to mostly be involved in the modulation of forward locomotion speed, but it has recently been implicated in behavior state transitions; optogenetic activation of RIB during backward locomotion leads to transitions from backward locomotion to forward locomotion or to omega turns, and optogenetic RIB activation during forward locomotion led to omega turns (Y. Wang et al. 2020). To summarize, RIB neurons modulate forward locomotion speed and have recently been identified as modulators of behavioral state transitions.

Motor neurons of importance to this study

Head motor neurons

C. elegans enjoys more degrees of freedom in its head than in the rest of its body, where its repertoire of movement is restricted to dorsal and ventral muscle contractions. *C. elegans* counts on 11 motor neuron classes that innervate head and neck muscles, permitting them to move their heads laterally as well as dorsoventrally (J. G. White et al. 1986). For the sake of simplicity, we will focus on the SMD and RME head motor neuron classes.

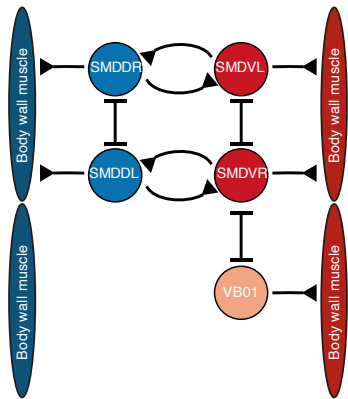


Figure 3.2. SMD and VB01 motor neuron connectivity. Neuron and muscle connectivity schematic illustrating the lateralized muscle innervations of CPG candidate motor neurons. Cell bodies and projections not shown to scale. Blunt arrowhead (|—) depict electrical junctions; inverted arrowheads depict chemical synapses. Neurons depicted in blue correspond to those innervating dorsal muscles, neurons depicted in red/salmon correspond to those innervating ventral muscles.

The SMD motor neurons

SMD is a class of 4 cholinergic motor neurons that innervate muscles in the head (J. G. White et al. 1986). The SMDs are divided into two left-right pairs: the dorsal SMDs— SMDDL and SMDDR— innervate dorsal muscles and the ventral SMDs— SMDVL and SMDVR— innervate the ventral counterparts (J. G. White et al. 1986). SMD left/right pairs are connected through gap junctions, as has been observed for many other neuron classes (J. G. White et al. 1986; Witvliet et al. 2021). Additionally, SMDs from opposite pairs show reciprocal chemical synapses, such that SMDDL and SMDVR are reciprocally connected, as are SMDDR and SMDVL (Fig. 3.2) (J. G. White et al. 1986; Witvliet et al. 2021). Because of their innervation of opposing muscle groups and their expression of inhibitory acetylcholine-gated chloride channels, these reciprocal connections have been hypothesized to be cross-inhibitory (Pereira et al. 2015). The SMDs send long, not-innervated processes posteriorly down the sublateral cords; it has been theorized that these could serve proprioception (J. G. White et al. 1986). Recently, it has been reported that they express mechanosensitive TRPC channels TRP-1 and TRP-2, and mutations in these channels seem to affect SMDD activity preferentially (Yeon et al. 2018). Thus, the SMDs have a proprioceptive function.

The SMDs are most well known for their role in reorientation turns, as SMD laser ablations result in reduced omega turn frequency and shallower omega turns (Gray, Hill, and Bargmann 2005). More recently, SMDV activity was shown to be correlated to head bending during post-reversal reorientation turns (Kato et al. 2015). On the other hand, SMDs show activity correlated with dorso-ventral head bending (Hendricks et al. 2012; Yeon et al. 2018). In line with this, we have also observed a relationship between SMD activity and head movements (Fig. 3.3): We analyzed SMD activity and its relation to locomotion in freely moving animals (Fig. 3.3b) and observed that SMDD peaked during dorsal head bends and SMDV during ventral head bends (Fig. 3.3b). Interestingly, SMDD and SMDV peaked at restricted phases of the head-bend cycle during forward locomotion, and at altered phases during reverse locomotion (Fig. 3.3e-f). Thus, our results and others' implicate the SMDs neurons in head movements during forward locomotion in addition to their known role in reorientation turns.

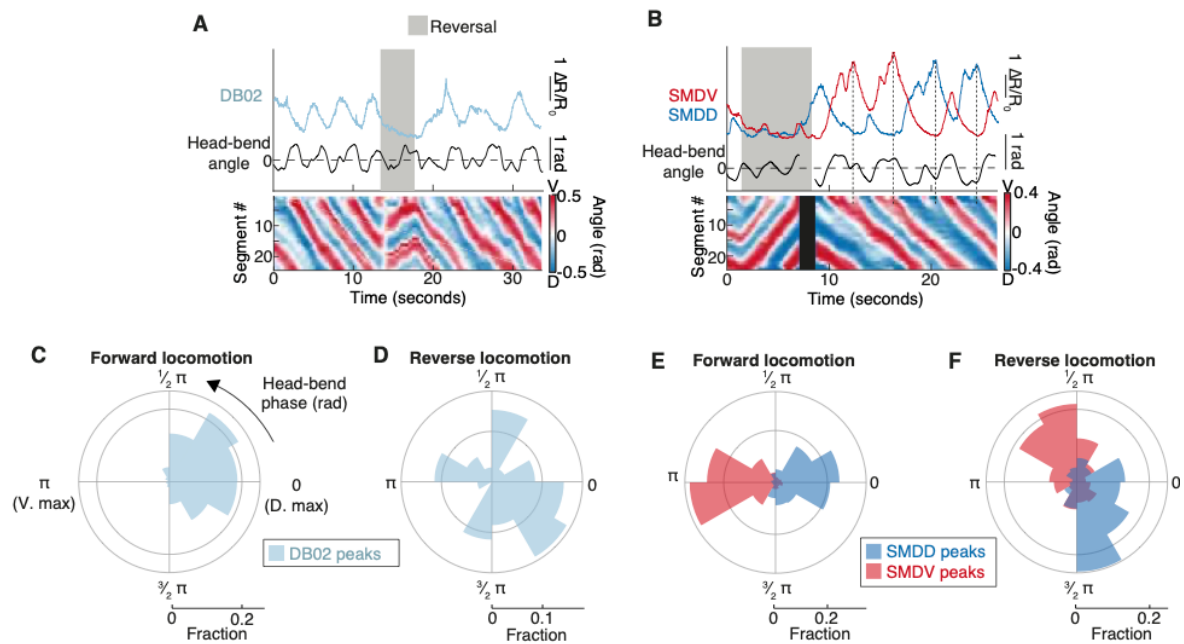


Figure 3.3. Hierarchy level I and II interaction: SMD neurons are multi-functional. (Adapted from Kaplan et al, 2020) (A-B) Example DB02 (A) and SMD (B) Ca^{2+} -imaging in moving animals. $\Delta R/R_0$ = normalized GCaMP/mCherry ratio. Lower: posture kymograms, black indicates missing data. Dotted vertical lines: unilateral SMDD- or SMDV-only oscillations. (C-F) Fractional distributions of DB02 (C-D) or SMD (E-F) Ca^{2+} peaks binned by head-bend phase during forward (C, E) or reverse (D, F) locomotion. $n = 746$ (C), 35 (D), 478 (E, SMDD), 389 (E, SMDV), 150 (F, SMDD), 158 (F, SMDV) peaks pooled across 11 (SMD) and 10 (DB02) animals. $p < 10^{-6}$ for all distributions except SMDV ($p = 3 \times 10^{-6}$) and DB02 (ns, $p = 0.26$) during reverse locomotion, indicating the probability that distributions are drawn randomly. Probability that each neuron's reversal distribution was drawn from its respective forward distributions: $p < 10^{-6}$ (SMDD and SMDV) and 0.0014 (DB02).

Interestingly, work by the Yun Zhang lab suggests that the SMDs are potentially involved in the integration of body movement information with incoming sensory input, a strategy used for the localization of attractive sensory signals in navigation (H. Liu et al. 2018). The location of an odorant can be determined if it is differentially sensed on one side more than the other while the animal is moving forward. An elegant way to discriminate the location of an odor source could be a coincidence detection neuron that gets information on the direction of the movements that the animal is performing, and sensory information. This seems to be the case for RIA interneurons, which regulate navigation behaviors (Ha et al. 2010). RIAs get input from multiple sensory networks, and they are connected to the SMDs, whose activity is tightly linked to dorsal and ventral head movements (J. G. White et al. 1986; Gray, Hill, and Bargmann 2005; Ha et al. 2010; Hendricks et al. 2012; Shen et al. 2016). RIA receives sensory information throughout its process but spatially-segregated head-bend information from SMDD and SMDV to different axonal compartments (J. G. White et al. 1986; Hendricks et al. 2012). These compartmentalized dynamics help worms steer toward attractive odors because the coincidence of odor-evoked activity and a head-bend signal in one compartment but not the other leads to a difference in signal strength; this asymmetric activation of one RIA process compartment is then used to modulate the activity of the same SMD that provided the head-bend signal, biasing the animal's head bends towards the attractant (H. Liu et al. 2018). Thus, the neuronal circuit composed of the SMDs,

RIAs and sensory neurons play a role in integrating the worm's movement into sensory information processing.

The RME motor neurons

RME is a class of 4 GABAergic motor neurons that innervate head muscles (J. G. White et al. 1986). The class comprises RMED, RMEV, RMEL and RMER. RMEL and RMER synapse onto muscles, while RMED and RMEV synapse onto muscles but probably also onto adjacent SMD processes (Altun, Z.F. and Hall, D.H. 2021). RME (D/V) activity negatively modulates the amplitude of undulatory head bending during forward locomotion (Shen et al. 2016). RMED/V show oscillatory calcium signals during undulatory dorsal/ventral head bending, and these signals are preceded and driven by extrasynaptic signals from SMDD/V (Shen et al. 2016). The resulting RME signal limits head bend amplitude by inhibiting SMD, a positive regulator of head bend amplitude (Shen et al. 2016).

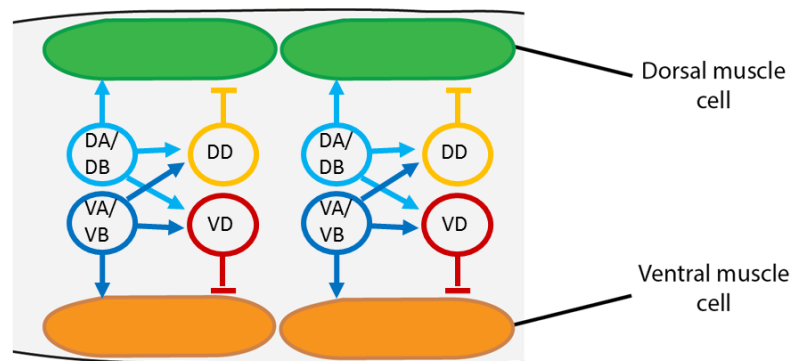


Figure 3.4. Schematic of the *C. elegans* nervous and muscle system anatomy. Simplified wiring diagram of the motor neurons that innervate body muscles and coordinate their contractions. Forward movement is executed through the activation of dorsal (DB) and ventral (VB) B motor neurons; backward movement is controlled by the dorsal (DA) and ventral (VA) A motor neurons. Upon activation of dorsal A or B neurons, the ventral muscle is inhibited by activating the GABAergic VD neurons; when the ventral A or B neurons are activated, dorsal muscles are inhibited by the DDs. Neurons of each cell type are connected via gap junctions, therefore propagating signals along the worm's body. (Inspired by (Wen et al. 2012)).

Body motor neurons

C. elegans moves forward through sinusoidal, dorso-ventral muscle contractions that go from head to tail, and backwards through muscle contractions that propagate from the tail to the head. Regardless of the direction of movement, alternating dorsal and ventral body bending waves propagate through the body, and dorsal muscle activation coincides with the inhibition of opposing ventral muscles, and vice versa. Its body wall muscles are organized into dorsal and ventral rows that are controlled by eight distinct classes of motor neurons: DA, VA, DB, VB, DD, VD, AS and VC (J. G. White et al. 1986). A-, B- and D-type motor neurons are divided into ventral and dorsal motor neurons, according to the muscles that they innervate, such that DA, DB and DD (and AS) neurons send commissures from the ventral side to innervate dorsal muscles, and VA, VB, VC and VD neurons

innervate ventral body wall muscles (Fig. 3.4) (J. G. White et al. 1976, 1986). The neurons are also differentiated according to the movements that they are involved in: DA, VA and AS are cholinergic motor neurons that drive backward locomotion; DB and VB are cholinergic motor neurons that activate body wall muscles to drive forward locomotion; DD and VD are GABAergic and facilitate the relaxation of dorsal/ventral muscles opposite to ventral/dorsal muscles that are contracting; and VC motor neurons control vulval muscles (J. G. White, Albertson, and Anness 1978; McIntire et al. 1993). For a more complete picture of the role of VD- and DD- motor neurons, see (Deng et al. 2021)) A- and B-type motor neurons (A-MNs and B-MNs) are activated by command interneurons. Body motor neurons are connected to the globally distributed network states that represent locomotion through output neurons AVA and AVB: Backward-active interneurons activate the A-MNs through output neuron AVA, driving backward crawling (Chalfie et al. 1985). Forward-active interneurons activate B-MNs through AVB and drive forward crawling, and the B-MNs are rhythmically active during forward crawling (Haspel, O'Donovan, and Hart 2010; Kawano et al. 2011; Wen et al. 2012). AVB and B-MNs are electrically connected through heterotypic UNC-7S/UNC-9 gap junctions, with UNC-7S expressed in AVB and UNC-9 in B-MNs (T. Starich et al. 2009).

Command interneurons do not orchestrate the propagation or the alternation of body bending waves, they merely provide excitatory input to all motor neurons of the relevant class. To understand how undulatory movements are generated in this nervous system, we will focus now on the forward locomotion circuit, which is most relevant to this study. As mentioned before, forward command interneuron AVB activates B-MNs to drive forward movement. The B-MNs comprise 7 dorsal DBs and 11 ventral VBs (DBs 1 through 7, VBs 1 through 11). Our recent work focused on the B-MNs, mostly DB02 and VB01, which are located on the anterior end of the ventral nerve cord (VNC), in the retrovesicular ganglion. We recorded the activity of B-MN DB02 in freely-behaving animals and observed activity oscillations strongly correlated with head bend angle, specifically during dorsal bends (Fig. 3.3a,c). During reverse locomotion, DB02 activity was largely reduced, showing small peaks with no correlation to head-bending (Fig. 3.3a,d) (Kaplan et al. 2020). We also focused on VB01, a ventral B-MN that has slightly different connectivity than other B-MNs (Haspel and O'Donovan 2011) and interestingly, is the only B-MN that is electrically connected to the SMD head motor neurons (through gap junctions between SMDVR and VB01) (J. G. White et al. 1986).

Going back to the question of how undulatory waves are generated and propagated along the body, it bears mentioning that B-MNs are connected to their anterior and posterior B-MN neighbors through gap junctions (J. G. White et al. 1986). This chain of interconnected motor neurons could be a good substrate for undulatory wave propagation, as activation starting at motor neurons near the head could propagate along the body through gap junctions. Adding to this, a study in 2012 uncovered that B-MNs are proprioceptive, and this proprioception drives the propagation and coordination of undulatory waves from head to tail (Wen et al. 2012). Thus, researchers proposed that undulatory locomotion could be achieved without distributed CPGs along the motor circuit, by the action of a CPG

near the head that generates the rhythmic bending of anterior segments, combined with wave propagation through proprioception in the motor neurons (Wen et al. 2012). Then, later studies suggested that both A- and B-MNs themselves participate in local oscillator circuits (Xu et al. 2018; Gao et al. 2018; Fouad et al. 2018), but the capacity of individual B-MNs to generate rhythmic activity was not confirmed. Thus, it was hypothesized that at least three oscillator units – an unknown head CPG, the VNC motor neurons in the midbody region (between VB3 and AS7), and the posterior VNC motor neurons (between VB9 and AS11) – or even individual motor neurons, generate oscillations and could be entrained by proprioception (Fouad et al. 2018). Further, electrical coupling between AVB and the B-MNs was shown to induce oscillations in the B-MNs and facilitate wave propagation (Xu et al. 2018). Taken together, the literature points to a model where B-MNs act as local oscillators that generate intrinsic rhythmic activity; the oscillators are themselves proprioceptive as well as connected to each other through gap junctions, which poses a mechanism for the oscillations to be entrained and the body bending wave to be propagated from head to tail (Fouad et al. 2018; Xu et al. 2018). Nevertheless, rhythmic activity of the B-MNs has not been shown in immobilized animals, nor has it been clarified whether specific B-MNs or small circuits are rhythmogenic; which neurons generate rhythmic activity to drive head movements has also remained elusive.

3.5.2 Neuronal population dynamics in *C. elegans*

Recent advancements have made it possible to record neuronal population dynamics of head and tail ganglia at single-cell resolution in *C. elegans* (Schrödel et al. 2013; Kato et al. 2015; Uzel, Kato, and Zimmer 2022). These studies rely on the use of various versions of genetically-encoded calcium indicator GCaMP (Nakai, Ohkura, and Imoto 2001; Akerboom et al. 2012). GCaMP is a fusion protein that contains green fluorescent protein (GFP), Calmodulin (CaM) and a sequence from myosin light-chain kinase, M13. GCaMP is engineered to contain a permuted GFP. Calcium influx into the cell leads to CaM calcium binding and a conformational change that will result in CaM binding to M13. This in turn leads to a conformational change of the split GFP and an increase in GFP fluorescence (Nakai, Ohkura, and Imoto 2001). Studies from the Zimmer lab recorded neuronal activity in *C. elegans* by restricting the localization of GCaMP to neuronal nuclei and making use of microfluidic devices for the immobilization of animals and acute delivery of sensory stimuli (Schrödel et al. 2013; Prevedel et al. 2014; Kato et al. 2015). Pan neuronal imaging of the activity of unstimulated animals revealed that many neurons in the head of *C. elegans* are active in immobilized animals subjected to constant conditions. Many neurons participate in coordinated activity patterns that are not obviously caused by sensory stimuli, and are thus interpreted as spontaneous network activity (Schrödel et al. 2013). Principal component analysis (PCA) was used to characterize the global dynamics and extract the major signals dominating the head ganglia; around 60% of the total variance in the neuronal traces was explained by the first 3 PCs (Kato et al. 2015). To understand how these activity patterns relate to behavior, the activity of single neurons was recorded in conditions that allowed animals to roam freely.

The information on how single neurons' activities relate to behavior was then used to interpret the global activity patterns in immobilized worms; PCs 1-3 get contributions from many neurons whose activity correlates with the action sequence. PC 1 is dominated by the activity of neurons that correlate to forward or reverse crawling; for example, signals shared across AVA, RIM and AIB neurons correlate with reversals, while AVB and RIB signals correlate with forward locomotion and are anticorrelated with the former. PC2 and PC3 are often dominated by head motor neurons whose activities correlate with turning maneuvers (Gray, Hill, and Bargmann 2005; Kato et al. 2015). Thus, the major signals permeating the nervous system are shared across many neurons and show coordinated, cyclical network dynamics that represent the worm's major motor commands assembled into an action sequence, like the one used for food search (Kato et al. 2015).

One of the traits most often used to describe central pattern generating circuits is the ability to generate rhythmic behavior in the absence of timing cues. Pan neuronal imaging in immobilized *C. elegans* is therefore a great paradigm to study rhythmogenesis in the absence of proprioceptive feedback, because the method imposes a lack of patterned sensory information in the microfluidic device and muscle paralysis caused by the agent tetramisole. Moreover, this paradigm allows for interrogation of neuronal activity in intact animals, providing an entrypoint into understanding how CPGs are coupled to and modulated by nervous system activity, as well as how CPG activity is embedded in the representation of the worm's major motor commands.

3.6 Aims of this thesis

A lot of important research focuses on studying how neuronal activity drives behavior at individual timescales, but behavior is driven and orchestrated on different timescales and simultaneously. Thus, our work aimed to understand how the nervous system coordinates behavior across timescales and how neurons driving behaviors on different timescales interact. Behavioral hierarchies have been proposed and described since the 50es, but whether hierarchies in behavior are driven by hierarchically organized activity remained unknown. Our recent work uncovered a behavioral hierarchy in *C. elegans* (Kaplan et al. 2020), an ideal model organism because it allows for high resolution descriptions of behavior, and neuronal activity recordings at a single-cell, yet pan neuronal level. The genetic tractability and complete connectome allow for informed hypothesis building and for testing of those hypotheses using genetic tools. Investigating whether this behavioral hierarchy is orchestrated by hierarchical neuronal activity can give us fundamental insights into how nervous systems orchestrate behavior across timescales. Moreover, our investigations hint at a possible CPG circuit for head movements in *C. elegans*. Our experimental approach allowed us to study how CPG circuit activity is embedded into the global patterns of nervous system activity. This question has historically been difficult to answer because of the experimental preparations used to study CPGs;

whole-brain immobilized calcium imaging of neuronal activity in *C. elegans* poses a unique opportunity to study CPG function in intact, immobilized animals.

This thesis aimed to:

1. Perform a nervous-system-wide search for the neurons driving hierarchically-organized behavior
2. Understanding the relationship between the neurons driving hierarchically-organized behaviors.
3. Understanding how the different levels of the hierarchy interact: A hierarchy entails that upper hierarchical levels should influence the lower ones; do we see such relationships? Do lower ones in turn affect the upper levels, thereby suggesting a more complex relationship than a top-down hierarchy?
4. Some of the neurons involved in this hierarchy are toggled between functional roles: how does the nervous system achieve this? These neurons seem to be part of central pattern generator circuits; how is their activity modulated?

4. Results

4.1. Identifying candidate neurons to implement a behavioral hierarchy in *C. elegans*

4.1.1. Expanded experimental imaging setup allows for Whole-Nervous-System interrogation

Recent efforts have established a method for Ca^{2+} imaging of neuronal activity in the head ganglia of immobilized *C. elegans*, at single-cell resolution (Kato et al. 2015; Schrödel et al. 2013; Nguyen et al. 2016; Venkatachalam et al. 2016). Work from the Zimmer lab has shown that in such Ca^{2+} imaging experiments, many neurons in the head ganglia participate in spontaneous, coordinated population activity. These dynamics can be understood through dimensionality reduction methods such as principal component analysis (PCA), which reveals that a low dimensional, cyclical signal dominates the activity of the head ganglia. Calcium imaging of single neurons in freely behaving worms has shown that the activity of many of the neurons that participate in these population dynamics is tightly linked to behavior. By investigating the relationship between single neuronal activity and behavior in freely-moving worms, it has been shown that this brain-wide activity corresponds to the worm's major motor commands: forward movement, backward movement (reversals) and post-reversal turns (simplified as the FWD-REV cycle in this work) (Kato et al. 2015). Thus, a cyclical signal corresponding to the uppermost hierarchical level of our model dominates brain activity in *C. elegans*.

The coordinated dynamics of these neurons persist in imaging conditions that preclude movement and acute sensory stimulation, such that activity patterns can be assigned to forward or reverse motor command states in immobilized worms, as well as suggesting that they are intrinsically driven. This imaging paradigm is therefore ideal for investigating neuronal activity detached from proprioception and sensory inputs caused by locomotion. To delineate the circuits representing the levels of our behavioral hierarchy model, we first expanded our standard whole-brain Ca^{2+} imaging approach to encompass the entire nervous system (Fig. 4.1a, 4.1b), now including the head ganglia, the entire ventral nerve cord (VNC) with many body motor neurons, and tail ganglia (Fig. 4.1c) (Schrödel et al. 2013; Kato et al. 2015; Kaplan et al. 2020). Briefly, the design of the microfluidic device used to immobilize and laterally align worms was improved, such that the animal's head and tail are closer together, thereby reducing the imaging area required to record the activity of all neurons. Additionally, the imaging field of view was expanded by recording with an inverted epi-fluorescence microscope with a 25x objective coupled to a post-acquisition deconvolution step to increase the contrast and resolution of the image data (see Methods for details). With this imaging paradigm, which we refer to as Whole-Nervous-System imaging, we were able to comprehensively record the activity of many sensory-, inter- and motor neurons across the *C. elegans* nervous system.

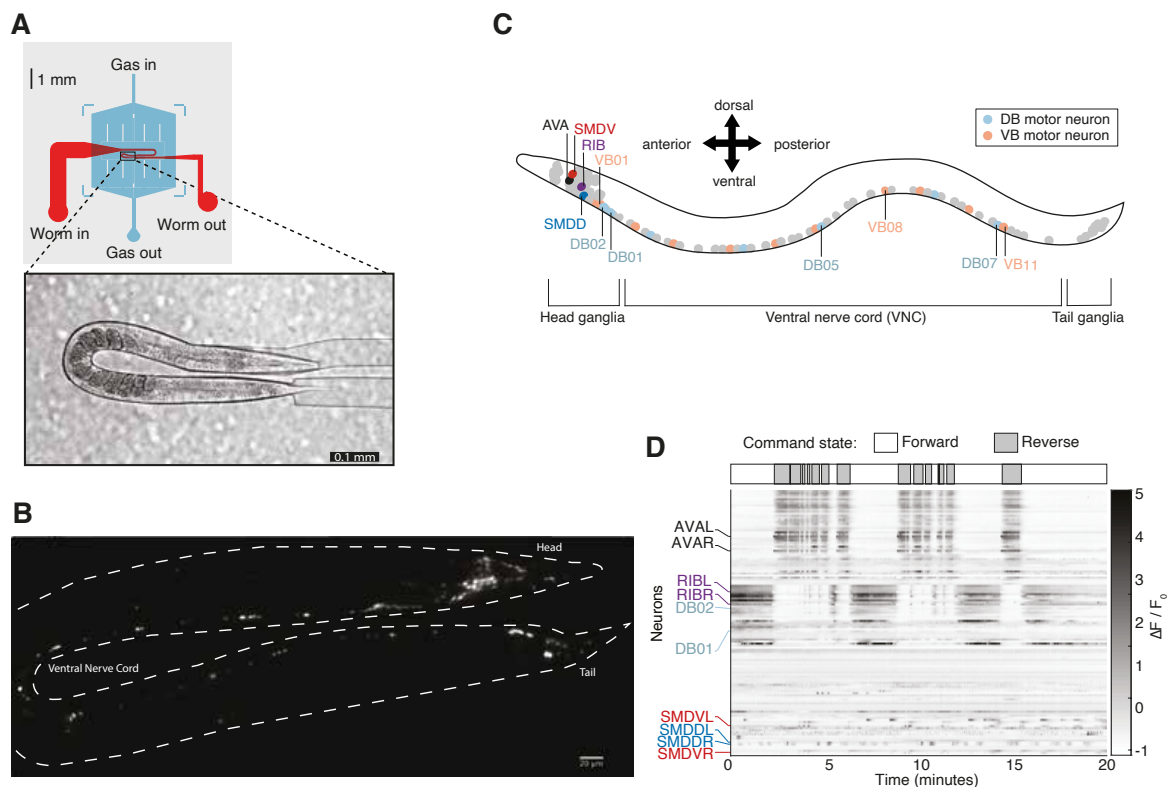


Figure 4.1. Experimental setup for whole-brain and whole-nervous-system imaging. (Adapted from Kaplan et al, 2020) **(A)** Technical drawing of microfluidic device used for whole-brain and whole-nervous-system Ca^{2+} imaging experiments. Black box shows a zoom-in of a phase-contrast image of an example worm immobilized in the imaging curve. **(B)** Example maximum intensity projection of a representative sample recorded in the whole-nervous-system, tetramisole-paralysis imaging configuration under constant conditions. **(C)** Worm schematic. Neurons further investigated in subsequent panels are indicated by colors and labels. **(D)** Example whole-nervous-system GCaMP6f recording. Upper: motor command states inferred from neuronal activity (Methods). Lower: Fluorescence timeseries of 129 neurons, sorted by correlation.

With this imaging paradigm, we generated five datasets capturing the neuronal activity of well-fed, adult *C. elegans*. From each recording, we could extract activity traces from the GCaMP signals of 119 neurons, on average. We then identified many neurons by their characteristic activity patterns, distinct anatomical positions and/or position relative to other identifiable neurons, according to previous work (see Methods) (Kato et al. 2015; Nichols et al. 2017; Skora, Mende, and Zimmer 2018; Uzel, Kato, and Zimmer 2022). Further, we identified the B motor neuron class in the Ventral Nerve Cord (VNC), the SMD head motor neuron class and the PDA neuron with the help of cell-class-specific promoters (see Methods). By sorting neuronal activity by correlation, we could observe that many neurons in these datasets are vigorously active and show coordinated activity patterns (Fig. 4.1d).

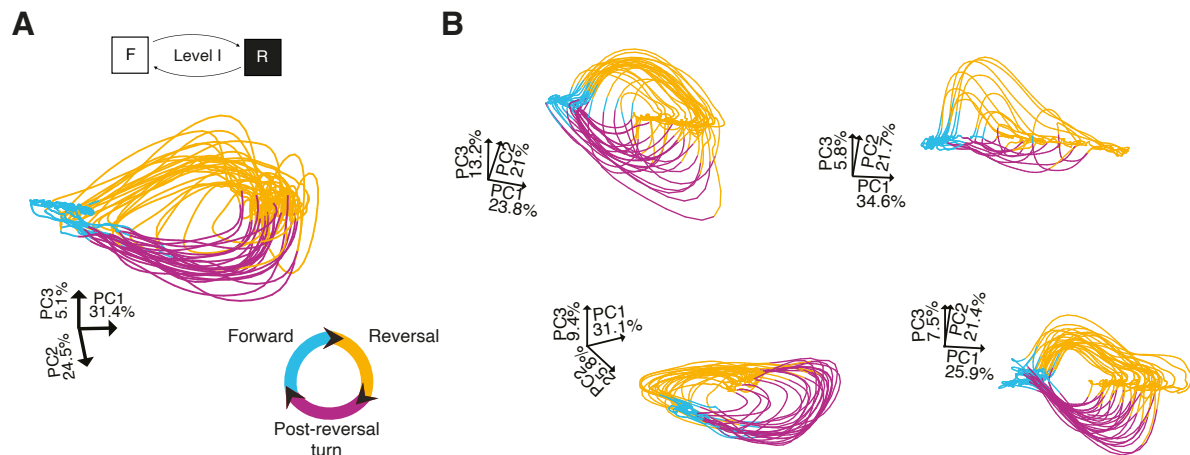


Figure 4.2. A nervous-system-wide representation of the uppermost hierarchical level. (adapted from Kaplan et al, 2020) (A-B) Low-dimensional representation of nervous-system-wide activity cycle, from principal components analysis (PCA). Color key in lower panel indicates motor command state inferred from neuronal activity (Methods; arrowheads indicate directional flow). Coordinates depict PC axes orientations and % variance explained. (A) corresponds to the recording depicted in Fig. 4.1d; (B) represent the remaining whole-nervous-system, tetramisole-paralysis recordings.

4.1.2. Level I: Nervous-system-wide representation of behavior at the uppermost hierarchy level

Then, we used a variation of PCA, a dimensionality reduction technique, to extract the main signals dominating the nervous system in each of these datasets (please see Introduction section 3.5.2, *Neuronal Population Dynamics in C. Elegans*). This PCA variation includes both activity traces and their time derivatives, as both are proven to contain information on different metrics of behavior (see Methods) (Kato et al. 2015; Kaplan et al. 2020). PCA extracts signals shared by many neurons; the Principal Components (PCs) are ordered descendingly according to how much of the variance in the dataset they capture, such that the first 3 PCs capture around 60% of the variance across a dataset and therefore best represent shared neuronal activity (Kato et al. 2015). By plotting the first 3 principal components (PCs) against each other, we can visualize the evolution of nervous system activity over time. This revealed that spontaneous neuronal population dynamics evolve over time and correspond to the cyclical progression through the worm's major motor command sequence (Fig. 4.2). These recurring dynamics are very similar to those previously observed in head ganglia datasets and did not depend on the use of activity traces in addition to the derivative traces (see Introduction section 3.5.2, *Neuronal Population Dynamics in C. Elegans*; (Kato et al. 2015)).

Previous studies have shown that pre-motor interneurons AVA and AVB control the activity of A- and B- motor neurons in the VNC, respectively (Kawano et al. 2011; Xu et al. 2018). These interneurons probably couple interneuron and motor neuron populations to create one coherent signal. Therefore, we asked whether these head ganglia dynamics extend to motor neurons, those motor neurons in the VNC that had not been recorded previously in head ganglia Ca^{2+} imaging. Surprisingly, PCA performed either nervous-system-wide on all measured neurons, only interneurons, or only motor neurons revealed strikingly similar phase portraits (Fig. 4.3), suggesting that network activity that represents the FWD-REV cycle extends from head premotor interneurons to the motor periphery in

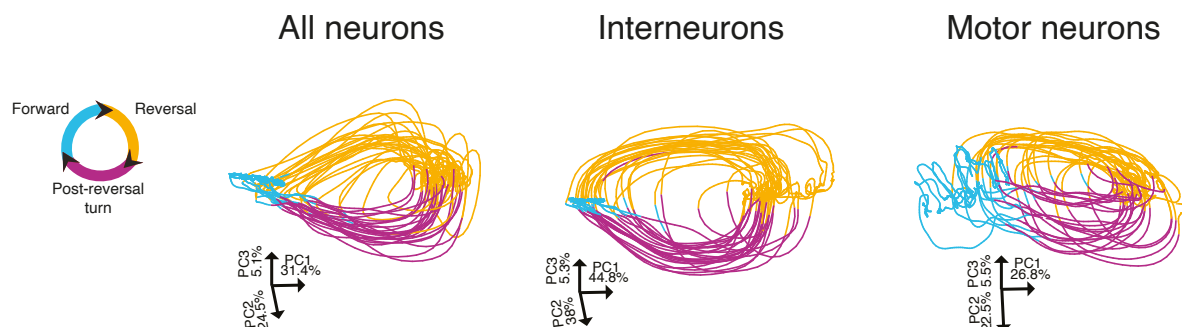


Figure 4.3. Inter- and motor neuron pools represent the uppermost hierarchical level. Low-dimensional representation of neuronal activity cycle, from principal components analysis (PCA) performed on all neuronal traces (left), interneuron traces (middle) or motor neuron traces (right) (see Methods). Color key in the leftmost panel indicates motor command state inferred from neuronal activity (Methods; arrowheads indicate directional flow). Coordinates depict PC axes orientations and % variance explained.

immobilized animals. Similarly, we investigated whether motor- and interneuron activity are represented by the PCs equally well, and whether either neuron pool's activities contained further information than that represented by the PCs. We calculated the Pearson's linear correlation coefficient between the original data and the reconstructed activity traces after PCA for each neuron, which were obtained through matrix multiplication of the PC coefficients with the PC loadings of the top ($i = 1$ to 5) PCs and then adding the mean of the original data (Fig. 4.4) (see Methods). The correlation coefficient serves as a measure of how well the top PCs capture the activity of motor neurons, interneurons, and other neurons; we observed that top PCs represented interneuron and motor neuron

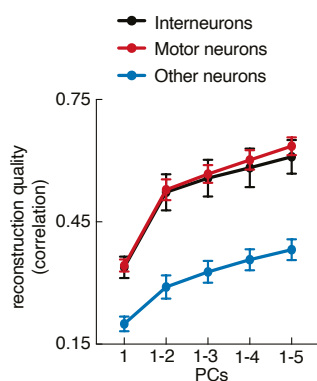


Figure 4.4. Inter- and motor neuron contributions to the representation of the uppermost hierarchical level. (from Kaplan et al, 2020) Mean \pm SEM correlation coefficient between neuronal activity traces and traces reconstructed using indicated top PCs. $n = 5$ datasets.

activity equally well, showing that VNC motor neurons are recruited to and participate in the nervous-system-wide representation of the FWD-REV-TURN cycle despite complete immobilization (Fig. 4.4). Further, we observed that motor neuron activity did not show significantly more

activity fluctuations than interneurons, which hints at a lack of concerted oscillatory activity in the motor neurons. Both motor- and interneurons were strongly modulated by forward/reverse command state, as seen by calculating the difference between each neuron's activity levels in forward and reverse command states (Fig. 4.5; see Table 4.1 for more information and p-values). Thus, nervous system-wide concerted and cyclical neuronal activity represents the worm's major motor commands and represents the uppermost level of our behavioral hierarchy model (Fig. 4.2).

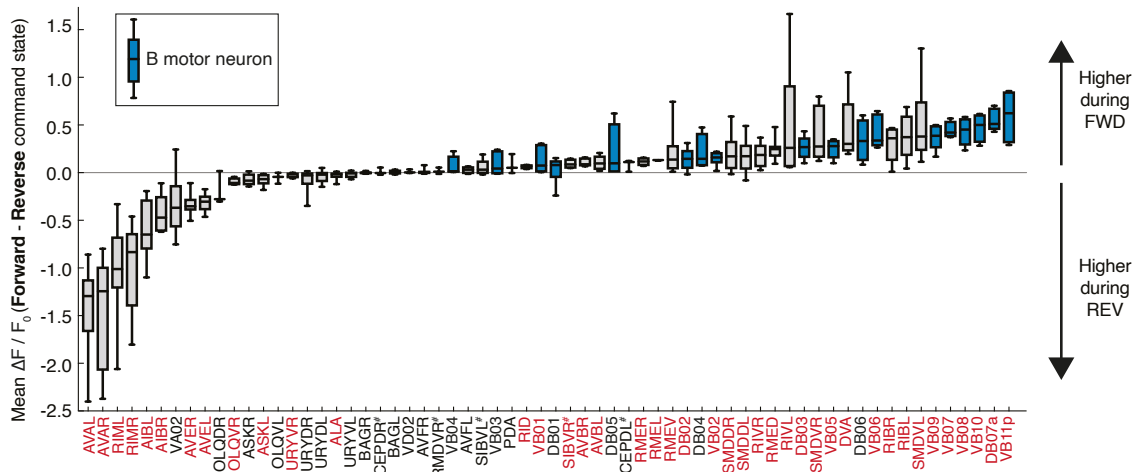


Figure 4.5. Motor- and interneurons were strongly modulated by forward/reverse command state. (from Kaplan et al, 2020) Difference in mean Ca^{2+} activity levels ($\Delta F / F_0$) of all identified neurons during forward vs. reverse commands, pooled from $n = 5$ whole-nervous-system and $n = 5$ whole-brain recordings (in tetramisole paralysis). Boxes: median and interquartile; whiskers: range. Blue boxes correspond to B motor neurons. Neurons labeled in red are those with significantly different mean activity levels in forward vs. reverse commands (paired t-test); see Table 4.1 for p-values and n numbers. #ambiguous IDs, see Methods for alternatives.

4.1.3. Identifying candidate neuronal drivers for hierarchical levels II and III

Having shown that a representation of behaviors at the uppermost hierarchical level permeates the entire nervous system, we set out to find candidate neurons that could drive the lower/faster-timescale level behaviors. Propagated bends and head-casts are rhythmic behaviors and could therefore be driven by central pattern generators (CPGs). CPGs are neurons or neuronal circuits that generate rhythmic/patterned neuronal activity in the absence of patterned sensory input or external feedback (Eve Marder and Bucher, n.d.; Kiehn 2011). To identify CPG candidate neurons, we harnessed the power of immobilized Ca^{2+} imaging, an experimental paradigm that prevents the sensation of dynamic sensory and proprioceptive inputs and is thus ideal for revealing CPG candidates. We found several neurons that showed activity fluctuations within the forward command state, the motor command state where freely-behaving animals execute propagated bends and head-casts, while many others were active within the forward command state but showed no fluctuations within it (Fig. 4.6a).

Next, we systematically screened for potential CPG candidates by detecting peaks in the Ca^{2+} activity traces of all identified neurons and calculating their peak frequencies per forward command state (see Methods). We found neurons with several fluctuations within forward command states (Fig. 4.7a) and set out to narrow down potential candidates. To this end, we devised a statistical method to test whether the inter-peak interval distribution between the detected peaks of each command period was significantly different from a random inter-peak interval distribution (see Methods and Table 4.1 for further information and p-values) by determining which of these neurons showed non-random (i.e. rhythmically active) inter-peak intervals (red names in Fig. 4.7a). Among these were several B-MNs and the SMD head motor neurons; we identified these two neuron classes as great CPG candidates as

they are both excitatory motor neuron classes and they innervate head- and neck muscles in the case of the SMDs, and neck- and body muscles in the case of the B-MNs (Fig. 4.6b). Rhythmic SMD activity under conditions that preclude proprioception indicates that they participate in a CPG circuit. B-MNs have been proven crucial for forward locomotion, further hinting at a role in a propagated bend CPG; and recent studies have proposed the B-MNs plus an unidentified head neuron class as potential CPGs for forward locomotion (Fouad et al. 2018; Xu et al. 2018). Because of their non-random, rhythmic activity within forward command periods, we view these neuronal classes as oscillators and will refer to them as such from here on out.

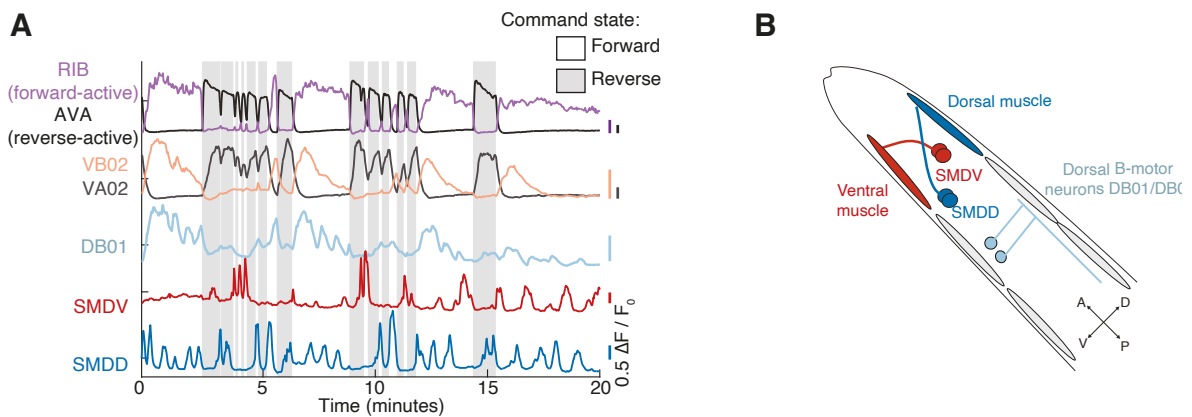


Figure 4.6. Candidate neurons show activity fluctuations within the forward command state (modified from Kaplan et al, 2020) **(A)** Activity traces of selected neurons, corresponds to the recording depicted in Fig. 4.1d. Command states were determined using AVA neuronal activity (see Methods). **(B)** Worm head schematic illustrating positions and lateralized muscle innervations of CPG candidate motor neurons. Cell bodies and projections not shown to scale. A: anterior; P: posterior; D: dorsal; V: ventral.

Conversely, we performed the analysis of peak frequencies on all identified neurons for reversal command states and found that most of the neurons that peaked multiple times per forward command state rarely did so during reverse command states, and none of the neurons analyzed showed statistically-significant, non-random (i.e. rhythmic) peak frequencies for reversal command states (Fig. 4.7b). However, some neurons such as the SMDs did show peak frequencies for both command states, a feature explored in section 4.5.

As previously mentioned, we identified the SMDs and B-MNs as potential oscillators to drive lower-level behaviors of the hierarchy – propagated-bends and head-casts. To determine whether these neurons constituted larger circuits with motor-pattern-like activity, we performed a variant of cross-correlation analysis to calculate so-termed covariograms. Covariograms reveal time relationships between the activity peaks of one neuron relative to another by calculating shuffle-corrected, peri-event time histograms of a neuron’s Ca^{2+} peaks relative to another (see Methods and (Brody 1999)) (Fig 4.8). Covariogram analysis defined three oscillator circuits, each consisting of only motor neurons. The first circuit was composed of SMDD(L/R) and RMED, which oscillated in synchrony (dark blue boxes in Fig. 4.8); the second circuit of SMDV(L/R), RMEV and VB01 oscillating in synchrony, and

antagonistically with SMDD (red boxes in Fig. 4.8); in the third circuit, dorsal B-MNs DB01 and DB02 oscillate in synchrony with only small correlations with the SMDV oscillator (light blue boxes in Fig. 4.8) (see p-values in Table 4.2 and Methods). The covariogram analysis of immobilized Ca^{2+} imaging data revealed functional interactions of SMDs with the RMEs: the RMEs are GABAergic head motor neurons that project to head muscles, such that RMED innervates ventral muscles, while RMEV projects to dorsal head muscles (J. White 2018). In freely behaving worms, they have been involved in the regulation of head bend amplitude in conjunction with SMDs (Shen et al. 2016), our results delineating oscillator circuits in immobilized conditions is in line with such studies.

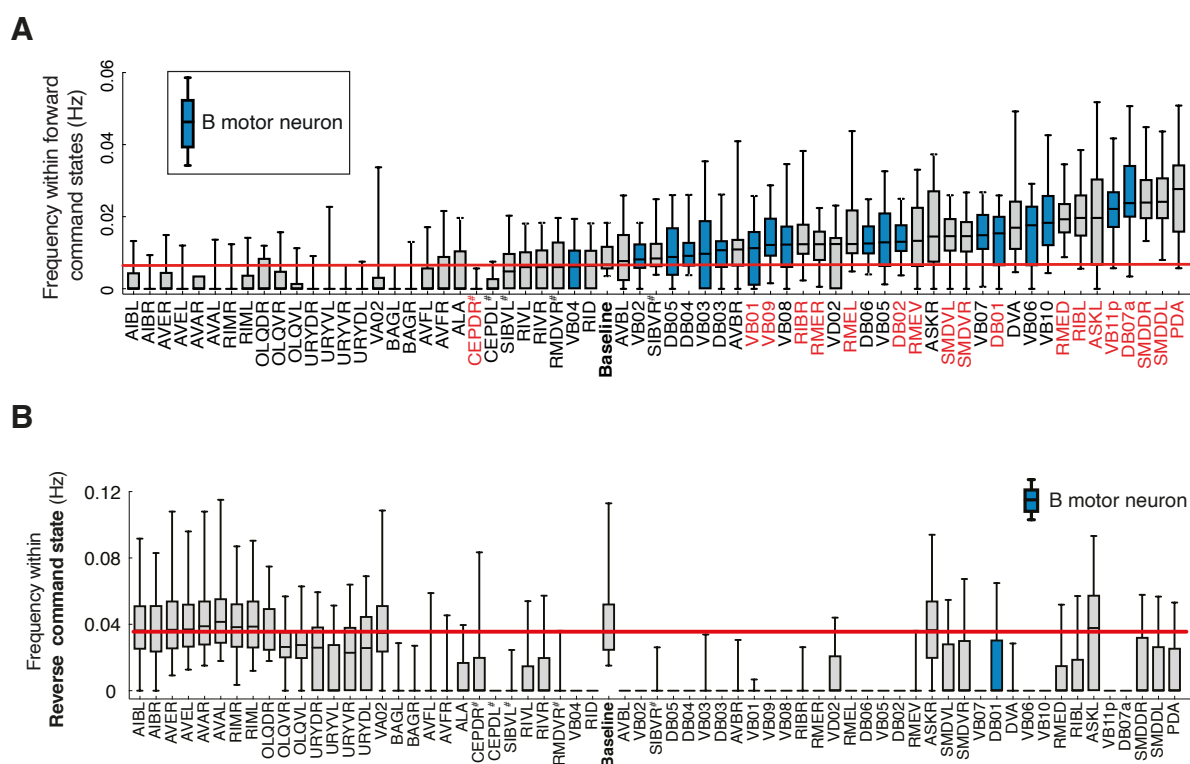


Figure 4.7. Analysis of activity fluctuations within forward/ reverse command periods. (modified from Kaplan et al, 2020) **(A)** Activity peak frequencies within forward command states, with one frequency data point calculated for each forward command state, for all identified neurons, pooled from $n = 5$ whole-nervous-system and $n = 5$ head ganglia recordings. Median, interquartile, and 5-95% range shown. “Baseline” distribution for one peak per forward command state, red line indicates its median. Neurons above “baseline” peaked multiple times within forward command states; of those, red labels indicate significantly non-random inter-peak interval distributions (Methods). See Table 4.1 for multiple-comparison corrected p-values and n numbers (number of forward command states = number of data points, for each neuron). #ambiguous IDs, see Methods for alternatives. **(B)** Frequencies of activity peaks of all identified neurons within reverse command states, with one frequency data point calculated for each reverse command state, pooled from $n=5$ whole-nervous-system and $n=5$ whole-brain recordings. Boxplots show median and interquartile; whiskers show 5%-95% range. “Baseline” is the distribution for one peak per reversal command state; its median is indicated by the red line. Neurons are ordered according to median frequency in forward state. Note that more neurons appear active in the forward state because we only include neuron classes which we reliably identified; we focused on identifying forward-active B-MNs and not reverse-active A-MNs, although we observed strong signals in the latter (data not shown).

Table 4.1. (from Kaplan et al, 2020) Related to Figures 4.5 and 4.7. Second column: Number of instances where each neuron was identified in immobilized Ca^{2+} imaging recordings for the calculation of mean activity level differences in forward vs. reverse command states (**Fig. 4.5**). Third column: p-values for the paired t-test (**Fig. 4.5**). Fourth column: number of forward states per neuron for which peak frequencies were calculated (**Fig. 4.7a**). Fifth column: p-values for inter-peak interval distribution resampling test (**Fig. 4.7a**). This was calculated only for neurons with multiple peaks per forward state, and statistical significance is corrected for multiple comparisons (Methods).

Neuron name	# observations	P-value (Fig. 4.5)	# forward states	P-value (Fig. 4.7a)
AIBL	10	0.000119	56	-
AIBR	10	0.000056	56	-
ALA	10	0.041445	56	0.1691
ASKL	8	0.007442	45	0.000686
ASKR	5	0.053196	25	0.1084
AVAL	10	0.000007	56	-
AVAR	10	0.000021	56	-
AVBL	8	0.003679	42	0.0923
AVBR	5	0.004497	30	0.0862
AVEL	10	0.000001	56	-
AVER	9	0.000016	49	-
AVFL	7	0.077079	37	-
AVFR	8	0.293196	46	-
BAGL	7	0.700558	37	-
BAGR	7	0.831927	37	-
Baseline	-	-	56	-
CEPDL	3	0.153182	20	-
CEPDR	3	0.730871	18	$<10^{-6}$
DB01	9	0.444463	49	1×10^{-6}
DB02	10	0.001824	56	5×10^{-6}
DB03	5	0.008244	26	0.0078
DB04	4	0.111655	21	0.3152
DB05	4	0.247590	21	0.0731
DB06	4	0.053807	22	0.1825
DB07a	5	0.000419	26	1×10^{-6}
DVA	5	0.047722	26	0.0301
OLQDR	3	0.209337	18	-
OLQVL	3	0.249957	19	-
OLQVR	4	0.014049	25	-
PDA	3	0.303379	14	$<10^{-6}$
RIBL	9	0.000788	51	1.1×10^{-5}
RIBR	9	0.001071	51	9×10^{-6}
RID	4	0.007461	24	-
RIML	10	0.000113	56	-
RIMR	9	0.000187	50	-
RIVL	9	0.041139	49	0.0106
RIVR	9	0.002213	49	0.0407
RMDVR	3	0.465273	19	-
RMED	10	0.000043	56	$<10^{-6}$
RMEL	3	0.000169	16	0.0021
RMER	4	0.009923	23	0.0015
RMEV	8	0.045459	46	0.000377
SIBVL	5	0.229044	30	0.2435
SIBVR	4	0.034030	24	0.1493
SMDDL	10	0.007962	56	$<10^{-6}$
SMDDR	9	0.010916	49	$<10^{-6}$

SMDVL	10	0.001672	56	2×10^{-6}
SMDVR	10	0.001490	56	.000234
URYDL	10	0.080583	56	-
URYDR	8	0.107907	45	-
URYVL	9	0.122731	49	-
URYVR	8	0.003887	45	-
VA02	6	0.055074	31	-
VB01	10	0.012811	56	0.000163
VB02	10	0.000033	56	0.1635
VB03	6	0.120118	31	0.0137
VB04	4	0.313493	19	0.4979
VB05	5	0.004762	26	0.0304
VB06	5	0.005444	26	0.0495
VB07	4	0.001905	21	0.0189
VB08	5	0.002505	26	0.0667
VB09	5	0.003075	26	0.0034
VB10	4	0.007944	23	0.0366
VB11p	5	0.007691	26	0.000412
VD02	3	0.464618	18	0.5031

As mentioned in the introduction, CPGs often show rhythm- and pattern-generating activity. Rhythm generation refers to the activity of a neuron or circuit being regularly repeating; pattern generation refers to activity that controls antagonistic muscle groups to generate a locomotion pattern and is coordinated across neurons. The observation that the SMDD oscillator is antagonistic to the

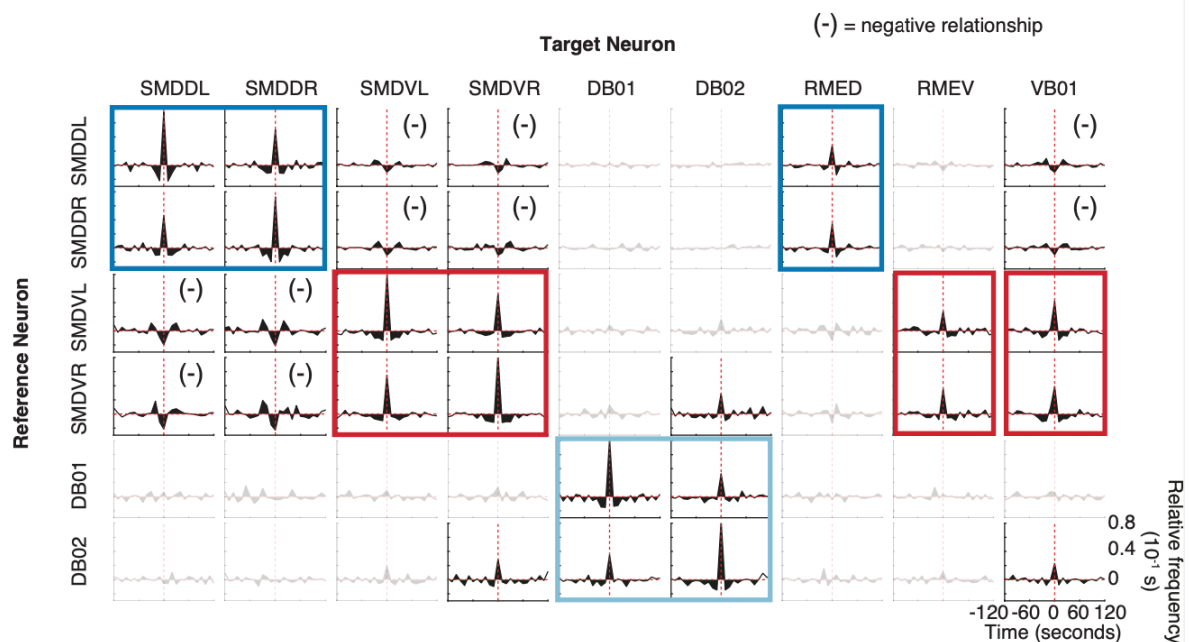


Figure 4.8. Covariograms identify candidate CPG circuits for lower hierarchical levels. (from Kaplan et al, 2020) Covariograms of SMD and DB with all coordinated neurons. All identified neurons were tested, but shown are only those with significant correlation with at least one SMD or DB01/02. Panels show the relative frequencies of Ca^{2+} -peaks of neurons in columns triggered to Ca^{2+} -peaks of neurons in rows. Data are shuffle-corrected so that positive/negative values show higher/lower correlation than chance (Methods). Opaque plots differ significantly from random surrogate distributions (Methods; p-values in Table 4.2). Colored borders denote significant positive relationships consistent within neuron classes. “(-)” denotes negative relationships (Methods).

SMDV oscillator, and vice versa, is consistent with SMD oscillators as rhythm- and pattern-generators for head-bending, where the SMDD oscillator could drive dorsal- and the SMDV oscillator ventral head-bending. On the other hand, the DB01/DB02 oscillator shows a positive relationship between neurons that innervate opposing muscle groups (dorsal-muscle innervating DB01/DB02 with ventral-muscle-innervating VB01), which is in contrast to their muscle innervation patterns and is thus consistent with rhythm generation only. Taken together, these activities suggest a fictive motor pattern in SMD and RME neurons for dorsal/ventral head-neck bending.

Several other B-MNs along the VNC (beyond DB01/DB02) exhibited rhythmic activity peaks (Fig. 4.7a); however, cross-correlation analysis indicated little to no coordination among them, consistent with the rhythm-, but not pattern-generating properties of CPGs (Fig. 4.9, see p-values in Table 4.2 and Methods). Hence, we focused future analysis and imaging efforts on DB01/DB02 and VB01, the B-MNs that showed the most robust functional relationships.

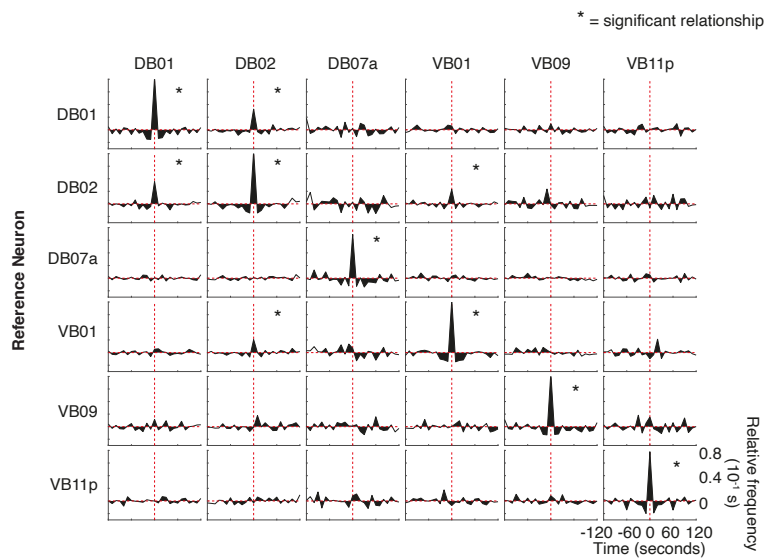


Figure 4.9. B-MNs show little coordinated activity in immobilized animals. (from Kaplan et al, 2020) Covariograms of oscillatory motor neurons. Panels show the relative frequencies of Ca^{2+} -peaks of neurons in columns triggered to Ca^{2+} -peaks of neurons in rows. Data are shuffle-corrected so that positive/negative values show higher/lower correlation than chance (Methods). * significant relationship, after multiple comparison correction. All significant relationships are positive. See Table 4.2 for p-values.

Table 4.2. (from Kaplan et al, 2020) Related to Figures 4.8 and 4.9. P-values for covariogram significance test for covariograms shown in Fig. 4.8 and Fig. 4.9. Statistical significance is corrected for multiple comparisons (Methods).

	SMDDL	SMDDR	SMDVL	SMDVR	DB01	DB02	RMED	RMEV	VB01
SMDDL	$<10^{-6}$	$<10^{-6}$	1×10^{-6}	1×10^{-6}	0.3393	0.4995	$<10^{-6}$	0.003	1×10^{-6}
SMDDR	$<10^{-6}$	$<10^{-6}$	1×10^{-6}	4×10^{-6}	0.2137	0.6218	$<10^{-6}$	0.157	3×10^{-5}
SMDVL	8×10^{-6}	1×10^{-5}	$<10^{-6}$	$<10^{-6}$	0.489	0.005	0.0012	5×10^{-6}	$<10^{-6}$
SMDVR	$<10^{-6}$	5×10^{-6}	$<10^{-6}$	$<10^{-6}$	0.0838	2×10^{-5}	0.0545	$<10^{-6}$	$<10^{-6}$
DB01	0.6151	0.1462	0.4047	0.0793	$<10^{-6}$	$<10^{-6}$	0.4562	0.0152	0.6005
DB02	0.7179	0.8183	0.0042	1×10^{-5}	$<10^{-6}$	$<10^{-6}$	0.1144	0.1501	0.0003
	DB01	DB02	DB07a	VB01	VB09	VB11p			
DB01	$<10^{-6}$	$<10^{-6}$	0.2229	0.6001	0.5037	0.4931			
DB02	$<10^{-6}$	$<10^{-6}$	0.9201	0.0003	0.1873	0.8323			

DB07a	0.6201	0.7833	<10 ⁻⁶	0.2583	0.1385	0.4710			
VB01	0.3821	0.0001	0.6632	<10 ⁻⁶	0.633	0.0137			
VB09	0.4753	0.1413	0.7336	0.72	<10 ⁻⁶	0.2397			
VB11p	0.2352	0.6546	0.3671	0.0068	0.142	<10 ⁻⁶			

Our B-MN covariogram results are consistent with previous studies that identified the B-MNs as distributed rhythm generators in the VNC (Fouad et al. 2018). We wondered whether the lack of coordinated oscillations in B-MNs along the VNC could stem from the fact that tetramisole, the paralyzing agent we used for immobilized recordings, is an acetylcholine-receptor agonist and could therefore alter the activity of many cholinergic neurons, like the B-MNs. To test this, we generated a further Ca²⁺ imaging dataset that captured the nervous system activity (216.4 neurons on average) of five adult *C. elegans* using an alternative paralysis method. The animals were immobilized in microfluidic devices as previously established, but paralyzed through the transgenic expression of histamine-gated chloride channels (*hisCl*) in body wall- and pharyngeal muscles (termed *myo-2::hisCl*, *myo-3::hisCl*, see Methods) (Pokala et al. 2014). In contrast to tetramisole, which paralyzes worms by causing the contraction of their body wall muscles, the *myo-2::hisCl*, *myo-3::hisCl* method paralyzed worms by relaxing their muscles. We observed that paralyzing worms with *myo-2::hisCl*, *myo-3::hisCl* vs. tetramisole leads to differences in the duration of reversal command states, but performing PCA on the neuronal traces (and derivatives) of worms paralyzed with *myo-2::hisCl*, *myo-3::hisCl* showed that the global representation of the FWD-REV cycle persists in the nervous system despite this alternative paralysis method (Fig. 4.10a). In regards to the activity of the B-MNs, we hypothesized that in worms paralyzed with *myo-2::hisCl*, *myo-3::hisCl*, B-MN activity could potentially reflect the alternating activation of dorsal/ventral body-wall muscles that is observed in moving animals, as opposed to the concerted activity of B-MNs in observed in tetramisole-paralyzed animals. Thus, we assessed whether B-MNs in *myo-2::hisCl*, *myo-3::hisCl* show similar activity to that of B-MNs in tetramisole-paralyzed animals. We did not observe any obvious coordinated oscillatory activity of B-MNs within forward command states in *myo-2::hisCl*, *myo-3::hisCl* paralysis either (Fig 4.10b).

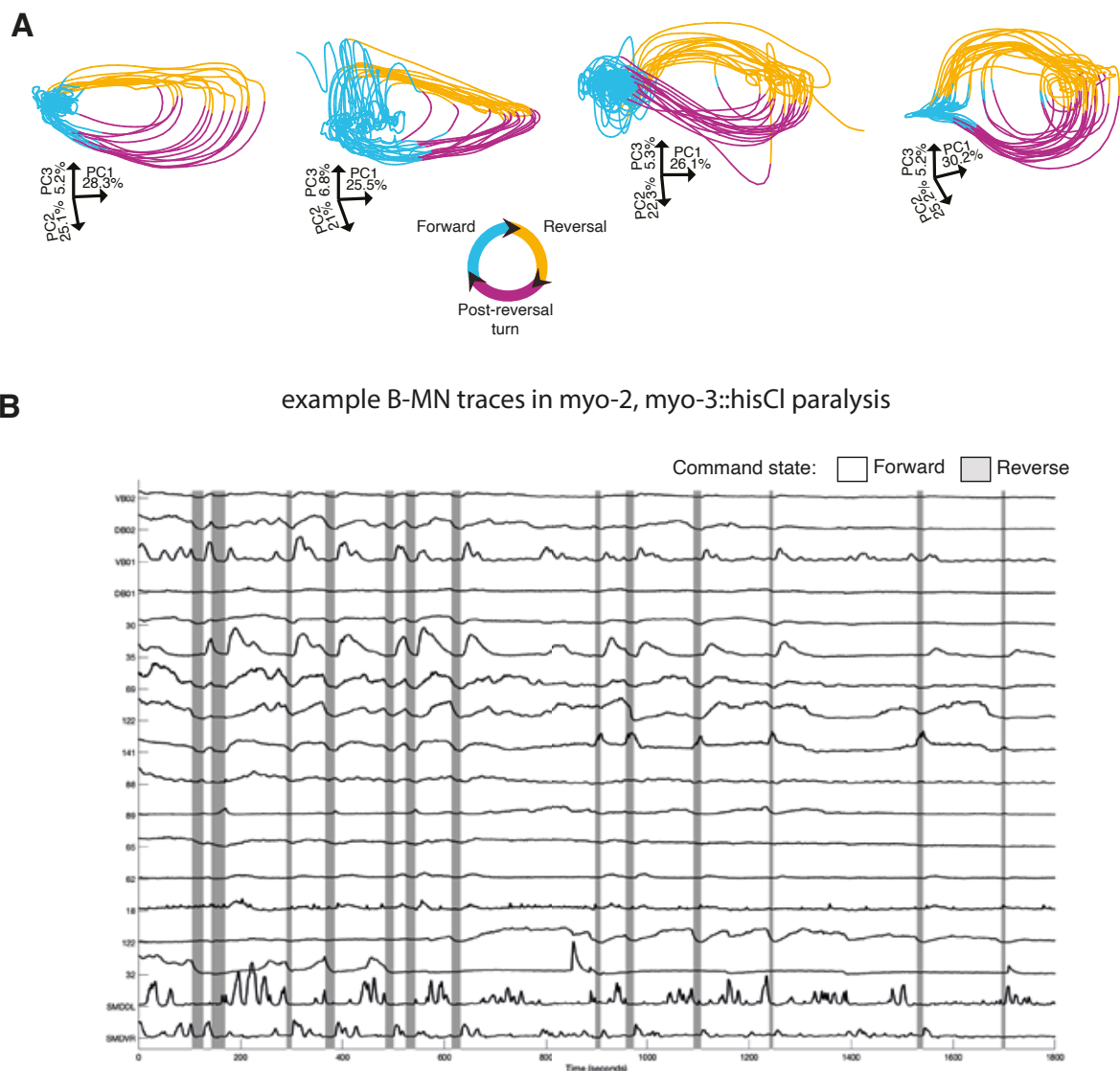


Figure 4.10. Alternative paralysis method confirms global representation of uppermost hierarchical level and does not reveal further coordination among B-MNs. (A) Low-dimensional representation of nervous-system-wide activity cycle, from principal components analysis (PCA) on whole-nervous-system imaging of *myo-2::, myo-3::hisCl*-paralysed animals. Color key in lower panel indicates motor command state inferred from neuronal activity (same color code as Figure 4.2-4.3). Coordinates depict PC axes orientations and % variance explained. (B) Activity traces of SMD, B-MNs and B-MN candidates from representative recordings. Command states were determined using AVA neuronal activity (see Methods).

Proprioception has been described in B-MNs, as well as in the SMDs (Wen et al. 2012; Xu et al. 2018; Yeon et al. 2018). We hypothesize that proprioceptive feedback is a requirement for more complete motor patterns in the B-MNs (i.e. alternating dorso-ventral, propagated body bends posterior to the neck region) and higher frequency oscillations in SMDs and B-MNs. This hypothesis is in line with previous characterizations of CPGs reporting 10-fold decreases in CPG frequencies in intact animals vs. CPG preparations (Fox, Soll, and Wu 2006; Goulding 2009). Thus, we imaged the neuronal activity of SMDs or DB02 in freely-moving animals. To this end, we placed worms expressing mCherry and GCaMP6f in SMD or DB02 between a chunk of agar and a coverglass to constrain their movement to two dimensions, and imaged the neuronal activity of moving worms using an inverted compound

microscope which tracked the neurons of interest in space and re-centered them onto the objective, using the system described in (Faumont, Lindsay, and Lockery 2012) (see Methods for further details). Then, we measured the frequencies of SMD and DB01 activity peaks in freely-moving animals and compared them to those observed in immobilized animals. We observed an approximately 10-fold decrease in SMD and B-MN frequencies upon immobilization (Fig. 4.11). This decrease is consistent with other CPG studies (Fox, Soll, and Wu 2006; Goulding 2009). Thus, we further hypothesize that proprioceptive inputs are required for frequency entrainment of B-MNs and SMDs. We next focused on the SMD and DB oscillators and their relationship to head-bending.

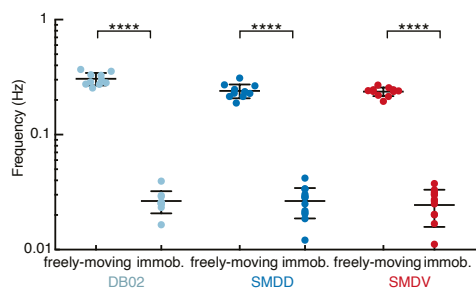


Figure 4.11. Immobilization leads to a consistent 10-fold decrease in CPG candidate frequencies. Frequency of detected activity peaks of DB02, SMDD and SMDV motor neurons in freely-moving and immobilized animals. Each data point from one animal, n=10 (DB02 freely-moving), n=10 (DB02 immobilized), n=11 (SMDD freely-moving), n=13 (SMDD immobilized), n=11 (SMDV freely-moving), n=13 (SMDV immobilized). Note the log scale of the y-axis. ****p<0.0001, unpaired, two-tailed t test.

4.2. B- and SMD motor neurons are required for propagated bends and head casts, respectively

Next, we examined how the SMD and DB oscillators interact in immobilized worms. Because the SMD and DB01/02 are located in the head ganglia area and whole-brain imaging recordings yield higher-quality data (see Methods), we decided to perform whole-brain imaging as opposed to whole-nervous-system imaging from this point onward. We first tested whether SMD and DB01/02 can oscillate independently from each other. To this end, we inhibited each independently and transiently using hisCl; we targeted the SMDs with a cell-class-specific promoter combination, and since no genetic driver was available to target DB01/-2 specifically, we used a promoter for cholinergic motor neurons in the VNC, including all B-MNs (VNC_{ACh}) (see Methods). We recorded the neuronal activity of the head ganglia of five SMD-inhibited- ($SMD::hisCl$) and four VNC_{ACh} -inhibited ($VNC_{ACh}::hisCl$) animals. $SMD::hisCl$ whole-brain recordings revealed that DB01/02 can oscillate in the absence of SMD activity (Fig. 4.12a), though we did observe a small reduction of DB01 frequency (Fig. 4.12b). Conversely, in $VNC_{ACh}::hisCl$ recordings we observed a slight increase in SMDD- and a strong decrease in SMDV- peak frequency in forward command states (Fig. 4.12c-d).

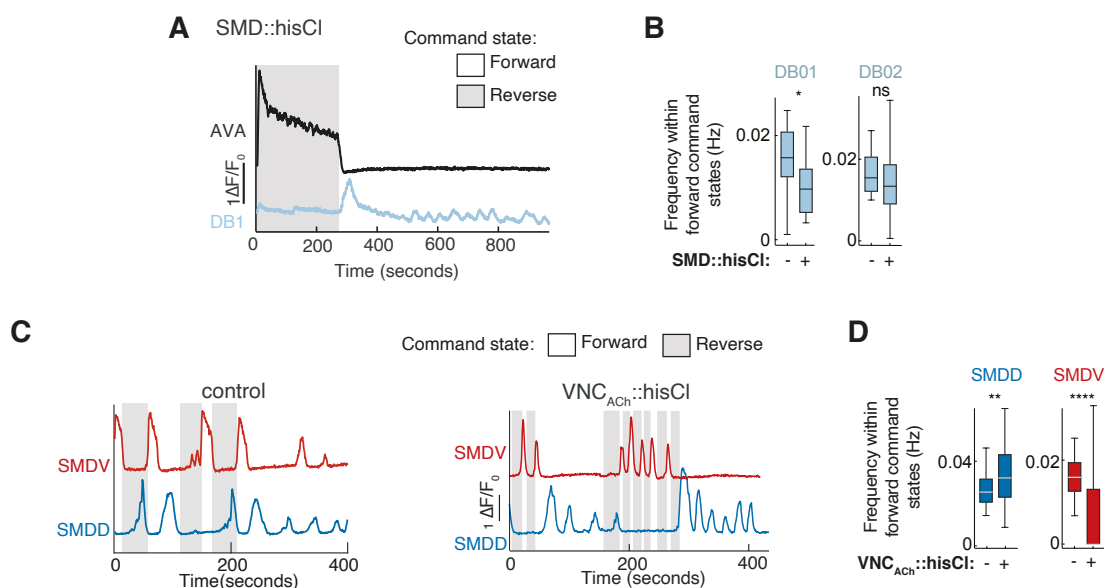


Figure 4.12. DB motor neurons show activity fluctuations during SMD inhibition. (modified from Kaplan et al, 2020) (A) Example GCaMP activity traces of AVA and DB01 neurons in an immobilized, SMD-inhibited animal (SMD::hisCl). Command states were determined using AVA neuronal activity (see Methods). (B,D) Frequencies as in Figure 4.7a for the indicated neurons in control, VNC_{ACh}-inhibited, and SMD-inhibited animals, pooled across paired neurons, and across $n = 5$ (control, SMD::HisCl) or 4 (VNC_{ACh}::HisCl) recordings. * $p < 0.05$, ** $p < 0.01$, **** $p < 0.0001$, Mann-Whitney test. ns, not significant. Boxplots show median, interquartile, and range. (C) Example SMD activity traces from an immobilized, control recording (left) and from a VNC_{ACh}-inhibited animal (VNC_{ACh}::hisCl, right). Command states were determined using AVA neuronal activity (see Methods).

The differential effect of VNC_{ACh} inhibition on SMDD/SMDV could be explained by inhibition of ventral B-MN VB01, as VB01 is the only B-MN electrically connected to the SMDs through a gap junction to SMDV(R) (J. G. White et al. 1986; Witvliet et al. 2021). In line with this, VB01 and SMDV activities are positively correlated during forward command states in unperturbed animals (Fig. 4.8, Fig. 4.13a), and inhibiting the SMDs abolished VB01 activity (Fig. 4.13b). This relationship between VB01 and SMDV will be explored further in section 4.3, nevertheless, these manipulations show that SMDD and DB01/02 can operate as independent oscillators.

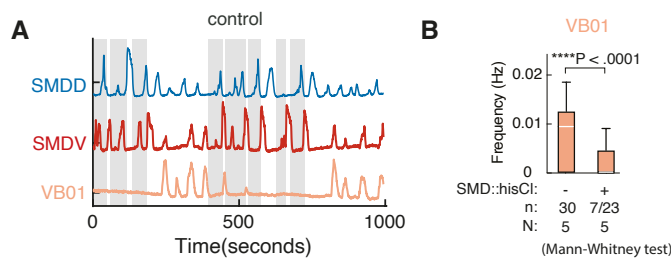


Figure 4.13. VB01 and SMDV activities are interrelated. (A) Example GCaMP activity traces of SMD and VB01 neurons in an immobilized animal. Command states were determined using AVA neuronal activity (see Methods). (B) VB01 frequencies as in Figure 4.7a in control and SMD-inhibited animals, pooled across $n = 5$ recordings for each condition. * $p < 0.05$, ** $p < 0.01$, **** $p < 0.0001$, Mann-Whitney test. ns, not significant. Boxplots show median, interquartile, and range.

reversals distinct from head-casting. In fact, inhibiting the SMDs led to a decrease in head-bend angle, but only during forward locomotion (Fig. 4.16). This possibility is explored in section 4.5.

4.3. Level I and II interaction: Upper hierarchical level toggles activity of middle- and lower-level neurons

Next, we aimed to understand whether the activities of the SMDs and DB01/02 are modulated by the FWD-REV cycle (Fig. 4.17a), a hypothesis consistent with our behavioral hierarchy model. This

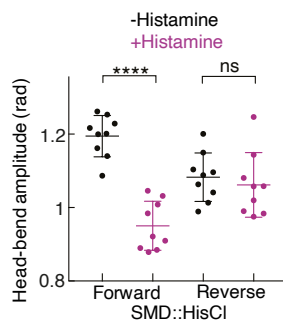


Figure 4.16. Relationship between SMD activity and head-bending amplitudes is restricted to forward locomotion. (from Kaplan et al, 2020) Peak head-bend amplitudes in SMD::hisCl animals, mean \pm SD. **** $p < 0.0001$ Mann-Whitney Test; ns, not significant.

idea is also in line with the previous observation that many neurons, among them several B-MNs, are upregulated in the FWD command state in immobilized worms (Fig. 4.5). We performed Ca^{2+} imaging in freely moving worms for DB02 and SMDs (see Methods). Then, we extracted their calcium activity peaks and quantified the frequencies

and mean amplitudes of DB02/SMD peaks in both behavior states separately (see Methods). We observed a decrease in DB02, SMDD and SMDV peak frequencies and mean amplitudes in reverse locomotion when compared to forward locomotion (Fig. 4.17b). Thus, the upper hierarchical level toggles DB02, SMDD and SMDV between distinct activity states in freely-moving worms. We then wondered whether this hierarchical control depended on proprioceptive feedback or whether it was network-based and thus arose from intrinsic circuit properties. To disentangle this, we again made use of the whole-brain Ca^{2+} imaging paradigm, where neuronal activity is decoupled from proprioception due to immobilization, and saw a decrease in DB02 frequency and SMDD peak amplitude during reverse command states (Fig. 4.17c), as we had seen in freely behaving worms (Fig. 4.17b). These results suggest that the hierarchical control of neuronal activity is a circuit property and independent of behavioral execution. Interestingly, we saw no significant modulation of SMDD or SMDV frequency or SMDV peak amplitude in immobilized animals. To summarize, SMD and DB oscillations are toggled within the overarching forward/reverse command cycle and this hierarchical control occurs partly via circuit interactions.

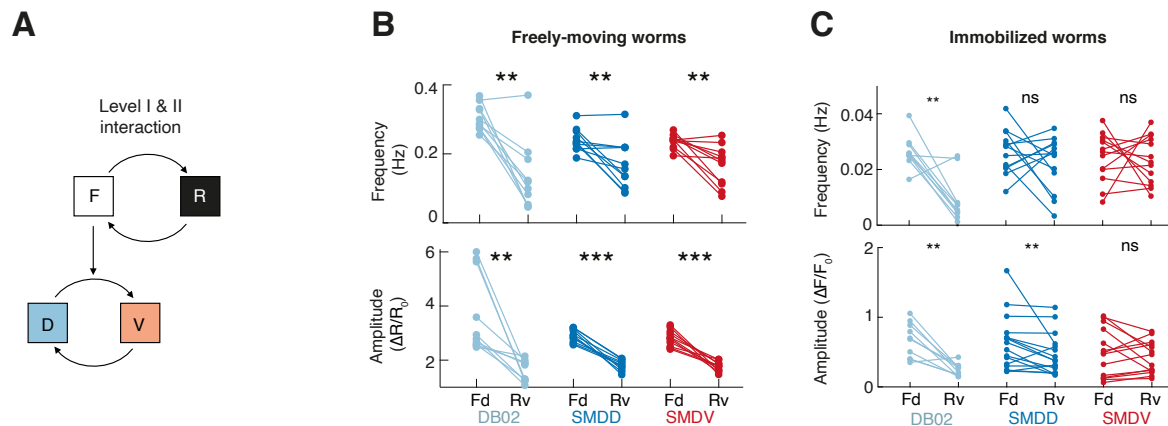


Figure 4.17. Upper hierarchical level toggles activity of middle- and lower-level neurons. (from Kaplan et al, 2020) **(A)** Hierarchy levels investigated. **(B)** Frequency (upper) and average amplitude (lower; R = GCaMP/mCherry ratio) of detected activity peaks of SMD and DB02 in freely behaving animals. ****** $p < 0.01$, ******* $p \leq 0.001$, Wilcoxon matched-pairs signed rank test. Each data point from one animal, $n=11$ (SMD) and $n=10$ (DB02). **(C)** Frequency (upper) and mean amplitude (lower) of DB02 ($n=10$), SMDD ($n=16$) and SMDV ($n=14$) GCaMP activity peaks in forward and reversal command states across whole-brain and whole-nervous-system recordings. ****** $p < 0.01$, Wilcoxon matched-pairs signed rank test. ns, not significant.

4.4. Level II and III interaction: Investigating the relationship between SMD and B-MN activities

4.4.1. Correlations between B-MN and SMD and propagated-bends and head-casts

Propagated-bends and head-casts are tightly linked, as head-casts occur at specific phases of the propagated-bend cycle (phase nesting, see section 3.4 and Fig. 3.1e-f). Naturally, we sought to understand whether the hierarchical organization of these behaviors would be reflected in the activity of the neurons that drive them (Fig. 4.18a). We imaged SMD/DB02 activity in freely moving animals, while recording their behavior. Briefly, we imaged the neuronal activity of moving worms whose movement was constrained to two dimensions by placing them between a chunk of agar and a coverglass. We expressed mCherry and GCaMP6f in SMD or DB02, and imaged their neuronal activity using an inverted compound microscope which tracked the neurons of interest in space and re-centered them onto the objective, using the system described in (Faumont, Lindsay, and Lockery 2012). We recorded the worms' behavior simultaneously with their neuronal activity (see Methods). Then, we examined how SMD/DB02 neuronal activity related to propagated-bends and head-casts.

To this end, we used kymograms, which are representations of worm posture over time, to identify propagated-bends and head-casts, depending on the final propagation segment of a head bend (see introduction section 3.5., and Methods). Then, we calculated average kymograms, triggered to either dorsal or ventral propagated-bends (Fig. 4.18b-c), and dorsal or ventral head-casts (Fig. 4.18d-e), and calculated the average neuronal activity of DB02 and SMD activity during these behavioral events (see Methods). We found a strong link between the activities of all neurons to propagated-bends, as they showed fluctuations synchronized with propagated-bends. DB02 and SMDD oscillations co-occurred with dorsal propagated bends and not ventral propagated-bends, in line with these neurons' innervation of dorsal body wall muscles (Fig. 4.18b-c) (J. G. White et al. 1986). Conversely, ventral-

muscle-projecting SMDVs showed activity during ventral propagated-bends but not dorsal propagated-bends; the alternation of dorsal and ventral propagated-bends was also mirrored by alternating SMDD and SMDV activity peaks (Fig. 4.18c) (J. G. White et al. 1986).

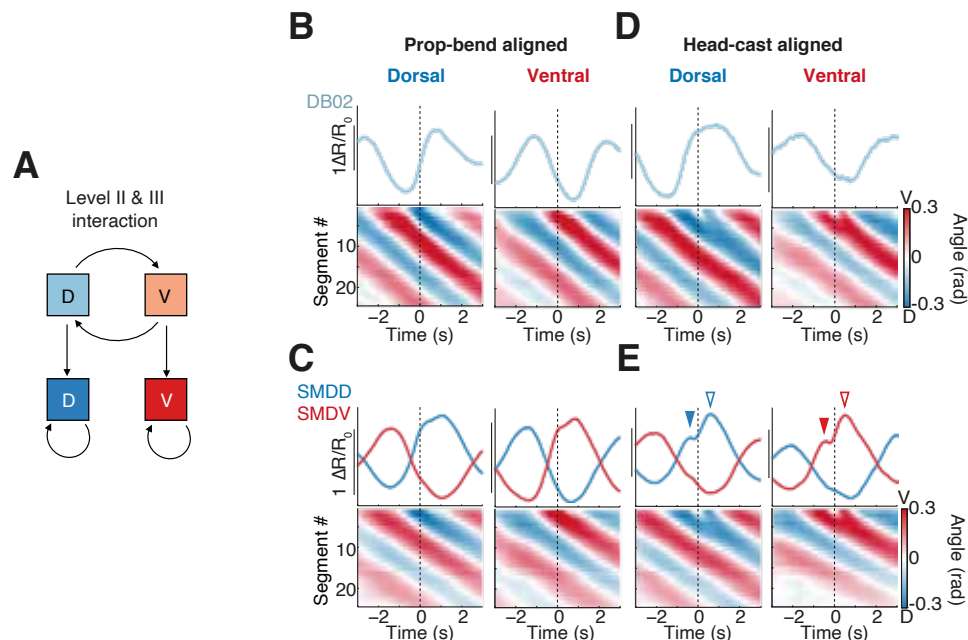


Figure 4.18. Relationships between oscillator activities and hierarchical behaviors. (from Kaplan et al, 2020) (A) Hierarchy levels investigated. (B-E) Trigger-averaged Kymograms (lower) and neuronal activity traces (upper; $R = \text{GCaMP}/\text{mCherry}$ ratio) from DB02 (B, D) and SMD (C, E) imaging, aligned to either propagated-bends without subsequent head-casts (B-C) or initial head-casts (D-E). Left to right, $n = 669, 680, 303, 101$ (B,D) and $n = 377, 360, 178, 119$ (C,E). In (E), activity peaks during propagated-bends (filled arrowheads) and head-casts (open arrowheads) denoted. Data pooled across 11 (SMD) and 10 (DB02) animals.

In regards to head-casting, we found no further oscillations in DB02 activity beyond those associated with dorsal propagated-bends (Fig. 4.18d). Interestingly, SMD activity showed peaks coinciding with propagated-bends, as previously mentioned, and showed an additional activity peak overlapping with head-casts (Fig. 4.18e, see filled arrowheads for propagated-bends and empty arrowheads for head-casts). This activity was lateralized such that SMDD oscillated during dorsal-directed head-casts following dorsal propagated-bends, and SMDV oscillated during ventral-directed head-casts following ventral propagated-bends. In contrast to their propagated-bend-activity, SMDD and SMDV did not alternate during head-casts: SMDV was silent while SMDD was active during dorsal head-casts, and vice versa (Fig. 4.18e). To summarize, DB02 activity coincided with dorsal propagated-bends only, while SMDs showed separable activity profiles during propagated-bends and head-casts: SMDD/V alternated during dorsal/ventral propagated-bends, while during dorsal/ventral head-casts, they showed unilateral SMDD- or SMDV-only oscillations, respectively.

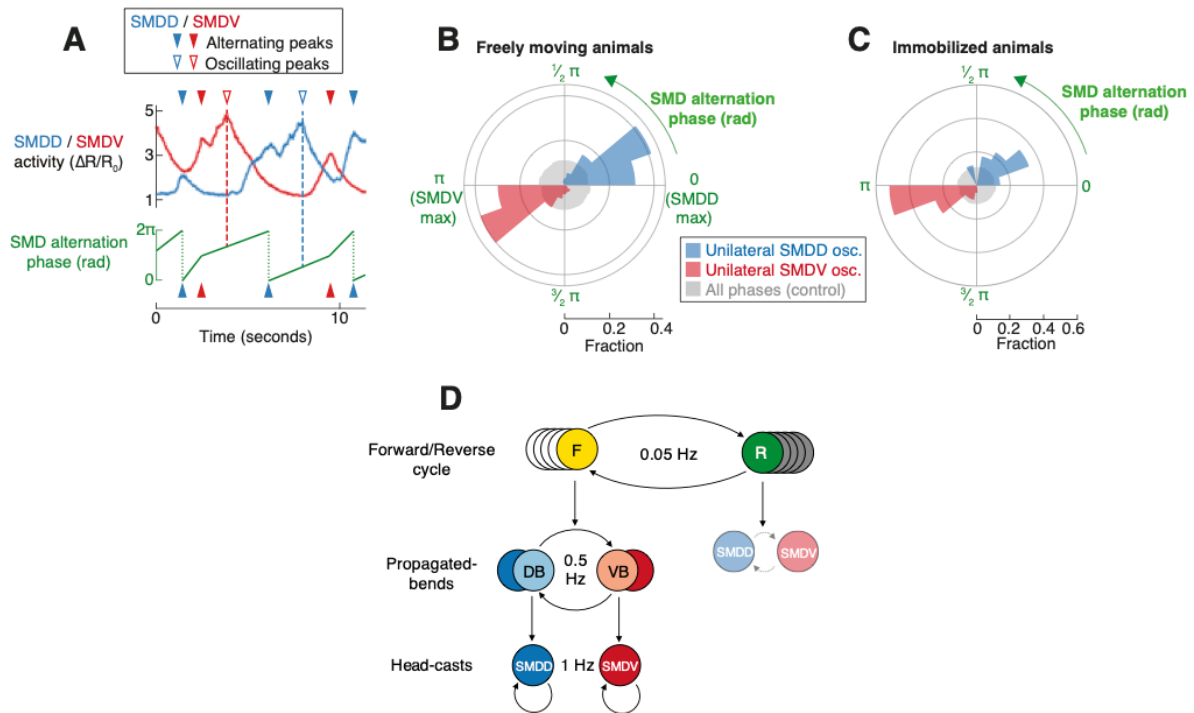


Figure 4.19. Hierarchy level II and III interaction: phase-nesting of SMD activity. (from Kaplan et al, 2020) **(A)** Example SMD activity time series illustrating SMD alternation phase measurement. Red and blue dashed lines indicate unilateral SMDD-only or SMDV-only oscillations. **(B-C)** Fractional distributions of unilateral SMDD-only or SMDV-only oscillations binned according to SMD alternation cycle phase, in freely moving **(B)** or immobilized **(C)** animals. $n = 196$ **(B, SMDD)**, 147 **(B, SMDV)**, 57 **(C, SMDD)** and 23 **(C, SMDV)**. $p \leq 10^{-6}$ for each SMD distribution in **(B)** and **(C)** indicates the probability that distributions are drawn randomly from the full data distribution shown in grey (Methods). Data in **(B)** pooled across 11 (SMD) and 10 (DB02) animals. Data in **(C)** pooled from 13 animals. **(D)** Neuron classes (F = forward-active neurons, R = reverse-active neurons) underlying each behavior.

4.4.2. Phase nesting of B-MN and SMD activity

As discussed in the introduction section, head-casts occur at restricted phases of the propagated-bend cycle, a relationship termed phase-nesting. SMDs showed activity peaks co-occurring with both propagated-bends (alternating) and head-casts (unilateral). Naturally, we wondered whether head-cast-related SMD activity could also be phase-nested. To investigate this, we exploited the fact that SMDD and SMDV alternated peaks with one another during propagated-bends, whereas during lateralized head-casts, one SMD oscillated while the other SMD remained silent. This allowed us to use SMD alternating peaks to quantify the phase of SMDD/SMDV alternation cycle by converting a sequence of three alternating peaks (SMDD – SMDV – SMDD) into a cycle ($0 - 1 - 2\pi$ rad) (Fig. 4.19a, see Methods). This would correspond to the propagated-bend cycle. Then, we calculated the fraction of SMDD-only or SMDV-only oscillations that occurred at each phase of the SMD alternation cycle and plotted this as a polar histogram (Fig. 4.19b). We observed that unilateral SMD oscillations occurred at specific phases of the SMD alternation cycle, and were thus phase-nested, in a similar manner to the co-occurring behaviors (compare Fig. 3.1f with Fig. 4.19b). Given the importance of SMD activity in head-casting (established in section 4.2), these findings suggested that phase-nested SMD activity could underlie the phase-nested organization of behavior. Alternatively, phase-nested

behavior and phase-nested SMD activity could simply arise from biomechanical constraints which would require head-casts to occur at distinct phases; and phase-nested behavior could be reflected in SMD activity through proprioception. If phase-nesting in SMD neuronal activity arises from circuit mechanisms and does not require proprioception, it should prevail despite immobilization. We performed the same analysis on immobilized worm data and found that SMD activity patterns were also phase-nested (Fig. 4.19c), indicating that this organization is a property of the neural circuit independent of behavioral execution and proprioceptive feedback. Phase-nested SMD activity therefore provides a potential mechanism for phase-nested behavior: SMDD-only or SMDV-only oscillations each occur during specific windows of the SMD alternation cycle, driving head-casts only at specific propagated-bend phases. In summary, two different timescale behaviors are tightly coordinated via phase-nested neural oscillators. Further, neuronal activity and thus behavior are hierarchically organized across three timescales, through phase-nesting (Fig. 4.19d).

4.4.3. How are propagated bends and head casts coupled? Investigating the role of gap junction proteins in SMDV and VB01 activity

We observed that B-MN activity drives and correlates to propagated-bends while SMD activity drives and correlates to head-casts (Fig. 4.14, Fig. 4.18); and that SMD activity shows signatures of both behaviors (Fig. 4.18c, e). These observations spawned following hypotheses: First, that this propagated-bend-related SMD activity could serve to coordinate propagated-bends and head-casts. Secondly, this signal must be relayed to the SMDs, given that B-MN activity, and not SMD, drives propagated-bends (Fig. 4.14b). The possibility that propagated-bend-related signals are generated in SMD through proprioception could be ruled out since we observed them in immobilized animals, too. We set out to understand how the propagated-bend cycle is relayed onto SMD and hypothesized that the B-MN oscillation drives the SMD alternation cycle correlated to propagated-bends (Fig. 4.19d). Indeed, B-MN-inhibited animals ($VNC::hisCl$) showed a loss of SMD alternations in immobilized worms (Fig. 4.12c-d). As mentioned in section 4.2, B-MNs are coupled to the SMDs through a single gap junction connection between VB01 and SMDV(R), and SMDV and VB01 activities are correlated in immobilized worms (Fig. 4.13a) (J. G. White et al. 1986). In fact, SMD inhibition in immobilized animals resulted in decreased VB01 activity during forward command states, possibly through the co-inhibition of VB01 through its gap junction connection to SMDV (Fig. 4.13b). We hypothesized that the VB01–SMDV connection could link the propagated-bend cycle and SMD activity. However, while $SMD::hisCl$ showed decreased VB01 activity (Fig. 4.13b), $VNC_{ACh}::hisCl$ showed decreased SMDV activity (Fig. 4.12d), making it difficult to draw conclusions about causality in the circuit.

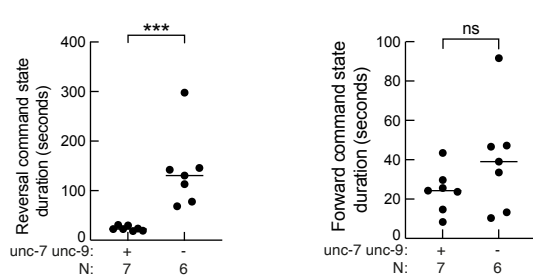


Figure 4.20. *unc-7 unc-9* gap junction disruptions affect reversal command state durations. Mean reversal (left) and forward (right) command state durations across whole-brain recordings. Each data point is from one animal. - denotes lack of mutations; + denotes presence of mutations. Control: N=7; *unc-7, unc-9*: N=7 recordings. ns, not significant; *p<0.05, **p<0.01, ***p<0.001, ****p<0.0001, ns not significant; Mann-Whitney Test.

Next, we aimed to investigate the importance of the VB01-SMDV gap junction for SMD activity. Ideally, we could disrupt the VB01-SMDV gap junction specifically while avoiding co-inhibition. Thus, we set out to find gene promoters to specifically target VB01 or promoter combinations that would only overlap in VB01, but these efforts were not successful (not shown). We opted for a genetic mutant approach to disrupt gap junctions in many neurons, including VB01 and SMDV, and assess the effect of lack of gap junctions on SMD and VB01 activity. Specifically, we imaged the neuronal activity of *unc-7 unc-9* innexin mutants in the immobilized whole-brain imaging paradigm (see Methods). We chose these genes because UNC-7 and UNC-9 are innexin components present in many neurons in *C. elegans*, among them in SMD and VB motor neurons (T. Starich et al. 2009; Altun et al. 2009). First, we quantified the average forward/reversal command state duration in *unc-7 unc-9* mutant worms, and found that reversal command states became much longer, while forward command state durations remained unaffected (Fig. 4.20). However, since this manipulation affects many neurons, it is hard to draw conclusions from this observation.

Focusing on SMD and VB01 activity in *unc-7 unc-9* mutants, SMD neurons were still active during reverse command states, while their activity was greatly decreased during forward command states (Fig. 4.21a, compare to Fig. 4.13a). On the other hand, VB01 activity was preserved (Fig. 4.21a). In fact, we calculated the cross correlation between VB01 and SMDV activity traces in unperturbed animals and in *unc-7 unc-9* mutants and observed a loss of correlation between VB01 and SMDV in *unc-7 unc-9* mutants (Fig. 4.21b).

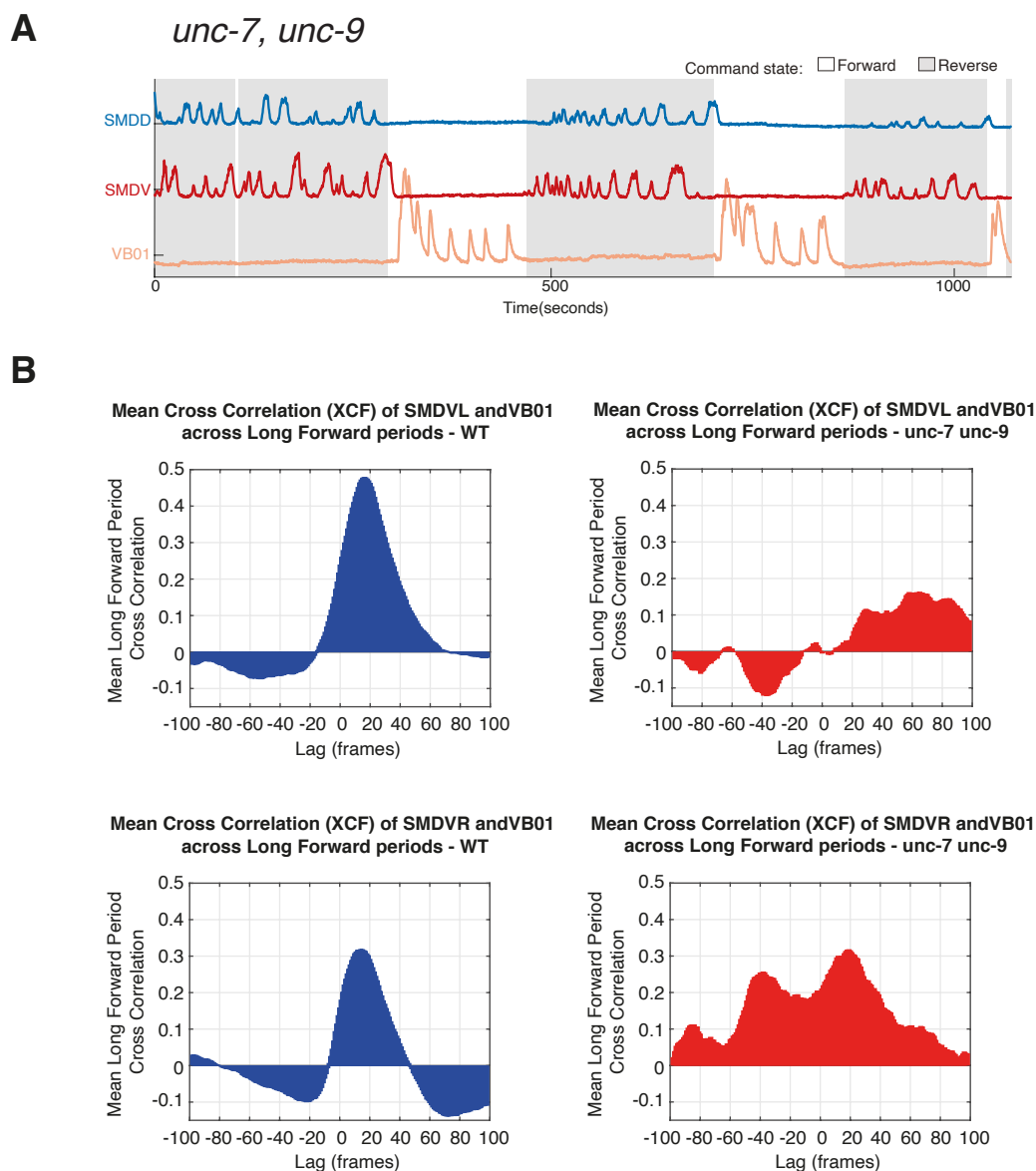


Figure 4.21. *unc-7 unc-9* gap junction disruptions affect SMDV and VB01 correlation. (A) Example GCaMP activity traces of SMD and VB01 neurons in an immobilized, *unc-7 unc-9* mutant animal. Command states were determined using AVA neuronal activity (see Methods). (B) Mean cross correlation across forward command periods of SMDVL (top)/ SMDVR (bottom) and VB01 across control (left) and *unc-7 unc-9* (right) animals in immobilized, whole-brain imaging recordings. P values were calculated using the `kstest2` MATLAB function (Mathworks); * $p < 0.05$, ** $p < 0.01$, *** $p < 0.001$, **** $p < 0.0001$; ns, not significant. The SMDV x VB01 cross correlations in *unc-7 unc-9* mutants were significantly different than WT (SMDVL x VB01 $p = 4.0627 \times 10^{-5}$; SMDVR x VB01 2.0848×10^{-46}).

Additionally, we observed that activity peaks of SMDDL/R and SMDVL/R neuron pairs, whose activities are highly correlated in unperturbed animals, were uncoordinated in *unc-7 unc-9* mutants (data not shown). Therefore, we quantified the mean amplitude and frequency of all four SMDs (SMDDL, SMDDR, SMDVL, SMDVR) and VB01 (instead of quantifying these parameters from the activity of one representative SMDD and one SMDV). We found that, in *unc-7 unc-9* mutants, peak frequency in forward command periods was decreased in SMDD (though only significantly in SMDDL), and not affected in SMDV, possibly because SMDV peak frequencies in forward command

states are very low to begin with (Fig. 4.22a). These results suggest that, in forward command states, SMD activity requires excitatory inputs facilitated by *unc-7 unc-9* innexins, perhaps from VB01, and that electrical left/right pair connections are required for normal SMD function.

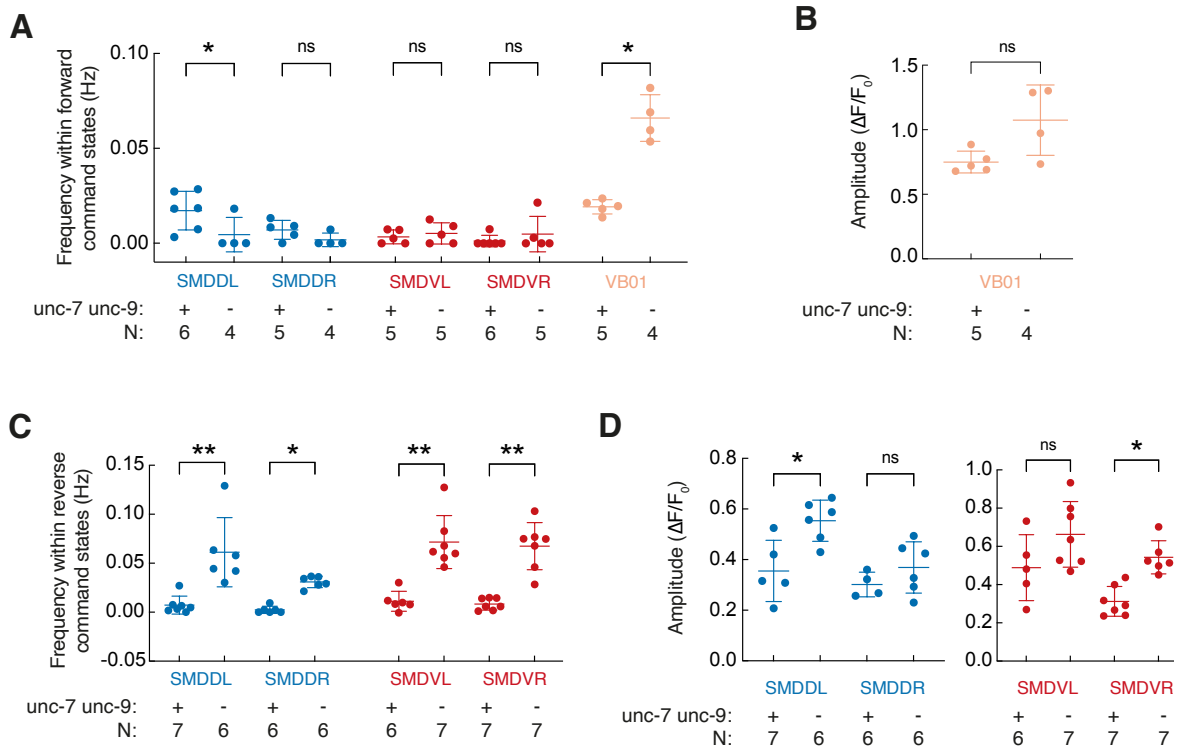


Figure 4.22. *unc-7 unc-9* gap junction disruptions affects SMD and VB01 activities (A-B) Mean (A) frequency and (B) amplitude of GCaMP activity peaks of the denoted neurons in forward command states across whole-brain recordings of control and *unc-7 unc-9* innexin mutants. * $p < 0.05$, ** $p < 0.01$, *** $p < 0.001$, **** $p < 0.0001$, ns not significant; Kruskal-Wallis Test (SMD) and Mann-Whitney Test (VB01). (C-D) Mean (C) frequency and (D) amplitude of GCaMP activity peaks of the denoted neurons in reversal command states across whole-brain recordings of control and *unc-7 unc-9* innexin mutants. * $p < 0.05$, ** $p < 0.01$, *** $p < 0.001$, **** $p < 0.0001$, ns not significant; Kruskal-Wallis Test. (A-D) Each data point is from one animal. All data were obtained from $N=7$ control and $N=7$ *unc-7, unc-9* recordings. Because neurons sometimes showed no activity in forward/reversal command periods, the N numbers in the figure reflect the number of neurons whose activities were used for each quantification. - denotes lack of mutation; + denotes presence of mutation. * $p < 0.05$, ** $p < 0.01$, *** $p < 0.001$, **** $p < 0.0001$; ns, not significant.

We quantified the effect of *unc-7 unc-9* mutation on VB01 activity in forward command states and found a clear increase in VB01 frequency in *unc-7 unc-9* mutants (Fig. 4.22a), while VB01 mean peak amplitude showed a moderate, but not statistically significant increase (Fig. 4.22b). These results suggest that VB01 activity is negatively modulated by gap junction inputs. Regarding SMD activity in reversal command periods, we found a clear increase in peak frequency of all four SMDs (Fig. 4.22c) and significant increases in SMDDL and SMDVR peak amplitudes (Fig. 4.22d) in *unc-7 unc-9* mutants. These findings suggest that SMD activity is negatively modulated through gap junctions in the reversal command state.

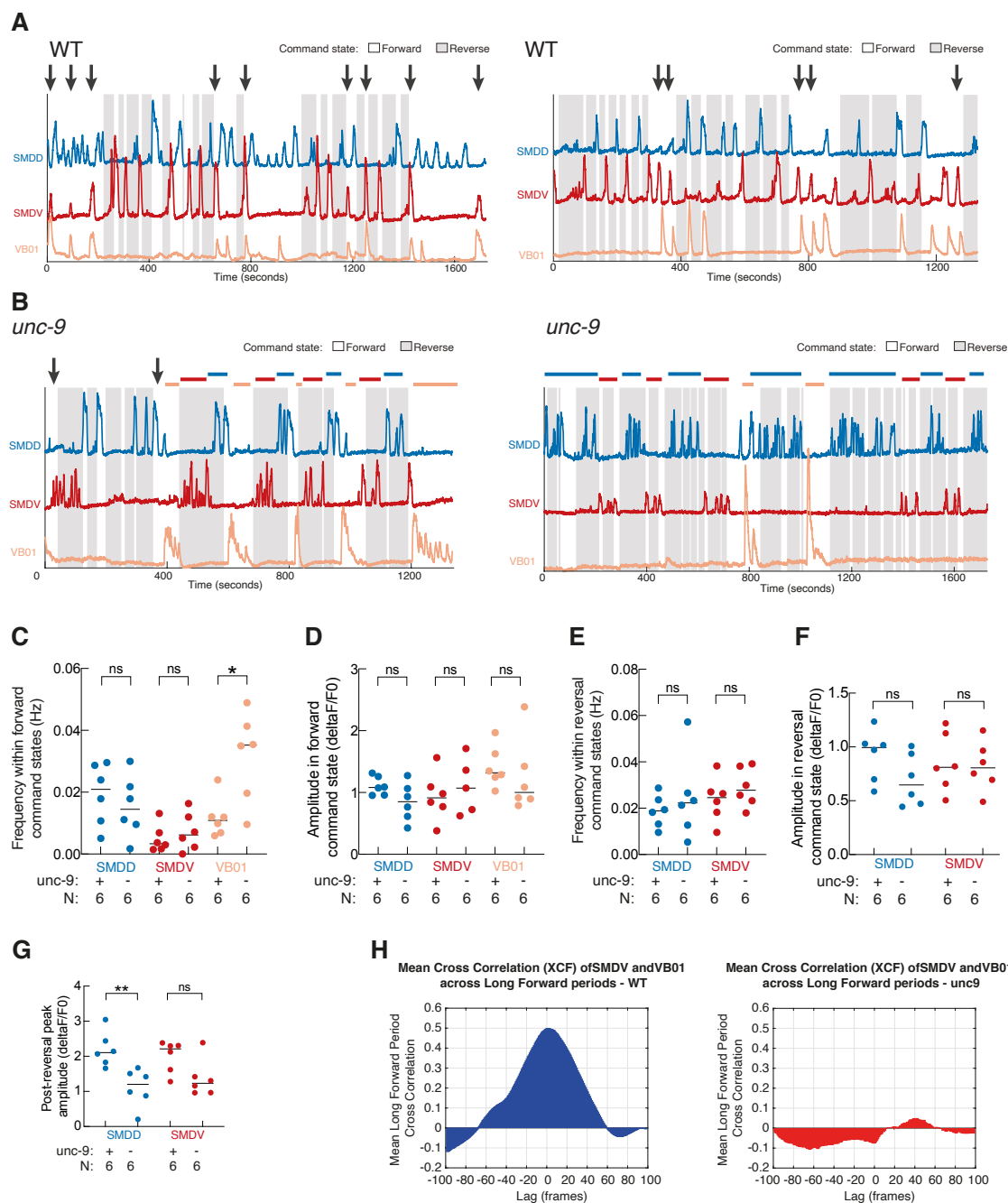


Figure 4.23. *unc-9* gap junction disruptions affects SMD and VB01 activities differentially in forward or reversal command states. (A-B) Example GCaMP activity traces of SMD and VB01 neurons in immobilized (A) control and (B) *unc-7 unc-9* mutant animals. Command states were determined using AVA neuronal activity (see Methods). Arrows denote shared SMDV/VB01 activity peaks, horizontal bars above activity traces denote periods of uninterrupted activity from one neuron, without alternation with other neurons; colors correspond to the colors of the activity traces of the corresponding neuron. (C-D) Mean (C) frequency and (D) amplitude of GCaMP activity peaks of SMD and VB01 neurons in forward command states across whole-brain recordings of control and *unc-9* innexin mutants. (E-F) Mean (E) frequency and (F) amplitude of SMD GCaMP activity peaks in reversal command states across whole-brain recordings of control and *unc-9* innexin mutants. (G) Mean amplitude of post-reversal SMD GCaMP activity peaks across whole-brain recordings of control and *unc-9* innexin mutants. (C-G) Each data point is from one animal. - denotes lack of mutation; + denotes presence of mutation. * $p < 0.05$, ** $p < 0.01$, *** $p < 0.001$, **** $p < 0.0001$; ns, not significant; Mann-Whitney Test. (H) Mean cross correlation across forward command periods of SMDV and VB01 across control (left) and *unc-9* (right) animals in immobilized, whole-brain imaging recordings. P values were calculated using the `kstest2` MATLAB function (Mathworks); * $p < 0.05$, ** $p < 0.01$, *** $p < 0.001$, **** $p < 0.0001$; ns, not significant. The SMDV x VB01 cross correlations in *unc-7 unc-9* mutants were significantly different than WT ($p = 9.4333 \times 10^{-30}$).

To summarize, these data suggest that VB01 activity is independent from SMD, while SMD activity may require gap junction inputs from VB01 (or other neurons) during forward command states (Fig. 4.21a). Further, we calculated the mean cross correlation between VB01 and SMDV activity traces in all forward command periods, and observed that the correlation between VB01 and SMDV during forward command periods is lost in *unc-7 unc-9* mutants (Fig. 4.21b). We performed a Kolmogorov Smirnov test comparing the distribution of mean cross correlation per forward command periods for all periods for wildtype vs *unc-7 unc-9* mutants, using the *kstest2* function in MATLAB (Mathworks), and found the following p-values: SMDVL x VB01 $p=4.0627 \times 10^{-5}$, SMDVR x VB01 $p=2.0848 \times 10^{-46}$. Thus, we suggest that *unc-7* and/or *unc-9* innexins underlie the correlation between VB01 and SMDV activity peaks. Lastly, we calculated the average peak frequency and amplitude of SMD and VB01; the data suggests that gap junctions play a role in negatively modulating VB01 activity in forward command states (Fig. 4.22a), and SMD activity in reversal command states (Fig. 4.22c,d).

The observations made from *unc-7 unc-9* mutant imaging motivated us to dissect the role of innexins in SMD/VB01 activity further. Forward command output neuron AVB is electrically connected to B-MNs through heterotypic UNC-7S/UNC-9 gap junctions, with UNC-7S expressed in AVB and UNC-9 in B-MNs (T. Starich et al. 2009). Although both SMD and the ventral B-MNs express both UNC-7 and UNC-9, we wondered whether imaging the neuronal activity of single mutants would help us further dissect the role of individual innexins in this circuit. Thus, we recorded Ca^{2+} activity in *unc-9* single mutants and assessed the effect of a lack of *unc-9* in SMDD, SMDV and VB01 activity. We observed that both SMDs were occasionally active during forward command states, albeit rarely (Figs. 4.23a-b, see arrows for SMD activity in forward command states). This observation is in contrast with the observation that SMD activity is diminished in *unc-7 unc-9*; we hypothesize that gap junction input via *unc-7* is crucial for SMD activity during forward command states. Qualitative inspection of SMD activity also revealed that throughout the recordings, SMDD and SMDV are active mostly in bouts; SMDD-SMDV activity peaks rarely alternate, as would be observed in wildtype animals (compare alternating activity peaks from SMDD and SMDV in Fig. 4.23a vs Fig. 4.23b). Further, VB01 activity appeared to be increased and often the only neuron of the three active throughout entire forward command periods (Fig. 4.23b), which is reminiscent of VB01 activity in *unc-7 unc-9* mutants (Fig. 4.21a). We quantified SMDD, SMDV and VB01 activity and found that, in forward command states, VB01 peak frequencies were increased in *unc-9* mutants, while SMDD and SMDV activities were not altered (Fig. 4.23c). This is in contrast to *unc-7 unc-9* mutants, where SMDD and SMDV activity in forward command states was abolished (Fig. 4.21, Fig. 4.22). Thus, the data suggest that SMD activity, especially SMDD, requires gap junction input in forward command states via *unc-7*. SMDD SMDD, SMDV and VB01 peak amplitudes remained unaltered (Fig. 4.23d). Interestingly, we observed no effects on SMD activity during reverse command states (Fig. 4.23e-f), in contrast to the increase in

SMD peak frequencies and amplitudes during reverse command states in *unc-7 unc-9* mutants (Fig. 4.22c-d). Thus, we hypothesize that inhibitory input via *unc-7* plays a role in modulating SMD activity in reverse command states. We also quantified the average post-reversal peak amplitudes of SMDD and SMDV and found that SMDD post-reversal peaks are significantly weaker in *unc-9* mutants, while SMDV peaks are not, despite an observable trend (Fig. 4.23g).

VB01 and SMDV activity are tightly linked: their activities in unperturbed worms are highly correlated (Fig. 4.8, black arrows in Fig. 4.23a) and inhibiting SMD abolishes VB01 activity (Fig. 4.13b). In *unc-7 unc-9* mutants, VB01 is decoupled from SMDV, as SMDV is not active during forward command states while VB01 vigorously is, and their correlation is lost (Fig. 4.21, Fig. 4.22a). We investigated the effect of *unc-9* mutation on SMDV-VB01 coupling by calculating the cross correlation between VB01 and SMDV activity traces across forward command periods in unperturbed animals and in *unc-9* mutants. We observed a significant loss of correlation between VB01 and SMDV in *unc-9* mutants (Fig. 4.23h). We performed a Kolmogorov Smirnov test comparing the distribution of mean cross correlation per forward command periods for all periods for wildtype vs *unc-9* mutants, using the `kstest2` function in MATLAB (Mathworks), and found the following p-values: SMDV x VB01 $p = 9.433 \times 10^{-30}$. Thus, the coupling of SMDV and VB01 activities is dependent on *unc-9*. Lastly, it is likely that VB01 activity through gap junctions is instructive to SMDV activity, given that innexin mutants show VB01 activity and no SMDV activity during forward command states specifically. We hypothesize that VB01 is an oscillator independent from SMDV, and perhaps driving SMDV oscillations.

4.5. Level I and II Interactions: Do lower hierarchical levels influence the global forward-reverse-turn cycle?

SMD, a multifunctional neuron class

As mentioned in section 3.2, the SMDs showed altered activity in reversal command periods in immobilized and freely behaving animals (Fig. 4.17b,c), and inhibiting the SMDs led to reduced head bend amplitudes during forward, but not reverse locomotion (Fig. 4.16). We wondered: If SMD activity does not serve head-bending during backward locomotion, what role do the SMDs play in this state? Previous work has shown that reversal ends are typically followed by reorientation turns (also termed post-reversal turns), upon which worms transition into forward locomotion (Gray, Hill, and Bargmann 2005; Donnelly et al. 2013). We calculated averages of SMDD/V activity triggered to reversal ends and reliably observed mutually-exclusive SMDD or SMDV activity peaks coinciding with post-reversal dorsal or ventral turns, respectively (Fig. 4.24a). In fact, we observed that SMD activity correlated with the amplitude of reorientation turns, shown by the correlation between post-reversal head bend angle and the amplitude of the co-occurring SMD Ca^{2+} activity peak (Fig. 4.24b). This suggested a distinct

role in reverse-to-forward transitions: SMD activity in reversals serves post-reversal turn amplitude and could promote reverse-to-forward transitions.

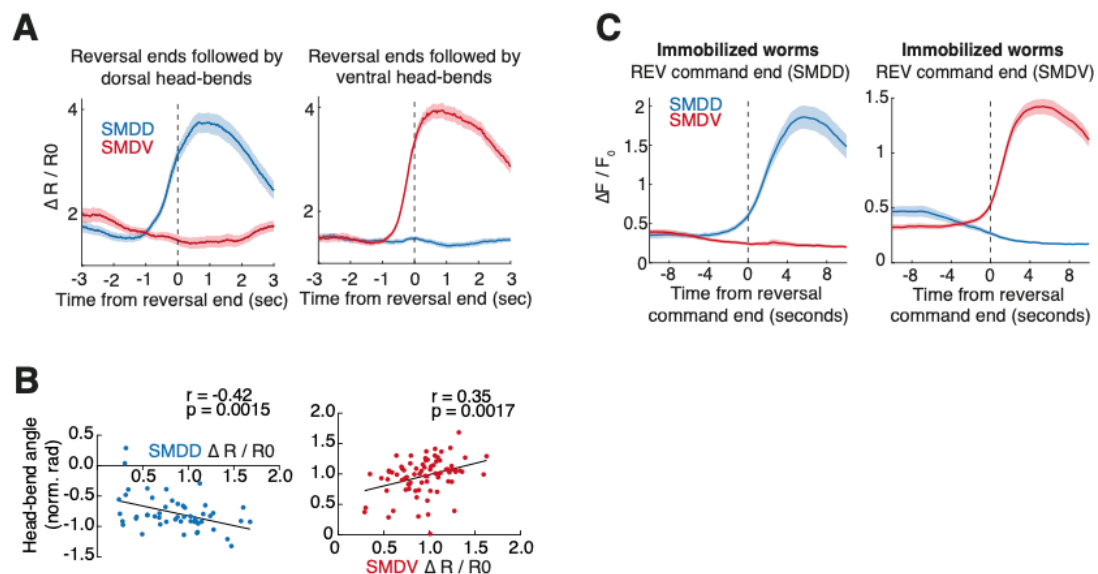


Figure 4.24. SMD activity is tightly linked to reversal ends in freely-behaving and immobilized animals. (from Kaplan et al, 2020) **(A)** Trigger-averaged GCaMP/mCherry traces \pm SEM from SMD recordings in freely moving animals aligned to reverse-to-turn transitions, separated by post-reversal dorsal (left) or ventral (right) head-bend. $n = 55$ dorsal and 96 ventral events, pooled from 11 animals. **(B)** Peak head-bend angle (angle #2, normalized to 95th percentile within each recording) and GCaMP/mCherry signal amplitude for SMDD and post-reversal dorsal head-bends (left) or SMDV and post-reversal ventral head-bends (right). Pearson correlation coefficient and p-value indicated, n as in **(A)**. **(C)** Trigger-averaged SMD GCaMP traces \pm SEM from immobilized worm recordings aligned to reverse-to-forward command state transitions, separated by SMDD (left) and SMDV (right) transition peaks. $n = 64$ (SMDD) and 158 (SMDV) pooled across 10 animals.

The SMDs are head motor neurons and are also proprioceptive, so the correlation between their activity increases and post-reversal turns may be expected, given that these involve head movement (Yeon et al. 2018). Thus, we explored whether the SMDs played a role in the control of reverse-to-forward transitions beyond the execution of the post-reversal turn movement. In other words, we hypothesized that SMD activity could play a role in the generation of the post-reversal turn command itself and thus influence behavioral state transitions, i.e. the reverse-to-forward transition. In that case, SMD activity would be linked to reversal command ends also in the absence of movement. Indeed, averages of SMD activity triggered to reversal command state initiation in immobilized worms also showed SMDD/V peaks coinciding with reversal command ends, and, as in freely behaving worms, these peaks were mutually exclusive (Fig. 4.24c).

We hypothesized that SMD activity plays an active role in promoting reversal termination. Alternatively, SMD activity could simply coincide with reverse-to-forward transitions if, biomechanically, the transition from backward to forward locomotion required specific postures. Thus, we tested whether the lack of SMD activity would affect reverse-to-forward transition probability. We quantified the reversal durations in SMD-inhibited worms and found that worms where SMD activity was inhibited did transition from reverse to forward locomotion, but reversal durations were much

longer than in control worms (Fig. 4.25a). Crucially, we performed the same analysis on whole-brain Ca^{2+} imaging recordings from immobilized, SMD-inhibited animals to disentangle neuronal activity from movement execution. We observed a similar effect of SMD inhibition: the duration of reversal command states was increased in SMD::hisCl worms (Fig. 4.25b) and the distribution of reversal command state durations was skewed towards much longer reversal states (Fig. 4.25c). These results confirmed that SMD activity plays a role in reverse-to-forward transitions beyond movement execution, namely promoting reversal command termination.

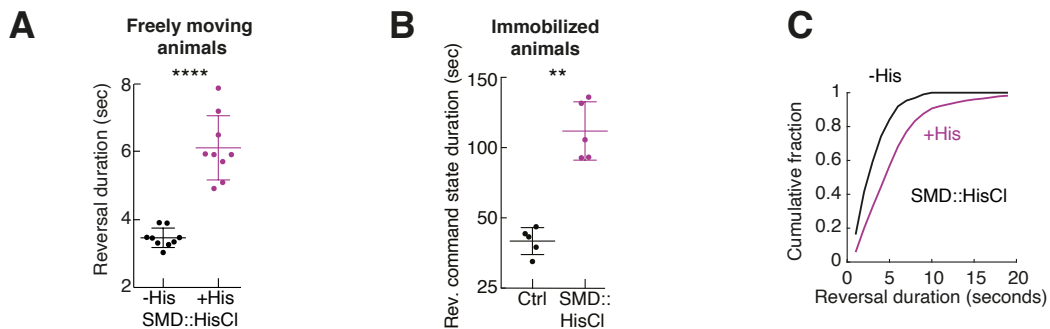


Figure 4.25. SMD activity promotes reversal termination (from Kaplan et al, 2020) **(A)** Reversal duration in SMD::hisCl animals. **** $p < 0.0001$, Mann-Whitney Test. Each data point is the mean of an experimental repeat ($n=9$) with ~ 20 animals each. **(B)** Reversal command duration from head ganglia imaging in immobilized animals. Each data point is the mean of an experimental repeat, $n=5$ each. ** $p < 0.01$, Mann-Whitney test. **(C)** Cumulative distribution of reversal duration in SMD::hisCl animals \pm histamine. $n = 1416$ (control) and 1814 (histamine) reversals. $p < 0.0001$, two-sample Kolmogorov-Smirnov test. Note that SMD inhibition led to reversal lengths beyond 10s that were never observed in non-inhibited controls. Data pooled from $n = 9$ experimental repeats from each condition, with ~ 20 animals each repetition.

The influence of SMD on reverse-to-forward transitions raised the question of whether the activity of lower level oscillators is required for the global neuronal dynamics that represent the uppermost FWD-REV cycle. To understand this, we performed Principal Component Analysis on SMD::hisCl/ $\text{VNC}_{\text{ACH}}::\text{hisCl}$ whole-brain, immobilized recordings and saw that whole-brain activity still represents the behavioral FWD-REV cycle (Fig. 4.26). Thus, inhibiting the lower-level oscillators does not affect the gross neuronal dynamics, but SMD inhibition does affect the frequency of behavioral state transitions.

To summarize, SMD activity promotes reversal command termination in moving and immobilized worms. Thus, the SMDs are multifunctional: they drive head-casting during forward locomotion while promoting reversal command termination during backward locomotion. These hierarchical relationships arise from intrinsic circuit properties and not proprioception. In conclusion, SMD and DB activities are nested within the overarching forward/reverse command cycle through circuit interactions.

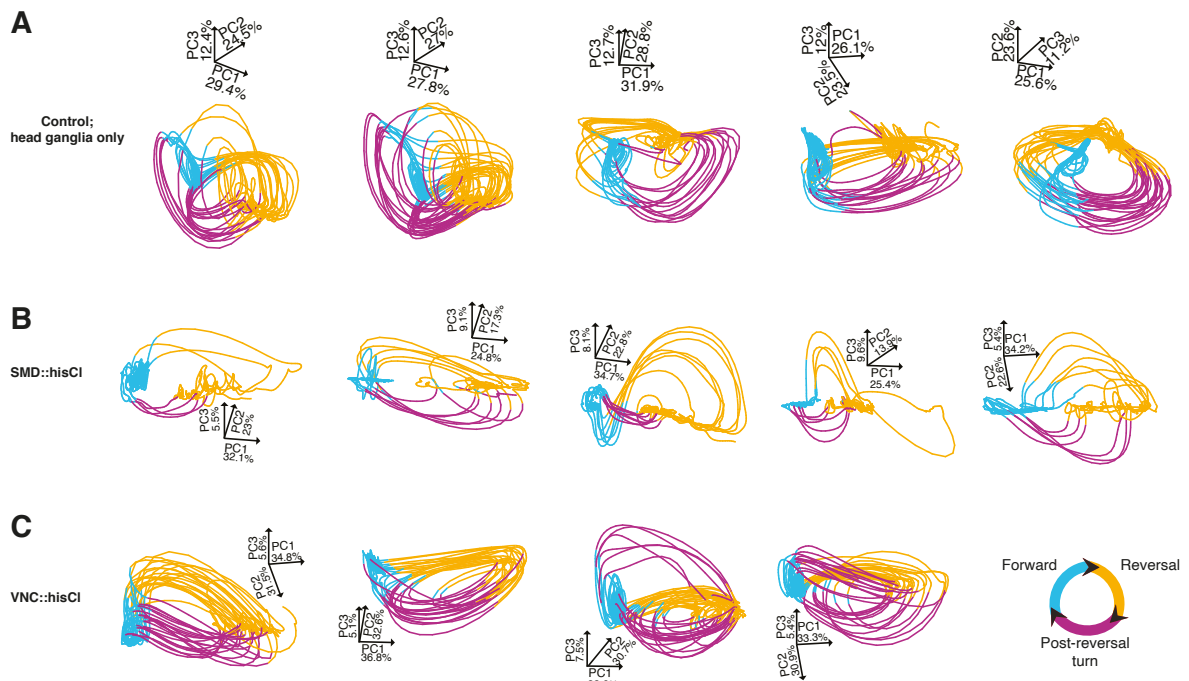


Figure 4.26. Inhibiting the lower-level oscillators does not affect forward/reverse cycle. (A-C) Low-dimensional representation of neuronal activity cycle, from principal components analysis (PCA) performed on neuronal traces from head ganglia neurons in control (A), SMD inhibition (B – SMD::hisCl), and motor neuron inhibition (C – VNC_{ACh}::hisCl). Color key in the rightmost panel in (C) indicates motor command state inferred from neuronal activity (Methods; arrowheads indicate directional flow). Coordinates depict PC axes orientations and % variance explained.

4.6. Investigating network mechanisms of SMD modulation

As presented previously, circuit mechanisms toggle the DB motor neurons between active/inactive states (Fig. 4.5); and their activity serves propagated bend generation during forward locomotion (Fig. 4.14b), while they seem to not serve a role in backward locomotion. In contrast, the SMDs are not toggled between active and inactive states, but rather between functional roles. In this section, we will explore the efforts we made to understand how SMD multifunctionality is achieved, i.e. how they are modulated in forward or reverse command states to drive head-casts or post-reversal turn commands, respectively.

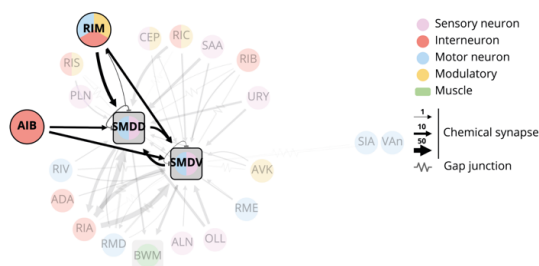


Figure 4.27. SMDs are pre-synaptic to reverse-active neurons AIB and RIM. (from nemanode.org) Schematic of synaptic connections between SMD and other neurons. Thresholds for graphing connections were set, such that only connections with at least two detected chemical synapses or one gap junction are displayed (White 1986, Witvliet 2021). L/R pairs have been pooled.

4.6.1. Investigating network mechanisms of SMD modulation in REV command state

First, we sought to understand which neurons' activities are important for the switch in SMD activity pattern in reversal command states. We considered which presynaptic partners of SMD are known to play a role in backward locomotion (Fig. 4.27). We focused on the AIB and RIM neurons and hypothesized that their activity could inhibit the SMDs during reversals (Piggott et al. 2011; Luo et al. 2014; Laurent et al. 2015; Kato et al. 2015; Gordus et al. 2015).

To test whether the AIB interneuron modulates SMD activity during reversals, we inhibited AIB through cell-specific expression of *hisCl* and acute histamine exposure and hypothesized that inhibiting AIB would abolish the decrease of SMD peak frequencies and amplitudes in reversals (Fig. 4.28a). Indeed, we observed that AIB inhibition abolished the modulation of SMDD amplitude and of both SMDs' frequencies in reverse locomotion, since histamine exposure in AIB::*hisCl* animals suppressed the amplitude and frequency differences between forward and reverse (Fig. 4.28b). These results implicate AIB in negatively regulating SMD activity and suggest that they are crucial for the switch of SMDs between high and lower activity states.

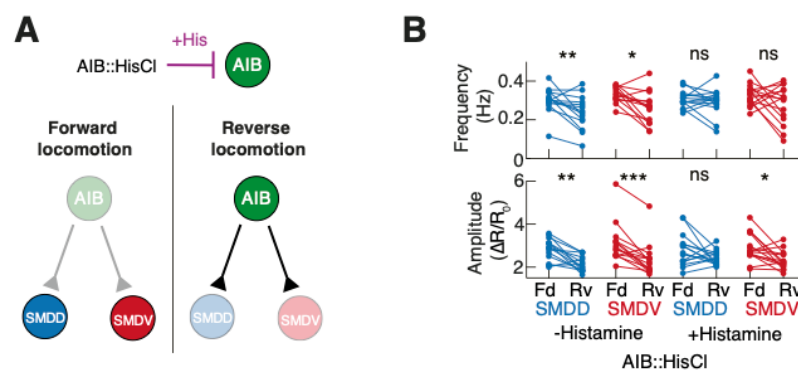


Figure 4.28. AIB interneurons orchestrate upper-hierarchy SMD switch. (from Kaplan et al, 2020) (A) Experiment design and hypothesis. (B) Frequency (upper) and average amplitude (lower; R = GCaMP/mCherry ratio) of activity peaks in AIB::*hisCl* animals \pm histamine. ns, not significant; * $p < 0.05$, ** $p < 0.01$, *** $p \leq 0.001$, Wilcoxon matched-pairs signed rank test. Each data point from one animal, $n = 14$ (-histamine) and $n = 15$ (+histamine).

Next, we explored the role of reversal-active motor neuron RIM. RIM is active during backward locomotion, innervates head muscles and SMD, and is postsynaptic to AIB (J. G. White et al. 1986; Piggott et al. 2011; Luo et al. 2014; Laurent et al. 2015; Kato et al. 2015; Gordus et al. 2015). Moreover, previous work from the Alkema and Horvitz labs has shown that RIM modulates backward locomotion and head oscillations during reversals through tyramine signaling (Alkema et al. 2005; Pirri et al. 2009; Donnelly et al. 2013). Since unpublished observations in the Zimmer lab showed that RIM-inhibited animals do not reverse (unpublished observations from Kerem Uzel, PhD), we resorted to studying RIM's role in SMD activity through tyramine synthesis and receptor mutants. We investigated *tdc-1*, a tyrosine decarboxylase required for tyramine biosynthesis; and *lgc-55*, a tyramine receptor expressed in the SMD neurons (Fig. 4.29a) (Pirri et al. 2009). As for AIB-inhibited worms, we quantified the average amplitude and frequency of SMDD and SMDV activity peaks in forward and reverse locomotion. We observed that both *tdc-1* and *lgc-55* mutations affected the forward/reverse

modulation of SMDD frequency only (Fig. 4.29b). Thus, we have found a small, but specific role of RIM on SMDD modulation (through tyramine signaling), and a major role of AIB in SMD modulation during reversals. These neurons' inputs contribute to the switch in SMD activity at the uppermost hierarchical level, and are consistent with our model of an implementation of a behavioral hierarchy through circuit interactions (Fig. 4.29c).

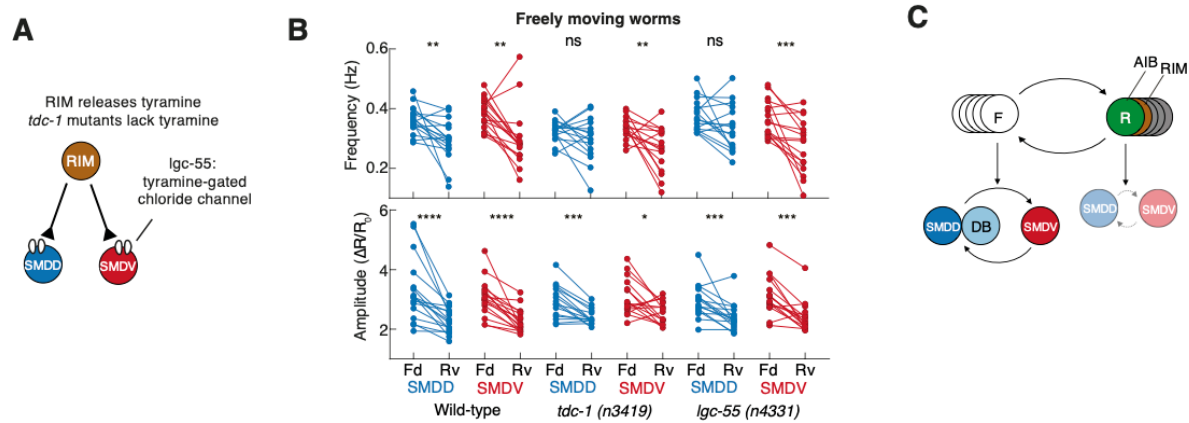


Figure 4.29. Tyramine mutations only partially affect upper-hierarchy SMD activity switch. (from Kaplan et al, 2020) **(A)** Experimental design. The RIM interneuron synapses onto both SMDD and SMDV. Several studies have shown that RIM signals via tyramine to affect head oscillations and reversal behavior (Alkema et al., 2005; Donnelly et al., 2013; Pirri et al., 2009). We therefore tested a deletion mutant of *tdc-1*, a tyrosine decarboxylase required for tyramine biosynthesis. These *tdc-1 (n3419)* mutants are strongly defective in tyramine production (Alkema et al., 2005). We also tested a large deletion allele of *lgc-55* (Donnelly et al., 2013; Ringstad et al., 2009), a tyramine receptor that is expressed in the SMD neurons (Pirri et al., 2009). Both mutant strains were defective in the forward/reverse state modulation of SMDD frequency, but no other parameters. **(B)** Frequency (upper) and average amplitude (lower) of activity peaks in *tdc-1 (n3419)* (n=16), *lgc-55 (n4331)* (n=16), and parallel wild-type controls (n=17). ns, not significant; *p<0.05, **p<0.01, ***p<0.001, ****p<0.0001, Wilcoxon matched-pairs signed rank test. Each data point is from one animal. **(C)** Summary of investigated neuronal relationships.

4.6.2 Mechanisms of SMD modulation in turn command state

A prominent feature of SMD activity is their antagonism: SMDD and SMDV are continuously active, yet their activity peaks are mutually exclusive (Fig. 4.6a, Fig. 4.8). This feature is perhaps most apparent at reversal command ends, which are invariably accompanied by either an SMDD or an SMDV peak (Fig. 4.24). These observations led us to wonder whether SMDD and SMDV mutually inhibit each other. We hypothesized that this antagonism could be crucial for the unambiguous performance of dorsal or ventral turns and thus for food search behavior. The SMDD/SMDV antagonism could arise from cholinergic signaling, as the SMD class is cholinergic, SMDD and SMDV are reciprocally connected through chemical synapses, and the *C. elegans* genome contains not only excitatory acetylcholine-gated channels, but also inhibitory ones (J. G. White et al. 1986; Putrenko, Zakikhani, and Dent 2005; Pereira et al. 2015). In fact, it has been shown that SMDs express several acetylcholine-gated chloride (ACh-gated Cl⁻) channels through which they could inhibit each other: *acc-1*, *acc-4*, *lgc-46* and *lgc-47* (Pereira et al. 2015; Taylor et al. 2021). Among these, *acc-1* and *lgc-47* were enriched in SMD (Taylor et al. 2021). To understand the role of cholinergic signaling and inhibition in SMD activity, we recorded the whole-brain neuronal activity of immobilized, *acc-1* mutant worms. These

recordings revealed that, in wildtype animals, SMDD and SMDV activities are mutually exclusive (Fig. 4.30a), whereas in *acc-1* mutants, SMDD and SMDV showed coincident activity peaks (Fig. 4.30b).

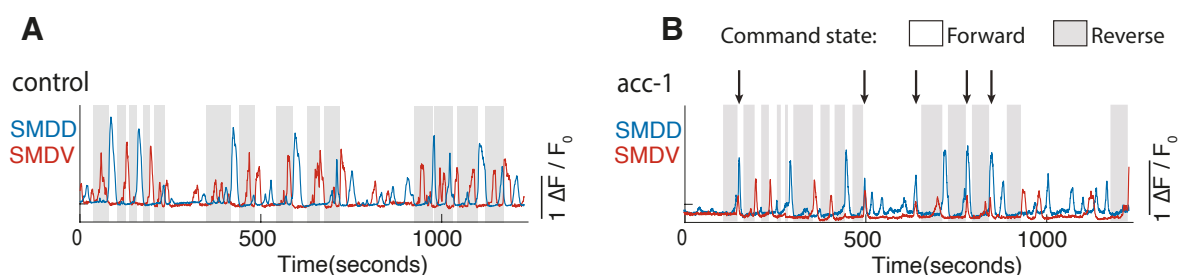


Figure 4.30. *acc-1* ACh-gated chloride channel mutation affects SMD antagonism, but not SMD activity. (A-B) Example GcAMP activity traces of SMDD and SMDV neurons in an immobilized, (A) control animal and (B) an *acc-1* ACh-gated chloride channel mutant animal. Command states were determined using AVA neuronal activity (see Methods).

We quantified the mean fraction of co-occurring peaks in control and *acc-1* recordings across all four SMD neurons (SMDDL, SMDDR, SMDVL, SMDVR) and found a small decrease in the fraction of co-occurring activity peaks within left/right pairs (comparing SMDDL with SMDDR, and SMDVL with SMDVR) (Fig. 4.31a). More importantly, we observed an increase in the fraction of co-

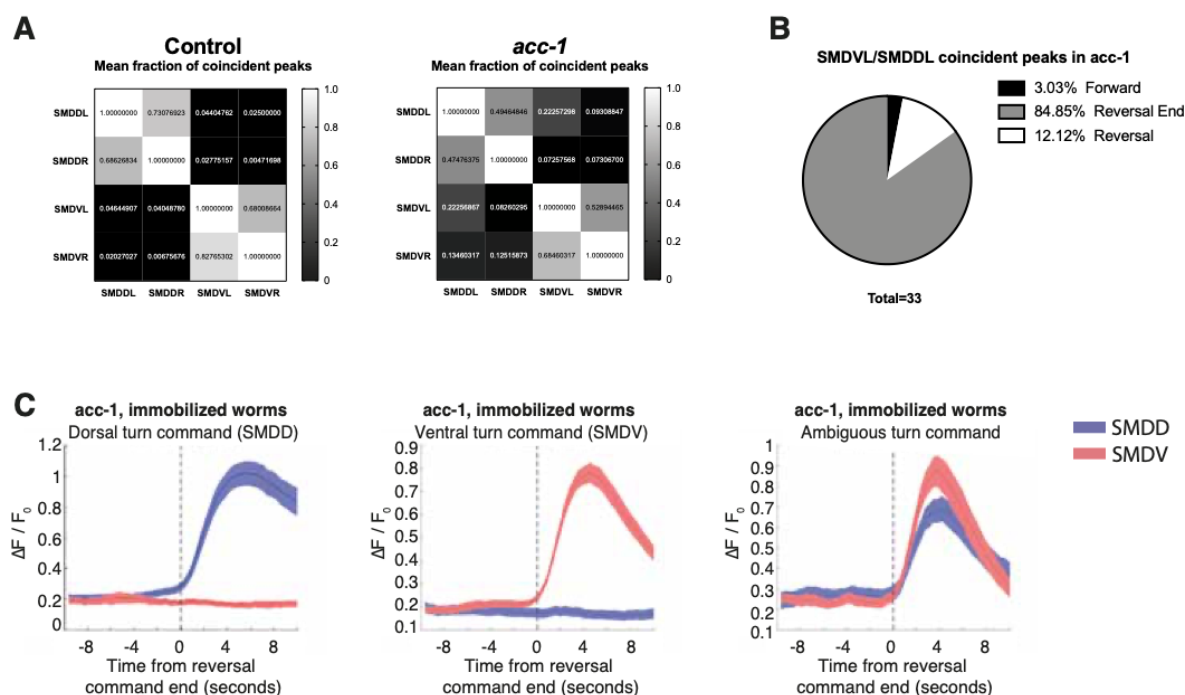


Figure 4.31. ACh-gated chloride channels ensure mutual exclusiveness at reversal end- turn transition. (A) Mean fraction of coincident activity peaks among all four SMD neurons in control (left) and *acc-1* animals. $n=5$ *acc-1* recordings; $n=4$ control recordings. (B) Fraction of coincident peaks between SMDVL and SMDDL sorted by behavior command state, in *acc-1* mutant animals ($n=33$ coincident peaks pooled across $N=5$ recordings). (C) Averages of SMD activity triggered to (left panel) dorsal-, (middle panel) ventral-, or (right panel) ambiguous turn commands (see Methods). Timepoint 0 denotes the onset of reversal command end (AVA fall, see Methods). $N=5$ recordings for all panels; $n=26$ dorsal turn commands (left), $n=55$ ventral turn commands (middle), $n=29$ ambiguous turn commands (right).

occurring activity peaks of neurons across pairs (comparing SMDDs with SMDVs, termed coincident peaks for simplicity) (Fig. 4.31a). While in control recordings, coincident peaks with the opposing SMD occur in a maximum of 4.64% of cases, they amount to 22.26% in *acc-1* mutants (Fig. 4.31a). It is worth noting that we believe that the coincident peaks detected in control recordings are a product of our peak detection method, which sometimes detects very low amplitude signals as peaks. Next, we wondered whether these coincident peaks disproportionately occur at specific behavioral command states and found that the vast majority of them occur at reversal end (Fig. 4.31b). Reversal-end-triggered averages of SMD activity, where we manually categorized reversal ends as dorsal (SMDD peak with no SMDV peak), ventral (SMDV peak with no SMDD peak) or ambiguous (coincident SMDD and SMDV peaks) turn commands, further visualize the ambiguous turn command phenotype of *acc-1* mutants (see Methods, Fig. 4.31c).

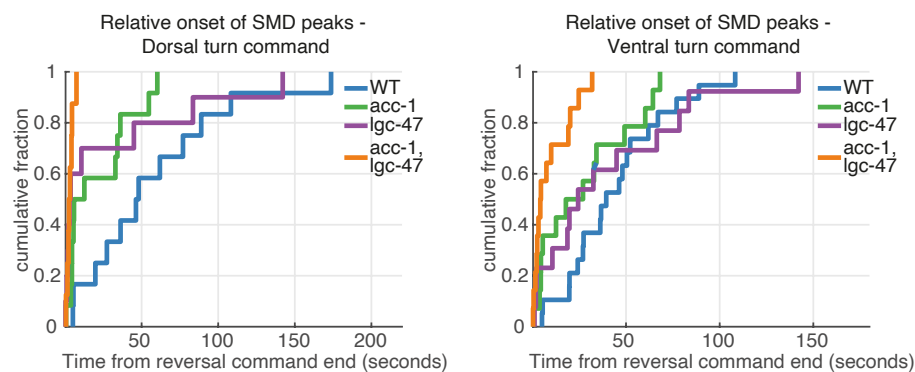


Figure 4.32. ACh-gate chloride channel mutations decrease the distance between SMDD and SMDV activity peaks at turn command onsets. Cumulative distributions of the relative onsets of SMD peaks upon dorsal (left) and ventral (right) turn commands. The onset of the first SMDV peak upon reversal command end was subtracted from the onset of the first SMDD peak upon reversal command end to obtain the relative onset for dorsal turn commands (left) and vice versa for ventral turn commands (right) (see Methods). Control: N=8; *acc-1*: N=5; *lgc-47*: N=6; *acc-1*, *lgc-47*: N=6 recordings.

Next, seeing that the *lgc-47* channel is also enriched in SMD, we performed a more comprehensive analysis of ACh-gated Cl⁻ channels, including not only *acc-1* single mutants, but also *lgc-47* single mutants and *acc-1 lgc-47* double mutants (Taylor et al. 2021). To assess whether ACh-gated Cl⁻ channels affect the SMD antagonism at reversal end, we calculated onset differences between SMDD and SMDV peaks at reversal end. To this end, we automatically categorized reversal ends according to which SMD (D or V) peaked first upon reversal command end and then calculated the onset difference between this peak and the first peak of the opposing SMD, i.e. in a dorsal turn command, where SMDD peaks first, we calculated the difference between this SMDD peak onset and the next first SMDV peak onset (see Methods). We found that, especially for dorsal turn commands, the time difference between alternating SMD peaks upon reversal end was markedly decreased. This phenotype is most apparent in *acc-1 lgc-47* double mutants, where all SMDV peaks following the post-reversal SMDD peak occur within 10 seconds from reversal end, as opposed to wildtype, where less than 20% of SMDV peaks occur within 10 seconds from reversal end (Fig. 4.32).

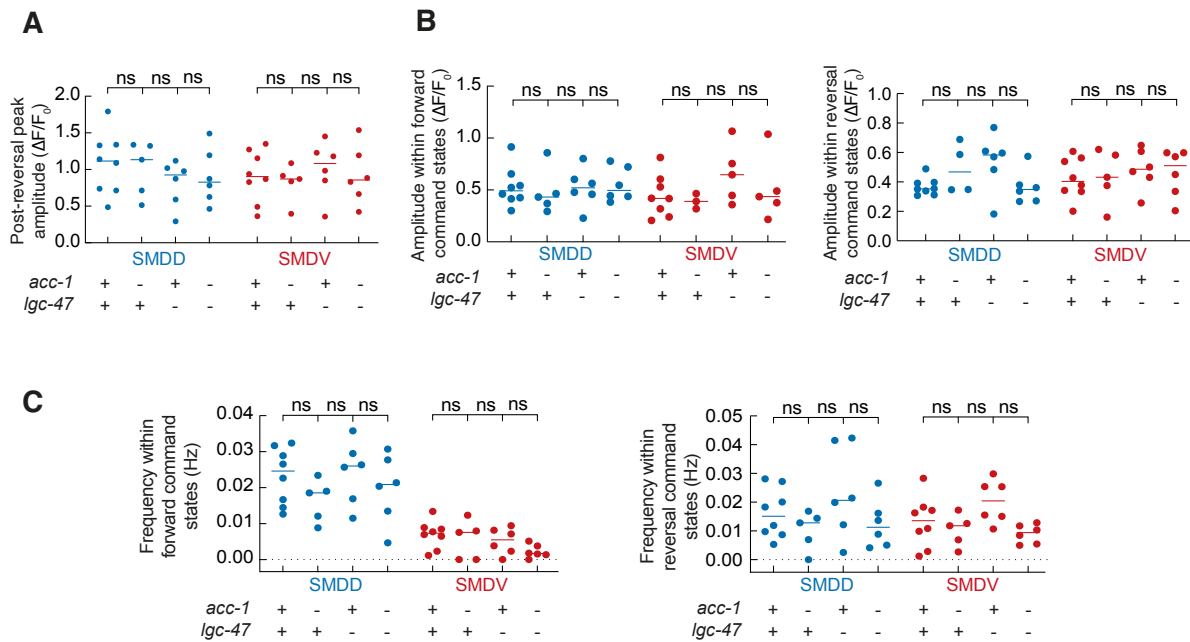


Figure 4.33. ACh-gated chloride channels do not modulate SMD peak frequency or amplitude. (A) Mean amplitude of post-reversal-command SMDD and SMDV GCaMP activity peaks across whole-brain recordings. Analysis of variance (ANOVA). ns, not significant. (B) Mean amplitude of SMDD and SMDV GCaMP activity peaks in forward (left) and reversal (right) command states across whole-brain recordings. Kruskal-Wallis test. ns, not significant. (C) Mean frequency of SMDD and SMDV GCaMP activity peaks in forward (left) and reversal (right) command states across whole-brain recordings. Kruskal-Wallis test. ns, not significant. (A-C) Control: N=8; *acc-1*: N=5; *lgc-47*: N=6; *acc-1, lgc-47*: N=6 recordings. - denotes lack of mutation; + denotes mutation. Each data point is from one animal.

Interestingly, these mutations have no effect on the amplitude of post-rev peaks (Fig. 4.33a), neither on SMD peak frequency or amplitude in either command state (Fig. 4.33b,c). Thus, the data suggests that ACh-gated chloride channels do not play a role in modulating SMD peak frequency or amplitude, but rather on establishing the dominance of either SMD at reversal end and presumably the mutual exclusiveness of dorsal or ventral turn execution. Lastly, we observed an effect of ACh-gated Cl⁻ channels on command state durations: both forward and reverse command states were consistently shorter in these mutants (Fig. 4.34), hinting at a role of inhibitory cholinergic signaling in sustaining command states.

In section 4.6.1, we saw that SMD activity is negatively modulated during the reversal command state (Fig. 4.28, Fig. 4.29). We wondered how the strong, reversal-end SMD peak is reliably generated despite SMD modulation during reversal command states. We identified two, non-mutually-exclusive possibilities: SMD activity could rebound from inhibition at the end of the reversal command state, when the activity of reversal neurons such as AIB and RIM decreases; alternatively/additionally, SMD could receive excitatory inputs at the reverse-to-forward transition from forward-active neurons. We explored the latter possibility and identified forward command interneuron RIB as a potential candidate for excitatory input to SMD. RIB activity is tightly linked to forward locomotion (Gray 2005) and forward locomotion speed, and it has gap junction connections to and is presynaptic to SMD (Fig.

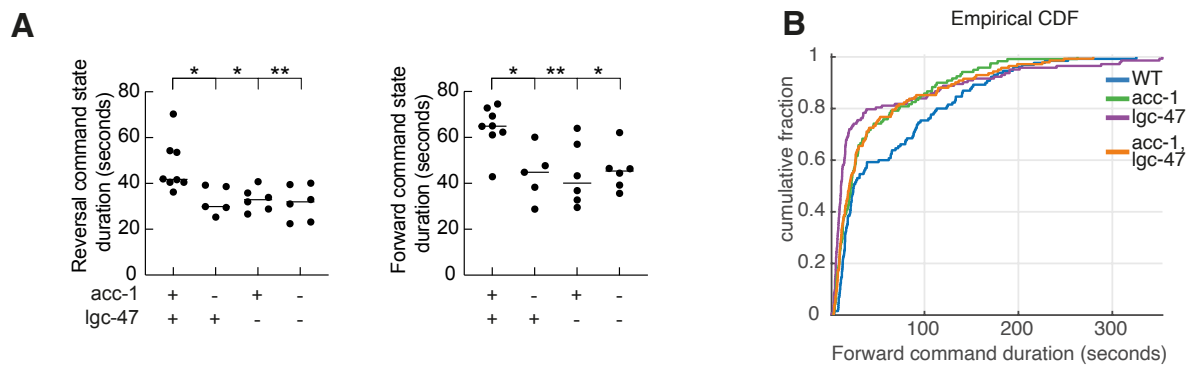


Figure 4.34. ACh-gated chloride channel mutations affect command state durations. (A) Mean reversal (left) and forward (right) command state durations across whole-brain recordings. Each data point is from one animal. - denotes lack of mutation; + denotes mutation. Control: N=8; *acc-1*: N=5; *lgc-47*: N=6; *acc-1, lgc-47*: N=6 recordings. ns, not significant; * $p < 0.05$, ** $p < 0.01$, *** $p < 0.001$, **** $p < 0.0001$, analysis of variance (ANOVA). (B) Cumulative distribution of forward command state durations. Control: N=8; *acc-1*: N=5; *lgc-47*: N=6; *acc-1, lgc-47*: N=6 recordings.

35a) (J. G. White et al. 1986; Z. Li et al. 2014; Kato et al. 2015). We inhibited RIB cell-specifically using the hisCl system and imaged the whole-brain neuronal activity of these animals. We found that RIB inhibition led to decreased amplitudes of post-reversal SMD peaks (Fig. 4.35b), which suggests that RIB activity plays a role in potentiating post-reversal SMD activity. Moreover, we observed an altered proportion of dorsal/ventral turn commands in RIB-inhibited worms, as RIB::*hisCl* leads to an increase in reversal command ends associated with an SMDD activity peak (Fig. 4.35c). Our results show that RIB activity positively modulates SMD activity at the reverse-to-forward transition and that its activity is especially important for establishing the dominance of SMDV over SMDD activity peaks at reversal end. Paradoxically, inhibiting RIB, which is a forward-active neuron, led to an increase in forward command durations and shorter REV command states (Fig. 4.35d-e).

4.6.3. Investigating network mechanisms of SMD modulation in FWD command state

Lastly, we investigated the modulation of SMD activity in forward command states. Our *unc-7 unc-9* mutant recordings suggested that SMD activity requires input via gap junctions during forward command states, since immobilized *unc-7 unc-9* mutants showed silent SMDs specifically during forward states (Fig. 4.21a). Given that RIB and SMD are connected through gap junctions, we investigated the role of RIB in SMD activity further in immobilized worms (Fig. 4.35a). Our RIB::*hisCl* recordings contained periods of full RIB inhibition and periods of incomplete RIB inhibition, so we quantified SMD activity (frequency and amplitude) in periods of incomplete RIB inhibition (termed 'RIB high') and periods of full RIB inhibition (termed 'RIB low') (see Methods). We found that RIB inhibition led to decreased SMDD peak frequency, SMDD amplitude and SMDV amplitude in forward command states (Fig. 4.36a,b). Thus, the RIB interneuron class modulates SMD activity during forward command states. These results further suggest that RIB inhibition affects SMDD activity more strongly than SMDV. To summarize, RIB has a positively modulatory effect on SMD: SMD frequency and

amplitude correlates with the level of RIB activity, but it is not essential for SMD activity in the forward command state.

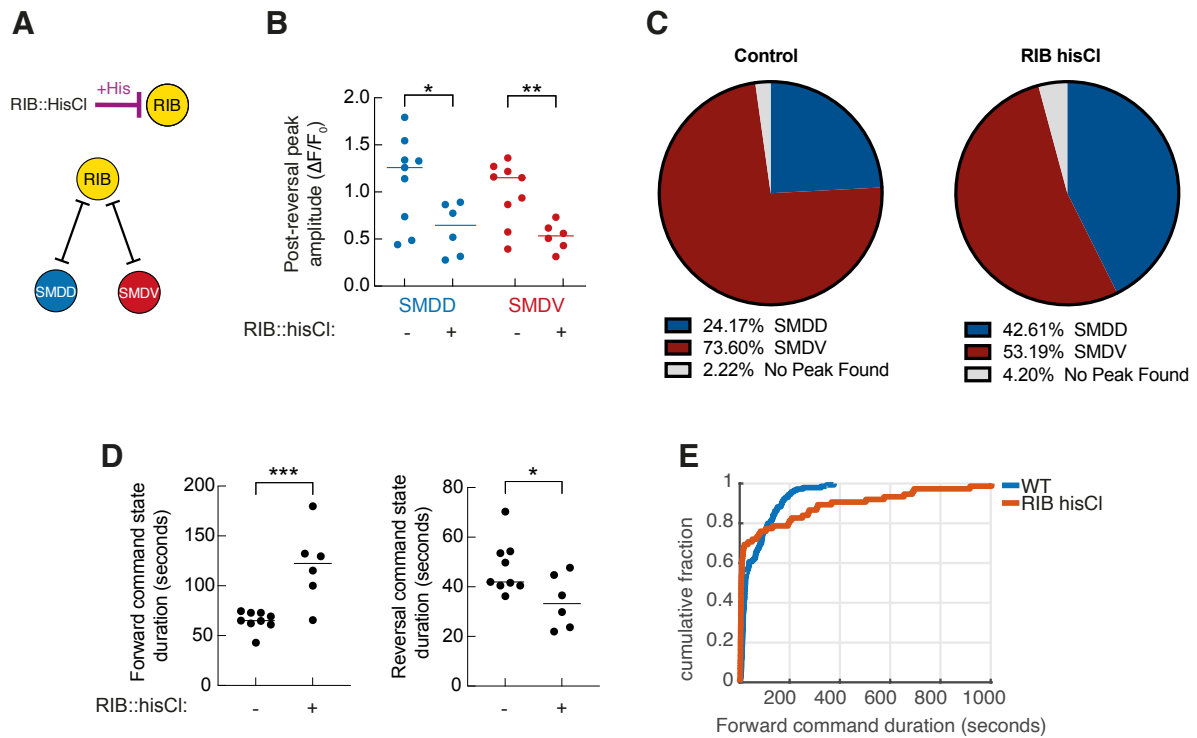


Figure 4.35. RIB inhibition affects the dominance of SMDV post-reversal end peaks over SMDD. (A) Experimental design. The RIB interneuron synapses onto both SMDD and SMDV via gap junctions. (B) Mean amplitude of post-reversal-command SMDD and SMDV GCaMP activity peaks across whole-brain recordings. - denotes lack of hisCl transgene and inhibition (control); + denotes presence of hisCl transgene and inhibition (RIB::hisCl). Each data point is from one animal. Control: N=9; RIB::hisCl: N=6 recordings. *p<0.05, **p<0.01, ***p<0.001, ****p<0.0001, unpaired T-test. (C) Proportion of reversal commands ending in SMDD (blue), SMDV (red) or no detected peaks (gray) in control (left) and RIB inhibition (RIB::hisCl, right), pooled over 9 control and 6 RIB::hisCl whole-brain recordings. (D) Mean forward (left) and reversal (right) command state durations across control and RIB inhibition whole-brain recordings. - denotes lack of hisCl transgene and inhibition (control); + denotes presence of hisCl transgene and inhibition (RIB::hisCl). Each data point is from one animal. Control: N=9; RIB::hisCl: N=6 recordings. ns, not significant; *p<0.05, **p<0.01, ***p<0.001, ****p<0.0001, unpaired T-test. (E) Cumulative distribution of forward command state durations across control and RIB inhibition whole-brain recordings. Control: N=9; RIB::hisCl: N=6 recordings.

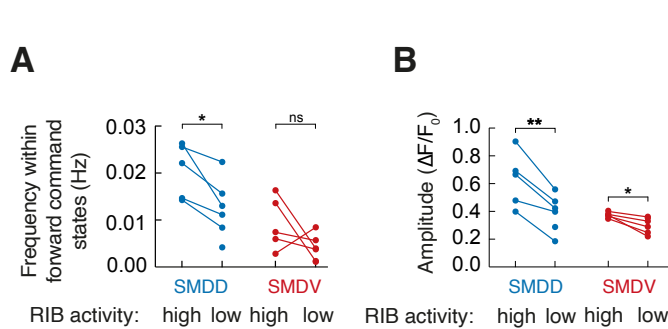


Figure 4.36. RIB activity modulates SMD activity in forward command states. (A-B) Mean (A) frequency and (B) amplitude of SMDD and SMDV GCaMP activity peaks in forward command states across RIB::hisCl whole-brain recordings. Because RIB inhibition was partly incomplete, we differentiated between timepoints where RIB was active (“RIB high”) and timepoints where RIB was silent (“RIB low”) (see Methods). *p<0.05, **p<0.01, ***p<0.001, ****p<0.0001, paired T-test. N=6 RIB::hisCl recordings.

5. Discussion

5.1 Research aims and key findings

Animals rely on the ability to move spontaneously and actively; individual motor actions are coordinated into longer-lasting action sequences by the nervous system. How the nervous system orchestrates the seamless execution of behaviors at different timescales is a fundamental question in neuroscience. A hierarchical organization of behavior has been proposed as a potential fundamental principle of behavior for decades. Behavioral hierarchies have been described previously, but mostly, it remains unclear whether it is a practical description of behavior or indeed a fundamental organizational principle. To differentiate these possibilities, the neuronal mechanisms underlying hierarchically-organized behavior need to be investigated. The goal of this thesis was to explore the neuronal underpinnings of a behavioral hierarchy that we recently described in *C. elegans* (Kaplan *et al.* 2020). Specifically, we aimed to identify the neurons driving hierarchically-organized behavior and to understand the relationships between their activities and to the global neuronal representation of locomotor commands. Further, locomotion often involves the rhythmic control of body parts, and thus requires the activity of Central Pattern Generators (CPGs). CPGs are often studied in isolation. Among the neurons involved in this behavioral hierarchy, we believe we have uncovered a CPG circuit for head movements. Thus, another aim of this project was to explore how CPG activity is coupled to global nervous system activity and how CPG participants are modulated to fulfill different functions depending on the overarching hierarchical state.

Our recent work uncovered a behavioral hierarchy in *C. elegans* spanning three timescales. At the uppermost hierarchical level, worms alternate between forward and backward locomotion. Within the longer-lasting forward crawling state, there are two behavioral motifs: propagated-bends and head-casts. Propagated-bends make up the undulatory body wave and correspond to the second level of this hierarchy. At the lowermost level, nested within propagated-bends, we found unilateral head bends called head-casts (Kaplan *et al.* 2020). This work identified the neurons and circuits that drive these behaviors and that implement the hierarchy (Fig. 5.1a). Previous work showed that global neuronal activity in the head ganglia represents the worm's major motor commands; we confirmed that neurons throughout the nervous system, and not only the head ganglia, participate in this representation (Kato *et al.* 2015). We confirmed that B-MNs in the Ventral Nerve Cord drive propagated bends, and identified the SMD head motor neurons as the drivers of head-casting behavior. We found that B-MN- and SMD activity are phase nested, such that head-casting occurs only at specific phases of the propagated-bend cycle. The B-MNs are toggled between states by the upper hierarchical level— active within Forward crawling, inactive within Reversals—, while the SMDs are toggled between functional roles, as they are active during both states. We found that the SMDs drive head-casting within Forward

crawling, and post-reversal turning upon Reversal execution; this modulation is based on intrinsic neuronal circuit interactions network-based rather than dependent on sensory inputs from proprioception, the animal's movement, and/or the environment. The SMD neurons are toggled between two different functions depending on the overarching behavioral state and pose an entry point to study the mechanisms through which this is achieved by the nervous system. We explored how they are modulated by specific neurons participating in the Forward-Reverse cycle, as well as some of the molecular mechanisms that may give rise to their activity.

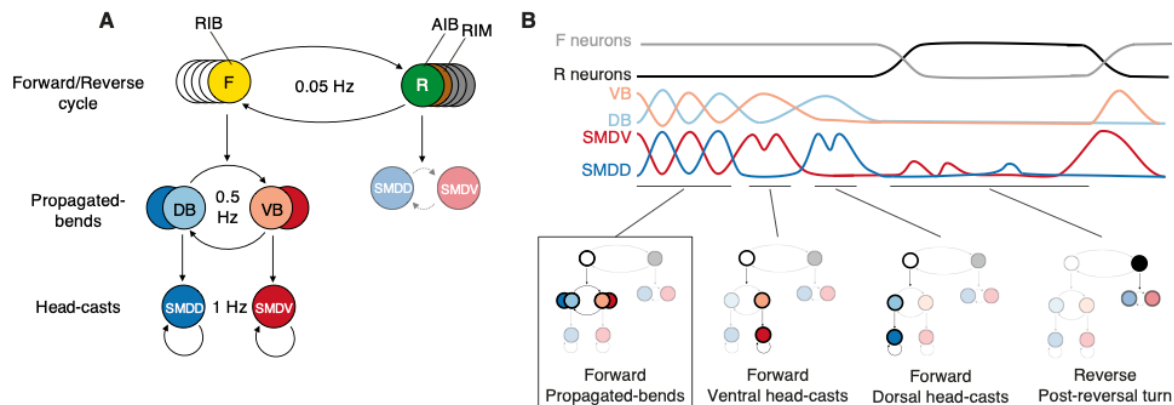


Figure 5.1. A hierarchical control mechanism for behavioral flexibility. (from Kaplan et al, 2020) **(A)** Neuron classes (F = forward-active neurons, R = reverse-active neurons) underlying each behavior. **(B)** Model traces (upper) and corresponding behavioral and neuronal hierarchy states (lower).

5.2. Slow and global vs. fast and local dynamics

Our results propose that a hierarchy of neuronal activity gives rise to a hierarchy of motor behaviors in *C. elegans*. The longer-lasting motor program of the uppermost hierarchical level is represented by slow, global dynamics permeating the activity of many neurons; faster-timescale behaviors are reflected in the fast, local dynamics of select motor neurons, the peripheral effectors. Further, neuronal activity representing the higher-level behavioral state gates the activity of the faster neuronal activities that drive the lower-level behaviors. Consequently, the activity of peripheral effectors contains signatures of multiple levels of behavior; the upper hierarchical level and the level that they drive. These relationships of slow dynamics representing longer-lasting behavioral states and fast dynamics representing local movements are reminiscent of studies of *Drosophila* brain activity during spontaneous behavior (Schaffer et al. 2021). This study found that the activity of many neurons correlated with vigorous behavioral states, such as instantaneous running or flailing, probably involving many muscles and neurons, while spatially restricted clusters of neurons represent more localized movements, such as grooming. On a similar note, cortical neurons in the mammalian brain form networks with behavior-dependent oscillatory activity at various spatial and temporal scales: slow, widespread oscillations span very large networks of neurons and permeate large areas of the brain, while high frequency oscillations are constrained to small networks of neurons (Buzsáki and Draguhn 2004).

It has been suggested that slow oscillations can modulate faster, local cortical rhythms; widespread oscillations then provide a mechanism for distant, local networks to be synchronized by the coupling of their rhythms (Buzsáki and Draguhn 2004). Thus, oscillations allow for computations occurring in distant areas of the nervous system to be coupled. Thus, a picture emerges where a hierarchy of neuronal activity organizes the representation of different time scales of behavior, and neuronal representations of behavior are nested across spatial scales.

5.3. A hierarchy of states

The behavioral hierarchy repurposes the activity of neurons for different functions in different contexts. This is achieved by the modulation of the SMDs by neurons that participate in the global dynamics that represent the uppermost level of the hierarchy. RIM and AIB neurons are involved in backward locomotion and negatively modulate SMD activity in that state (Fig. 4.28, Fig. 4.29), while RIB, whose activity correlates with forward crawling speed, positively modulates SMD activity (Fig. 4.35, Fig. 4.36) (Gray, Hill, and Bargmann 2005; Kocabas et al. 2012; Z. Li et al. 2014; Kato et al. 2015; Y. Wang et al. 2020). These findings start to paint a picture of how hierarchical control can orchestrate and coordinate behaviors at different timescales. An interesting feature of this system is that SMD activity promotes turning behavior and therefore transitions between behavioral states (Fig. 4.25, more evidence in (Kaplan et al. 2020)). The activity of a lower hierarchical level neuron affecting the upper-level Forward-Reverse cycle may seem like a contradiction to the proposed hierarchy model. Our data fits a model of a hierarchy of neuronal dynamical states, rather than a hierarchy of neurons. In this model, each hierarchical level is composed of states, and each state is associated with specific activity patterns across many neurons (Fig. 5.1b), rather than a hierarchy of neurons that occupy singular states (Kaplan et al. 2020). In accordance to this, the interneuron RIB was recently identified as playing roles in both forward crawling and in promoting reorientation turns, providing another example of a neuron that is involved in different behavioral states (Y. Wang et al. 2020). Thus, a hierarchy of neuronal states allows for neurons to participate in more than one behavior and thus creates a network of neurons that can potentially fulfill multiple functions.

5.4. Neuronal underpinnings of hierarchical relationships

Hierarchically organized behavior does not require the neuronal mechanisms that drive it to follow a hierarchical logic. This is best exemplified by zebra finch song, which is hierarchically organized, yet generated by a feedforward chain of synaptically-connected neurons (Glaze and Troyer 2006; Long, Jin, and Fee 2010). Thus, one of the most pressing questions we set out to answer was whether neuronal activity reflected the hierarchical organization of behavior, and which mechanisms establish these relationships. The neuronal activities we observed in immobilized worms suggest that it is mostly enabled by neuronal connections, rather than being dependent on sensory feedback, either

from the worm's own movement, proprioception, or sensory inputs from the environment. The worm's known synaptic connectivity is very informative (J. G. White et al. 1986). The most straightforward relationship is perhaps hierarchical level I (the forward-reverse switch) gating the occurrence of hierarchical level II (propagated-bends): the selective activation of B-MNs during forward command states is facilitated by the existing gap junction connections between them and descending interneurons such as AVB (J. G. White et al. 1986; Kawano et al. 2011; Xu et al. 2018). The uppermost hierarchical level toggles SMDs between functional roles: during forward crawling, SMD activity promotes head-casting; during reversals, they promote the termination of the reversal crawling state and drive the subsequent reorientation turns. Their peak amplitudes and frequencies are modulated by the Forward/Reverse cycle. Our data implicates reversal-active interneurons AIB and RIM in SMD modulation (as mentioned above), and these relationships are also supported by synaptic connections from AIB and RIM to SMD (J. G. White et al. 1986). We also identified that RIB activity, which correlates with forward locomotion speed, promotes SMD activity; this relationship can be explained by synaptic connectivity as well (J. G. White et al. 1986).

Propagated-bends (level II) and head-casts (level III) are phase-nested, such that head-casts occur at specific phases of the propagated-bend cycle. This relationship is also reflected in SMD activity: their activity peaks during forward crawling coincide with both propagated-bends and head-casts. SMD activity is synchronized to head bends occurring during propagated-bends and head-casts, but our data show that SMD inhibition does not abolish propagated-bends. Thus, the SMDs likely act as followers during propagated-bends and only drive head-casts. Inputs from other neurons, or proprioception, might entrain SMD with both B-MNs and propagated bends. If they are entrained through neuronal connections, SMD should receive input from propagated-bend-active neurons, such as the B-MNs. There is a direct link between SMDs and B-MNs, a gap junction connection between VB01 and SMDVR. This connection could couple the head-cast and propagated-bend oscillators. However, no B-MN directly synapses onto SMDD and our data revealed no correlation between SMDD and B-MNs (White 1986). Thus, so far we have an incomplete understanding of how SMD activity is coupled to propagated-bends, because there is a straightforward link between the propagated-bend cycle and SMDV, but not SMDD. SMDD could be entrained through periodical inhibition from SMDV, which is electrically coupled to VB01 and reciprocally connected to SMDD; this possibility is explored below. Alternatively, inputs from other neurons might entrain SMD with the propagated-bend cycle. In our recent work, we examined two major inputs of the SMDs, RIA and RME (Kaplan et al. 2020). RIA is the most prominent presynaptic partner and a modulator of SMD activity in freely moving worms; RME is a GABAergic motor neuron known to modulate SMD activity during head bending, and whose activity correlated with SMD in our imaging datasets (Fig. 4.8) (Hendricks et al. 2012; Shen et al. 2016; Q. Liu et al. 2018). However, we found no effect of RIA or RME manipulations on the correlation between SMD activity and head-bending (Kaplan et al. 2020). Alternatively, SMDD coupling to the propagated-bend cycle could be achieved through an indirect link: a gap junction between the VD01

motor neuron and SMDDR. VD01 is a GABAergic, inhibitory motor neuron postsynaptic to B-MNs VB01 and DB01 (J. G. White et al. 1986). Thus, VB01 could inhibit SMDD during ventral propagated-bends through VD01. This connection would explain our observation that in *unc-9* innexin mutants, VB01 and SMDV are not coupled, yet SMDD and VB01 are still anti-correlated (Fig. 4.23b, especially right panel). Our immobilized calcium imaging data does not support a correlation between VD01 activity and VB01, DB01, or SMD. However, VD01 activity could be obscured by our imaging paradigm, since we restrict GCaMP expression to the cell nucleus and activity fluctuations occurring only in the soma may not be detected. Another plausible mechanism through which these behaviors are coupled is through proprioception. We hypothesize that proprioception plays an important role in synchronizing SMDD activity with propagated-bend-related head-bending, given that both the SMDs and B-MNs are proprioceptive – SMDV could be coupled to the propagated-bend cycle through its electrical connection to VB01 (J. G. White et al. 1986; Wen et al. 2012; Yeon et al. 2018). Such a configuration would align with observations that *trp-1*, *trp-2* proprioceptive channel mutants have a ventral bias during forward locomotion (Yeon et al. 2018). Thus, we propose two alternatives for the mechanism that entrains SMD to the propagated-bend oscillation: one possibility is through a combination of electrical connections between SMDV and VB01, and proprioception in SMDD; the second option is the direct connection from VB01 to SMDV, and an indirect inhibition of SMDD by VB01 through GABAergic motor neuron VD01. Future work could aim to investigate the importance of VD01 and/or proprioception in the coupling of SMDD to the propagated bend cycle. Nevertheless, our immobilized imaging data show that many hierarchical relationships are based on circuit interactions rather than feedback from proprioception or behavioral execution. This suggests that a hierarchical organization of neuronal activities, independent of behavioral execution, creates hierarchically-organized behavior.

5.5. Modulation of the hierarchy

The behavioral hierarchy described here is restrictive, because lower-level behaviors can only be accessed by one mid-level state. This is exemplified by our observations that when the animal is performing a dorsal propagated-bend, it must first switch to a ventral propagated-bend in order to perform a ventral head-cast (Kaplan et al. 2020). In line with this, the SMDs only show head-cast related activity peaks during propagated-bends of the same side (SMDD during dorsal- and SMDV during ventral propagated-bends). Thus, this behavioral hierarchy is best described as a non-overlapping hierarchy, where lower-level behaviors cannot be accessed by multiple upper-level states (R. Dawkins 1976). Although it is a rigid framework, phase-nesting provides a great substrate for potential behavioral regulation, because manipulating the propagated-bend cycle speed can make it more or less probable for head-casts to occur. Crawling speed therefore narrows or widens the window of opportunity for head-cast occurrence. Although exploring the regulation of head-cast occurrence was not within the

scope of this thesis, work from our lab done by H. Kaplan and N. Khoss shows that both crawling speed regulation and sensory stimuli could affect head-cast probability ((Kaplan et al. 2020), Figure 8). Decreasing O_2 concentration – which slows down the animal, presumably to explore locally – resulted in longer propagated bend cycles and more head-casting (Zimmer et al. 2009; Hums et al. 2016; Kaplan et al. 2020). Similarly, inhibiting RIB activity– a neuron linearly correlated with crawling speed– elongated propagated-bend cycle periods and increased head-casting frequency (Kato et al. 2015; Kaplan et al. 2020). These data show that it is a rigid framework that can nevertheless be modulated by behavioral state and incoming sensory input. These RIB inhibition experiments performed on freely moving animals showed an increase in propagated-bend cycle period and an increase in head-casting frequency (Kaplan et al. 2020). These results contradict the immobilized RIB::hisCl experiments presented in this thesis, where RIB inhibition resulted in lower SMD frequencies in immobilized animals (Fig. 4.36). Decreasing ambient O_2 concentration modulates the animal's forward crawling speed (Zimmer et al. 2009). The results from RIB inhibition in freely moving animals are in agreement with those from the O_2 manipulations. Therefore, we are inclined to think that the immobilized imaging condition could lack inputs that would be required to obtain comparable results from these different paradigms. These inputs could be movement-, sensory- and/or exploration-related.

Zooming out on worm behavior on longer timescales, it has been previously described that when animals are crawling on food, they spontaneously switch between dwelling and roaming states (Fujiwara, Sengupta, and McIntire 2002). Dwelling can be described as a low-speed exploitative state, where worms do not travel far and mostly explore the local environment; roaming is a high-speed explorative state where fast forward crawling is upregulated (Fujiwara, Sengupta, and McIntire 2002). We believe that the roaming and dwelling states modulate the motor hierarchy we describe: dwelling is characterized by short forward-directed movements, and increased head-casting and reversals; roaming is characterized by long-range, fast forward-directed locomotion and fewer head-casts (Gallagher et al. 2013; Kaplan et al. 2020). Roaming and dwelling states differ in the probabilities of motor actions to occur, and do not completely restrict their occurrence within a particular state. In other words, head-casting and reversals still occur during roaming states, but with lower probabilities. This is in contrast to the behavioral hierarchy we describe, which is a non-overlapping hierarchy that aligns more with recent studies of hierarchies at the level of motor actions (Wiltschko et al. 2015; Berman, Bialek, and Shaevitz 2016; Gomez-Marin, Stephens, and Brown 2016; Marques et al. 2018). Because roaming and dwelling states modulate the frequency of reversals and head-casts, they are better described as an overlapping hierarchy (R. Dawkins 1976; Kaplan et al. 2020). Roaming and dwelling pose a control mechanism for this motor hierarchy that allows for behavioral flexibility, because the nervous system can generate different behavioral programs by re-utilizing motor actions in different ways. This longer-lasting modulation of behavior relies on neuromodulation (Ben Arous, Laffont, and Chatenay 2009;

Flavell et al. 2013). Interestingly, one of the few described examples of a behavioral hierarchy in *C. elegans*, the swimming/crawling hierarchy, also relies on neuromodulation (A. Vidal-Gadea et al. 2011; A. G. Vidal-Gadea and Pierce-Shimomura 2012). In this case, crawling or swimming states respectively permit or suppress behaviors such as defecation, egg-laying and food ingestion, and the suppression of these behaviors during swimming relies on neuromodulation. This example is consistent with a non-overlapping hierarchy, in contrast to roaming/dwelling. Thus, both overlapping and non-overlapping behavioral hierarchies can be found in *C. elegans*, and they are modulated via circuit mechanisms and/or neuromodulation. To summarize, hierarchical control can be found throughout the *C. elegans* nervous system.

5.6. Modulation by the hierarchy

A major feature of hierarchies of control is that they can serve as a mechanism to modulate neuronal activities depending on the upper hierarchical level. Hierarchical control of neuronal activity can be achieved through the differential modulation of neuronal substrates in different hierarchical states. Concomitant with their different behavioral roles, we observed that SMD peak frequency and amplitude differ between backward and forward locomotion. We aimed to understand the mechanism through which SMD modulation is achieved. In *C. elegans*, many neurons participate in the neuronal representation of the uppermost hierarchical level, the forward-reverse cycle; the *C. elegans* nervous system is highly interconnected (Varshney et al. 2011; Towlson et al. 2013; Uzel, Kato, and Zimmer 2022). Befittingly, SMDs are synaptically connected to forward- and backward-active neurons. We investigated the role of backward-active AIB and RIM neurons, and found that inhibiting AIB and RIM abolishes SMD activity differences between forward and backward crawling (Fig. 5.1). RIM is known for its role during escape responses, where worms perform reversals and suppress head movements upon anterior touch (Alkema et al. 2005; Pirri et al. 2009). During reversal escape responses, RIM releases tyramine and inhibits forward command interneuron AVB, but more interestingly, head/neck muscles, through activation of the LGC-55 chloride channel (Pirri et al. 2009; Pirri and Alkema 2012). Our data showed that SMD inhibition during backward locomotion (not exclusively the escape response) occurs via RIM and also relies on LGC-55 activation. Thus, tyramine release collectively inhibits SMD and head neck muscles to suppress head movements during reversals. We assume that this inhibition is lifted upon reversal end, allowing the SMD post-reversal activity peaks and the execution of head/neck bending during post-reversal turns. We hypothesize that this inhibition and the consequent release from inhibition contribute to the modulation of SMD, such that head movements are suppressed during reversals, and SMD drives reorientation turns upon reversal end. Conversely, we investigated the role of forward-active RIB neurons in the modulation of SMD during the forward locomotion state. We found that inhibiting RIB in immobilized animals decreased SMD activity in forward command states, and interestingly, also reduced the amplitude of post-reversal SMD peaks.

This hints at a role of RIB in potentiating SMD activity, both promoting activity related to head-casts and reorientation turns. In summary, our data give insights into how hierarchical organization differentially modulates neuronal substrates, such that the same neuron class performs different functional roles depending on the overarching behavioral state (Fig. 5.1). In the future, we should confirm the importance of RIM and RIB activity for the function of SMD during post-reversal reorientation turns, by assessing whether inhibiting these neurons affects reorientation turns.

5.7. A model for Central Pattern Generation in forward locomotion

Worm locomotion has been a source of speculation for some time; more specifically, how alternating sinusoidal body bending waves are generated and propagated. A landmark study that focused on motor neurons active during forward locomotion reported that B-MNs sense the bending of immediately-anterior body segments (Wen et al. 2012). This suggested that bending originated in the head region could be propagated through proprioception, and thus it was thought that worms potentially require one head CPG (Wen et al. 2012). Years later, studies suggested that the B-MNs (or small circuits containing B-MNs) are independent rhythm generators, and it was hypothesized that rhythmogenic B-MN circuits plus an unidentified head neuron CPG generate the rhythmic activity to drive forward locomotion (Fouad et al. 2018; Xu et al. 2018). However, B-MN activity had not been imaged in conditions that preclude rhythmic sensory input. Our data show that the B-MNs act as independent rhythm generators, and suggest that pattern generation (beyond rhythm generation) in the B-MNs requires proprioceptive feedback, consistent with previous studies (Wen et al. 2012; Fouad et al. 2018; Xu et al. 2018). Further, we identified the SMDs as pattern generators for head-casting movements, since their activity is rhythmic and alternating – fulfilling rhythm and pattern generation– in immobilized conditions. The SMDs have also been identified as proprioceptive, and the calcium dynamics of B-MNs and SMD recorded in immobilized conditions are one order of magnitude slower than in freely moving animals (Fig. 4.11) (Yeon et al. 2018). This is reminiscent of the frequency reduction observed in other studies of CPGs in sensory-deprived conditions (Fox, Soll, and Wu 2006; Goulding 2009). Thus, we hypothesize that both B-MN and SMD activity requires proprioceptive input for their entrainment. Our data and others' suggest that the B-MNs constitute a body CPG. Further, our data suggest the SMDs participate in a head neuron CPG for head-casting movements (in contrast to the head neuron CPG for forward locomotion hypothesized previously (Wen et al. 2012; Fouad et al. 2018). We hypothesize that the SMDs generate rhythmic activity to drive head-casts, and that other head motor neurons could potentially generate rhythmic activity to drive other kinds of head movements. Further, we propose that B-MNs generate rhythmic activity that drive propagated bends within forward locomotion; we hypothesize that they require proprioceptive input and electrical coupling to neighboring B-MNs for their entrainment and for the generation of more complete activity

patterns that ensure the propagation of the body bending wave. Further, we hypothesize that the SMD and B-MN oscillator circuits are coupled to ensure coherent forward locomotion.

Our calcium imaging recordings in immobilized animals reveal that neurons involved in the head and body oscillators (SMDV and VB01) have coordinated activity in conditions that preclude proprioception, hinting at a role of synaptic connections in their coordination. We focused on understanding the importance of VB01 activity on SMD pattern generation. We investigated VB01 and SMDV activity in *unc-7 unc-9* innexin mutants and found a dramatic loss in the correlation of their activities; a similar effect was observed in *unc-9* single mutants. Further, VB01 activity persists in conditions where SMD is silent, and we observed that SMDD, SMDV and VB01 can oscillate independently in *unc-9* mutants. These data hint at an entrainment of SMDV activity by VB01 and suggest that the synchrony between SMDV and VB01 observed in immobilized animals depends on UNC-9 innexins (Fig. 5.2). However, we could not draw many conclusions from these experiments, as gap junction mutations affect many other neurons. Understanding the directionality of the VB01-SMDV coupling will require understanding which isoforms of UNC-7 are expressed in these neurons, and future work should focus on cell-specific rescues of gap junction mutations to disentangle the role of VB01 activity on SMD pattern generation (Shui et al. 2020).

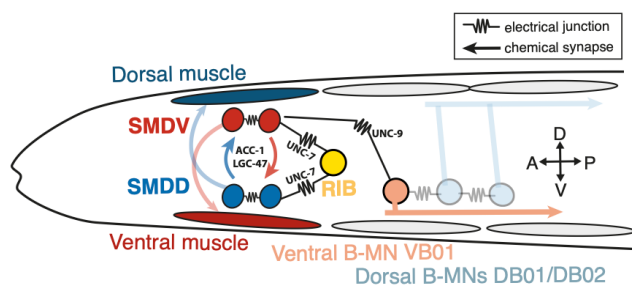


Figure 5.2. The role of gap junctions and ACh-gated chloride channels in SMD activity. Worm head schematic illustrating positions and lateralized muscle innervations of CPG candidate motor neurons and their synaptic and electrical connections to key neurons. ACC-1 and LGC-47 refer to ACh-gated chloride channels that we hypothesize underlie SMD antagonism; UNC-7 and UNC-9 refer to innexins. We hypothesize that RIB provides excitatory input to SMDs in forward command states via UNC-7, while UNC-9 underlies the SMDV-VB01 coordination. Cell bodies and projections not shown to scale. A: anterior; P: posterior; D: dorsal; V: ventral.

5.8. The hierarchical control of CPGs

This work bears resemblance to studies on the circuits that drive multi-timescale orofacial behaviors such as chewing, swallowing, breathing, and whisking in rodents. Most of these behaviors are rhythmic and driven by separable oscillators (Kleinfeld et al. 2014). Their frequencies and phase-locked relationships suggest a hierarchical organization where some rhythms influence others in a unidirectional manner. A major advantage of hierarchical control could be ensuring that behaviors do not interfere with one another and coordinating the activities of motor neurons that target overlapping body parts. Consistent with this, it seems that the rhythms of several orofacial behaviors are controlled by the breathing CPG (see (Moore et al. 2013) for whisking, (Katakura, Jia, and Nakamura 1995)

and (Nakamura, Katakura, and Nakajima 1999) for licking). This is best exemplified by the hierarchical relationship between the breathing and whisking behaviors and oscillators: breathing resets the whisking phase, but whisking does not affect the breathing phase. Further, a unidirectional anatomical pathway was found from the breathing CPG area to the whisking CPG (Moore et al. 2013). This relationship is reminiscent of the phase-nesting of head-cast-related activity peaks in the propagated-bend cycle: altering the propagated-bend rhythm can permit or restrict head-cast occurrence, but head-casting does not influence the propagated-bend cycle (Kaplan et al. 2020). Further, the phase resetting observed in rodent CPGs could explain how SMD oscillations may be restricted into particular phases of the B-MN oscillation cycle and ensure unilateral oscillations (and head-casts). Thus, hierarchical control poses a strategy for coordinating interrelated behaviors and ensuring that CPGs controlling overlapping body parts do not interfere with one another.

Orofacial behaviors are also important for sensory information gathering. Rodent exploration involves the coordinated movements of the head, nose and whiskers (Welker 1964). In addition to the coordination of the whisking oscillator to the breathing cycle, more recent work has shown that nose and head movements are also coordinated with the breathing rhythm (Moore et al. 2013; Kurnikova et al. 2017). Thus, coupling of exploratory orofacial behaviors to the breathing cycle has been proposed as a mechanism for sensory integration by temporally binding the perception of tactile and olfactory information (Kleinfeld et al. 2014). Similarly, in *C. elegans*, hierarchical control could aid sensory integration. SMD activity, which drives head-casting, contains signatures of both propagated-bends and head-casts. SMDs heavily connect to the RIA interneurons; RIAs receive information from multiple sensory networks and compartmentalized head-bend information from SMDs, which allows the animal to discriminate the location of odor sources (J. G. White et al. 1986; Hendricks et al. 2012).

Rhythmic motor patterns such as whisking can be modulated by sensory information: whisking is slowed down upon contact with an object, which may enhance sensation of tactile stimuli (Grant et al. 2009). Analogously, in *C. elegans*, we hypothesize that head-casting is important for information gathering because in conditions that promote exploratory behavior, such as oxygen shifts and the dwelling state, head-casting frequencies are increased (Kaplan et al. 2020). To summarize, hierarchically-controlled CPGs are modulated by sensory information, and they could facilitate the integration of sensory information in rodents and worms.

The coordination within and among orofacial CPG circuits is thought to be based on three mechanisms: (I) local interactions between potentially co-active circuits; (II) top-down control by central command systems mediating the execution and modulation of behaviors; and (III) peripheral feedback orchestrating the timing of different muscle groups (see (Kleinfeld et al. 2014) for an overview of supporting evidence). We believe we find these coordination mechanisms in the behavioral hierarchy we describe: (I) mutual inhibition through inhibitory cholinergic signaling of the SMD head-cast oscillators ensures they are not co-active, and gap junctions partially synchronize the SMD head-cast- and B-MN propagated-bend circuits; (II) the activity of the oscillators are gated by participants of the

forward-reverse cycle (i.e. AVB activates B-MNS); and (III) proprioceptive feedback is required for generating the undulatory pattern. Taken together, this hierarchy of CPG control has many similarities to the CPG circuits that ensure the complex orchestration of multiple rhythms of orofacial actions in rodents. *C. elegans* provides the advantages of allowing for access to the activity of all neurons, as well as information on the identities of all cells involved, and the connections between them. On the other hand, the rodent brainstem alone contains at least ten CPGs, such that studies in rodents will elucidate how hierarchical control achieves behavioral coordination at a much more complex scale. Nevertheless, both *C. elegans* and rodent studies are contributing to expanding our understanding of the strategies for behavioral coordination by the nervous system.

5.9. Motor neurons that multitask

The activity of the SMD class is fascinating; it shows signatures of all levels of this hierarchy, and it plays a role in different behaviors depending on the overarching behavioral state. During forward crawling, the SMDs drive head-casting behavior. During reverse locomotion, their activity is uncoupled from head movements; it promotes the termination of the reversal command and executes post-reversal turns. Thus, the SMDs perform motor- and interneuron roles, as they promote behavioral state transitions. This multifunctionality is enabled by hierarchical organization and control. In addition to their motor- and interneuron roles, the SMDs have also been identified as proprioceptive (Yeon et al. 2018). One could even say that the SMDs are sensory-motor-interneurons. Other motor neurons in *C. elegans*, the B-MNs, have also been identified as having mechanosensitive capabilities, and have been regarded as “motor neurons that multitask” (Wen et al. 2012; Goulding 2012). Our data and others’ now identify them as motor neurons that generate rhythmic activity in addition to mechanosensation (Xu et al. 2018; Fouad et al. 2018; Kaplan et al. 2020). Another example of multi-tasking motor neurons can be found in the stomatogastric ganglion of crustaceans, where motor neurons innervating the gut muscles also generate the rhythmic activity patterns required for food consumption and digestion (Harris-Warrick et al. 1992). These examples come from invertebrate studies; rodent studies have hinted at a different kind of multifunctional neurons: here, it has been observed that the same brainstem neurons respond to different orofacial behaviors (Moore, Kleinfeld, and Wang 2014). Thus, it has been suggested that CPGs may control multiple orofacial behaviors, though the anatomical and neurophysiological evidence for this is incomplete. In this case, neurons are multifunctional in that they participate in the rhythm generation for different behaviors, but not in the sense of fulfilling different functions, such as rhythm generation, proprioception and muscle activation, as is the case in the *C. elegans* and *crustacean* examples. Nevertheless, multifunctional motor neurons seem not to be an idiosyncrasy of the *C. elegans* nervous system, but rather a generalizable feature of compact neuronal circuits.

5.10. The regulation of behavioral state transitions

A fascinating aspect of this motor neuron network is the involvement of the SMDs in promoting reversal state termination and driving the subsequent post-reversal turn. This suggests that this motor neuron class also plays an interneuron role and influences the global transitions between behavioral states. Our experiments have uncovered further regulation of the SMD post-reversal turn activity; I will discuss these findings briefly.

We inhibited forward-active interneuron RIB and observed a decrease in SMD post-reversal peak amplitudes (Fig. 35a). This suggests that RIB activity is involved in the modulation of post-reversal SMD activity— and thus reorientation turns—, and is consistent with recent reports that RIB activation during forward locomotion promotes omega turns (Y. Wang et al. 2020). We hypothesize that SMD receives excitatory input from RIB at the reversal-forward transition and this input potentiates SMD post-reversal peaks. Further, we observed a decrease in the proportion of ventral turn commands (reversal ends associated with SMDV peaks, which in freely-moving worms coincides with ventral-directed turns). Therefore, we suggest that RIB may play a role in biasing the dorsal/ventral turn decision towards a ventral turn command. RIB and SMD are connected via gap junctions; somewhat consistent with this, we also observed decreases in post-reversal SMD peak amplitudes in *unc-9* innexin mutants (Fig. 5.2). These effects were statistically significant for SMDD, and not significant, but with an observable trend, for SMDV.

We also explored the effects of cholinergic inhibitory signaling and potentially mutual inhibition in SMD activity. We assessed the role of ACh-gated chloride channels ACC-1 and LGC-47 on SMD antagonism. We observed coincident SMDD and SMDV activity peaks in both *acc-1* and *lgc-47* mutants; these were mostly restricted to the post-reversal end activity (Figs. 30-32). Thus, we suggest that ACh-gated chloride channels are important for the mutual exclusiveness of SMD activity, especially during post-reversal turns (Fig. 5.2). We hypothesize that at the reversal-forward command transition, the SMDs are released from inhibition (by AIB and RIM, potentially among others) and both receive input from the shared upstream neurons (among them potentially RIB) (Fig. 5.2). ACh-gated chloride channels could ensure that either SMDD or SMDV peaks upon reversal end, making the dorsal/ventral turn decision unequivocal.

5.11. Further limitations and future perspectives

Some of the limitations and interesting future experiments have been presented throughout the discussion section of this thesis. I will present further caveats and limitations of our approaches to tackle these aims, as well as exciting future research directions.

We screened for intrinsically rhythmic neurons throughout the nervous system. To this end, we recorded neuronal activity in immobilized animals paralyzed with tetramisole (and the *myo-3::hisCl* method, discussed below). We identify a few caveats with this method. Firstly, our acquisition rates

amounted to around 3 Hz or less. To confirm that neuronal dynamics were not obscured by acquisition rate, we performed single plane 50 Hz recordings of SMD activity (in (Kaplan et al. 2020)) and confirmed that <3 Hz volumetric recordings are indeed sufficient to capture SMD dynamics. However, we cannot exclude the possibility that we missed faster dynamics in other neurons. On a similar note, most immobilized calcium imaging made use of paralyzing agent tetramisole to paralyze the animals. Given that tetramisole is an ACh receptor agonist, we expect neuronal activities to be altered in this context and potentially some neuronal activities to be obscured by this tonic activation. To investigate this, we recorded whole-nervous-system neuronal activity using an alternative paralysis method—the expression of hisCl in body wall muscles (myo-3::hisCl)—and confirmed that global neuronal dynamics representing the forward-reverse cycle are preserved (Fig. 4.10). We could also observe SMD antagonism and VB01-SMDV coupling in these conditions (not shown). However, we did observe additional neurons active in myo-3::hisCl that are silent in tetramisole-paralyzed animals, especially neurons we hypothesize are head motor neurons. Investigating these neurons and their relationships to each other, the behavioral hierarchy, and locomotion in general was not within the scope of this thesis, but future work should focus on these questions.

Experimental constraints allowed us to record the neuronal activities of single/pairs of neurons in moving animals or whole-brain neuronal activity in immobilized worms. Ideally, one would record whole-brain neuronal activity in behaving worms. Such experiments will inform on how the head-cast and propagated-bend CPGs interact in changing environments and how they are modulated by the environment. Further, rhythmic motor patterns can be modulated and even initiated by external stimuli (Moore, Kleinfeld, and Wang 2014); whole-brain imaging in behaving animals could thus reveal further potential oscillators that are silent in the whole-brain, immobilized imaging condition. On a similar note, we recorded neuronal activity in worms constrained to 2D in the “freely moving imaging” paradigm—where worms were sandwiched between an agar pad and a coverslip— or in fully immobilized conditions. *C. elegans* in the wild explore 3D environments such as decomposing fruit, and though dorsoventral crawling is constrained to two dimensions, head movements enjoy more degrees of freedom (J. White 2018). It is plausible that there is a diversity of head movements – and neurons that drive them – that remains to be explored. In line with this, there are 38 motor neurons from 11 neuron classes that innervate head and neck muscles in the worm (J. G. White et al. 1986). Future work could record behavior and neuronal activity in 3D. This could reveal further behaviors within the hierarchy we described, as well as potential oscillators analogous to SMD for other head movement directions. Further, explorations of worm behavior and neuronal activity in 3D will help us understand how head-casting and head movements in other directions are integrated into locomotion, and how the participating oscillators interact with one another. Worm behavior in 3D could resemble the hierarchy of orofacial behaviors even more, with more CPG circuits controlling different aspects of head movement.

A caveat of our neuronal inhibition experiments is only relying on the use of histamine-gated chloride channel *hisCl*. *HisCl* allows us to acutely inhibit neurons of interest, which allowed us to study the effects of acute neuronal inhibition, as opposed to genetic or cell ablations in early larval stages. However, *hisCl* does not allow for fine-grained temporal control of neuronal inhibition—once histamine is applied, neurons are inhibited for the duration of the recording. Thus, we could not interrogate the relationships between neurons at fast timescales. To this end, optogenetic activation and inhibition experiments are better suited. For example, although *SMD::hisCl* affected the duration of reversal commands, future work should optogenetically activate single SMD neurons and confirm that their activity drives the termination of the reversal command and the execution of the post-reversal turn.

We investigated the generation and modulation of rhythmic activity in the SMD motor neurons. One of the questions we aimed to answer was how important VB01 activity is for SMD rhythm generation. We inhibited all cholinergic motor neurons – among them VB01 – in the ventral nerve cord and observed that SMDD activity was unaffected, while SMDV activity decreased (Fig. 4.12). On a similar note, we assessed the importance of gap junctions and ACh-gated chloride channels on SMD activity using mutant strains. *unc-9* innexin mutants showed VB01 active during forward command states, while the SMDs were silent, hinting at an instructive role of VB01 activity on SMDV and perhaps SMDD. All innexin and ACh-gated chloride channel components investigated are expressed in multiple neurons, which makes it difficult to make conclusions about causality or about the importance of specific connections (i.e. the VB01-SMDV gap junction). Because we could not find a promoter combination to target VB01 specifically, we did not perform UNC-9 rescues in VB01 or target *hisCl* inhibition to VB01. This study should be complemented with cell-specific genetic rescues to disentangle these relationships, especially cell-specific innexin rescues in VB01. Alternatively, rescues of UNC-9 using a ventral B-MN promoter should clarify the role of gap junction input from VB01 to SMDV, since VB01 is the only ventral B-MN electrically connected to SMDV. Acute optogenetic inhibition or laser ablations of the individual circuit participants should help disentangle the role of these neurons in the generation of rhythmic activity and behavior.

We observed SMD activity in immobilized animals that resembled that of freely-moving animals, implicating them as CPG circuit participants. Despite our efforts, it remains largely unclear how oscillatory SMD activity is generated. We could show that several neurons' inputs modulate SMD activity, such as AIB RIM and RIB activity. However, the only condition that abolished SMD oscillations was the *unc-7 unc-9* mutant, and this effect was restricted to the forward command state (Figs. 4.21-22). Many open questions remain: Which neurons' inputs drive SMD oscillations in the forward command state? Does SMD require tonic input in this state? What is the role of L/R pair gap junctions in SMD rhythm generation? Cell-specific innexin rescues of SMD gap junction partners may help answer some of them. We expected mutual inhibition facilitated by cholinergic signaling to play a major role in SMD antagonism and in the generation of SMD oscillatory activity. Our imaging experiments of *acc-1* and *lgc-47* ACh-gated chloride channel mutants showed that cholinergic mutual

inhibition plays a clear, albeit minor role. This phenotype is fascinating, as it suggests that specific neurotransmitter receptors are ultimately involved in the decision between a dorsal or a ventral turn. Therefore, future work should characterize the behavioral effects of *acc-1* and *lgc-47* mutations. Although *acc-1* and *lgc-47* mutants showed a clear phenotype of coincident SMDD/SMDV peaks at reversal command ends, these peaks accounted for 20% of total SMD peaks at most, and SMD activity during other command states was largely unaffected (e.g. still antagonistic). Nevertheless, we did not exhaustively explore the role of all ACh-gated chloride channels expressed in SMD. The ACC channel family includes eight subunit genes: ACC-1, ACC-2, ACC-3, ACC-4, LGC-46, LGC-47, LGC-48, and LGC-49 (Putrenko, Zakikhani, and Dent 2005; Wever, Farrington, and Dent 2015). Four subunits are reported to be expressed in SMD: ACC-1, ACC-4, LGC-46 and LGC-47 (Pereira et al. 2015; Wever, Farrington, and Dent 2015; Hardege et al. 2022). We assessed the role of the strongly-expressed subunits ACC-1 and LGC-47; future work should explore the role of ACC-4 and LGC-46. Additionally, it is possible that further ACh-gated inhibitory channels are uncharacterized. Preliminary data from our lab shows synchronized SMDD and SMDV activity in temperature-sensitive ACh mutants (Nadja Schneeweiss, Pedro Augusto). Thus, SMD antagonism is most likely driven by acetylcholine-mediated mutual inhibition, and additional inhibitory ACh channels are most likely at play.

The principal objectives of this work were threefold: to uncover the neuronal underpinnings of a behavioral hierarchy in *C. elegans*; to explore how a CPG circuit is integrated to and modulated by the global representations of longer timescale behavioral states; and to understand the mechanisms through which this CPG generates intrinsic rhythmic and patterned activity. Although many open research directions and future experiments remain, this work has contributed to a better understanding of the organization and orchestration of behavior by the nervous system. This work was done using *C. elegans*, but the parallels to other studies show that many of these lessons apply to other model organisms, expanding our understanding of behavior and neuronal activity.

6. Materials and methods

6.1. Animal culture and animal strains

Worms were maintained using standard methods and grown at 20°C on nematode growth media (NGM) plates seeded with *Escherichia Coli* OP50 as a food source (Brenner 1974). All experiments were performed on young, hermaphrodite *C. elegans* adults bearing the *lite-1* mutation (*ce314*), which reduces blue light and UV responses (Edwards et al. 2008; J. Liu et al. 2010; Gong et al. 2016). A detailed list of all transgenic strains used is provided in **Table 6.1**.

Table 6.1. (modified from Kaplan et al, 2020) Detailed strain list, related to Figures 1-8, S1-S8, with specific figure panels listed.

Strain name	Experiment	Genotype	Construct (plasmid no.) injection concentrations	Additional References
ZIM1466	Whole-brain imaging and whole-nervous-system imaging (RIS inhibition, control)	<i>lite-1</i> (<i>ce314</i>); <i>mzmEx877</i> ; <i>mzmIs52</i>	<i>Pnlr-1(-150;-1)::HisCl::SL2::mCherry</i> (pAN30) – linearized, 0.5ng/uL <i>Punc-122::dsred</i> – linearized, 4ng/uL <i>Punc-31::NLSGCaMP6f</i> (pTS100, codon-optimized and with introns) – linearized, 2.5ng/uL	<i>Pnlr-1</i> (Gendrel, Atlas, and Hobert 2016; Haklai-Topper et al. 2011); a gift from Drs. Marie Gendrel and Oliver Hobert, 150bp upstream of <i>nlr-1</i> ATG.
ZIM1564	Behavior assays, SMD inhibition	<i>lite-1</i> (<i>ce314</i>); <i>mzmEx929</i>	<i>Punc-7s::CreVDH</i> (pHK248) - 100ng/uL <i>Pmyo-3::mCherry</i> - 2ng/uL	<i>Punc-7s</i> (T. A. Starich et al. 2009) <i>CreVDH</i> (Ruijtenberg and van den Heuvel 2015)
ZIM1725	Behavior assays, SMD inhibition	<i>lite-1</i> (<i>ce314</i>); <i>mzmEx1018</i>	<i>Punc-7s::CreVDH</i> (pHK248) - 40ng/uL <i>Pmyo-3::mCherry</i> - 2ng/uL	<i>Punc-7s</i> (T. A. Starich et al. 2009) <i>CreVDH</i> (Ruijtenberg and van den Heuvel 2015)
ZIM1418	Behavior assays, SMD inhibition	<i>lite-1</i> (<i>ce314</i>); <i>mzmEx858</i>	<i>Pflp-22::DIO-HisCl::SL2::mCherry</i> (pHK244) - 60 ng/uL <i>Pelt-2::NLSdsRedNLS</i> - 5 ng/uL	<i>Pflp-22</i> (Kim and Li 2004) ; a gift from Dr. Kyuhung Kim <i>DIO</i> (Sohal et al. 2009)
ZIM1473	Behavior assays, cholinergic VNC motor neuron inhibition	<i>lite-1</i> (<i>ce314</i>); <i>mzmIs28</i>	<i>Punc-17beta::HisCl::SL2::mCherry</i> (pHK172) - 80ng/uL	<i>Punc-17beta</i> (Charlie et al. 2006); a gift from Dr. Kenneth Miller
ZIM1628	Whole-brain imaging, SMD inhibition	<i>lite-1</i> (<i>ce314</i>); <i>mzmEx877</i> ; <i>mzmEx929</i> ; <i>mzmIs52</i>	<i>Pnlr-1(-150;-1)::HisCl::SL2::mCherry</i> (pAN30) – linearized, 0.5ng/uL <i>Punc-122::dsred</i> – linearized, 4ng/uL <i>Punc-7s::CreVDH</i> (pHK248) - 100ng/uL <i>Pmyo-3::mCherry</i> - 2ng/uL	<i>Pnlr-1</i> (Gendrel, Atlas, and Hobert 2016; Haklai-Topper et al. 2011) ; a gift from Drs. Marie Gendrel and Oliver Hobert <i>Punc-7s</i> (T. A. Starich et al. 2009) <i>CreVDH</i> (Ruijtenberg and van den Heuvel 2015)

			<i>Punc-31::NLSGCaMP6f</i> (pTS100, codon-optimized and with introns) – linearized, 2.5ng/uL	
ZIM1748	Whole-brain imaging, SMD inhibition	<i>lite-1</i> (ce314); <i>mzmEx877</i> ; <i>mzmEx1018</i> ; <i>mzmIs52</i>	<i>Pnlr-1(-150;-1)::HisCl::SL2::mCherry</i> (pAN30) – linearized, 0.5ng/uL <i>Punc-122::dsred</i> – linearized, 4ng/uL <i>Punc-7s::CreVDH</i> (pHK248) - 40ng/uL <i>Pmyo-3::mCherry</i> - 2ng/uL <i>Punc-31::NLSGCaMP6f</i> (pTS100, codon-optimized and with introns) – linearized, 2.5ng/uL	<i>Pnlr-1</i> (Gendrel, Atlas, and Hobert 2016; Haklai-Topper et al. 2011) ; a gift from Drs. Marie Gendrel and Oliver Hobert <i>Punc-7s</i> (T. A. Starich et al. 2009) <i>CreVDH</i> (Ruijtenberg and van den Heuvel 2015)
ZIM1562	Whole-brain imaging, SMD inhibition	<i>lite-1</i> (ce314); <i>mzmEx877</i> ; <i>mzmEx858</i> ; <i>mzmIs52</i>	<i>Pnlr-1(-150;-1)::HisCl::SL2::mCherry</i> (pAN30) – linearized, 0.5ng/uL <i>Punc-122::dsred</i> – linearized, 4ng/uL <i>Pflp-22::DIO-HisCl::SL2::mCherry</i> (pHK244) - 60 ng/uL <i>Pelt-2::NLSdsRedNLS</i> - 5 ng/uL <i>Punc-31::NLSGCaMP6f</i> (pTS100, codon-optimized and with introns) – linearized, 2.5ng/uL	<i>Pnlr-1</i> (Gendrel, Atlas, and Hobert 2016; Haklai-Topper et al. 2011) ; a gift from Drs. Marie Gendrel and Oliver Hobert <i>Pflp-22</i> (Kim and Li 2004) ; a gift from Dr. Kyuhyung Kim <i>DIO</i> (Sohal et al. 2009)
ZIM1574	Whole-brain imaging, cholinergic VNC motor neuron inhibition	<i>lite-1</i> (ce314); <i>mzmEx877</i> ; <i>mzmIs28</i> ; <i>mzmIs52</i>	<i>Pnlr-1(-150;-1)::HisCl::SL2::mCherry</i> (pAN30) – linearized, 0.5ng/uL <i>Punc-122::dsred</i> – linearized, 4ng/uL <i>Punc-17beta::HisCl::SL2::mCherry</i> (pHK172) - 80ng/uL <i>Punc-31::NLSGCaMP6f</i> (pTS100, codon-optimized and with introns) – linearized, 2.5ng/uL	<i>Pnlr-1</i> (Gendrel, Atlas, and Hobert 2016; Haklai-Topper et al. 2011) ; a gift from Drs. Marie Gendrel and Oliver Hobert <i>Punc-17beta</i> (Charlie et al. 2006); a gift from Dr. Kenneth Miller
ZIM1658	Freely-moving imaging of DB activity	<i>lite-1</i> (ce314); <i>mzmEx981</i>	<i>Punc-17beta::NLSGCaMP6f</i> (pHK264, codon-optimized and with introns) – 20ng/uL <i>Punc-17beta::mCherry::his58</i> (pHK114) – 40ng/uL	<i>Punc-17beta</i> (Charlie et al. 2006); a gift from Dr. Kenneth Miller
ZIM1467	Freely-moving imaging of SMD activity	<i>lite-1</i> (ce314); <i>mzmEx882</i>	<i>Punc-7S::CreVDH</i> (pHK248) - 100ng/uL <i>Pflp-22::DIO-mCherry</i> (pHK246) - 50ng/uL <i>Pflp-22::DIO-GCaMP6Fopt</i> (pHK247, codon-optimized and with introns) - 30ng/uL	<i>Pflp-22</i> (Kim and Li 2004) ; a gift from Dr. Kyuhyung Kim <i>CreVDH</i> (Ruijtenberg and van den Heuvel 2015) <i>DIO</i> (Sohal et al. 2009)

ZIM2122	Freely-moving imaging of SMD activity, AIB inhibition	<i>lite-1</i> (<i>ce314</i>); <i>mzmEx1268</i> ; <i>mzmEx882</i>	<i>Pinx-1::hisCl</i> (pHK307) - 50ng/uL <i>Pflp-17::mCherry</i> (MZ39) - 1.5ng/uL <i>Punc-7S::CreVDH</i> (pHK248) - 100ng/uL <i>Pflp-22::DIO-mCherry</i> (pHK246) - 50ng/uL <i>Pflp-22::DIO-GCaMP6Fopt</i> (pHK247, codon-optimized and with introns) - 30ng/uL	<i>CreVDH</i> (Ruijtenberg and van den Heuvel 2015) <i>Pflp-22</i> (Kim and Li 2004) ; a gift from Dr. Kyuhyung Kim <i>DIO</i> (Sohal et al. 2009)
ZIM2105	Freely-moving imaging of SMD activity in tyramine synthesis mutants	<i>lite-1</i> (<i>ce314</i>); <i>tdc-1</i> (<i>n3419</i>); <i>mzmEx882</i>	<i>Punc-7S::CreVDH</i> (pHK248) - 100ng/uL <i>Pflp-22::DIO-mCherry</i> (pHK246) - 50ng/uL <i>Pflp-22::DIO-GCaMP6Fopt</i> (pHK247) - 30ng/uL	<i>CreVDH</i> (Ruijtenberg and van den Heuvel 2015) <i>Pflp-22</i> (Kim and Li 2004) ; a gift from Dr. Kyuhyung Kim <i>DIO</i> (Sohal et al. 2009) <i>tdc-1</i> (Alkema et al. 2005)
ZIM2106	Freely-moving imaging of SMD activity in tyramine receptor mutants	<i>lite-1</i> (<i>ce314</i>); <i>lgc-55</i> (<i>n4331</i>); <i>mzmEx882</i>	<i>Punc-7S::CreVDH</i> (pHK248) - 100ng/uL <i>Pflp-22::DIO-mCherry</i> (pHK246) - 50ng/uL <i>Pflp-22::DIO-GCaMP6Fopt</i> (pHK247) - 30ng/uL	<i>CreVDH</i> (Ruijtenberg and van den Heuvel 2015) <i>Pflp-22</i> (Kim and Li 2004) ; a gift from Dr. Kyuhyung Kim <i>DIO</i> (Sohal et al. 2009) <i>lgc-55</i> (Ringstad, Abe, and Horvitz 2009)
ZIM2060	Whole-nervous-system imaging with pharyngeal and body wall muscle inhibition (<i>myo-2::hisCl</i> ; <i>myo-3::hisCl</i>)	<i>lite-1</i> (<i>ce314</i>); <i>mzmEx496</i> ; <i>mzmIs38</i> ; <i>mzmEx877</i> ; <i>mzmIs52</i>	<i>Pmyo-2::HisCl::SL2::mCherry</i> (pRL125) - 10 ng/uL <i>Pmyo-3::HisCl</i> (pRL140) - 20ng/uL ; <i>Punc-31::NLSGCaMP6f</i> (pTS100, codon-optimized and with introns) – linearized, 2.5ng/uL <i>Pnlr-1(-150;-1)::HisCl::SL2::mCherry</i> (pAN30) – linearized, 0.5ng/uL <i>Punc-122::dsred</i> – linearized, 4ng/uL	<i>Pnlr-1</i> (Gendrel, Atlas, and Hobert 2016; Haklai-Topper et al. 2011) ; a gift from Drs. Marie Gendrel and Oliver Hobert
ZIM2206	Whole-brain imaging of <i>unc-7 unc-9</i> mutants	<i>lite-1</i> (<i>ce314</i>); <i>unc-7</i> (<i>e5</i>); <i>unc-9</i> (<i>e101</i>); <i>mzmIs52</i>	<i>Punc-31::NLSGCaMP6f</i> (pTS100, codon-optimized and with introns) – linearized, 2.5ng/uL	<i>unc-7</i> (<i>e5</i>) (T. A. Starich et al. 2009); <i>unc-9</i> (<i>e101</i>) ((T. A. Starich et al. 2009); personal evidence Huiyan Huang)
ZIM1428	Whole-brain imaging of <i>unc-7 unc-9</i> mutants (control)	<i>lite-1</i> (<i>ce314</i>); <i>mzmIs52</i>	<i>Punc-31::NLSGCaMP6f</i> (pTS100, codon-optimized and with introns) – linearized, 2.5ng/uL	
ZIM2352	Whole-brain imaging of	<i>lite-1</i> (<i>ce314</i>); <i>unc-9</i> (<i>e101</i>);	<i>Punc-31::NLSGCaMP6f</i> (pTS100, codon-optimized and with introns) – linearized, 2.5ng/uL	<i>unc-9</i> (<i>e101</i>) ((T. A. Starich et al. 2009); personal evidence Huiyan Huang)

	<i>unc-9</i> mutants	<i>mzmEx877</i> ; <i>mzmIs52</i>	<i>Pnlr-1(-150;-1)::HisCl::SL2::mCherry</i> (pAN30) – linearized, 0.5ng/uL <i>Punc-122::dsred</i> – linearized, 4ng/uL	<i>Pnlr-1</i> (Gendrel, Atlas, and Hobert 2016; Haklai-Topper et al. 2011) ; a gift from Drs. Marie Gendrel and Oliver Hobert
ZIM2297	Whole-brain imaging of <i>acc-1</i> mutants	<i>lite-1</i> (<i>ce314</i>); <i>acc-1</i> (<i>tm3268</i>); <i>mzmEx877</i> ; <i>mzmIs52</i> ;	<i>Punc-31::NLSGCaMP6f</i> (pTS100, codon-optimized and with introns) – linearized, 2.5ng/uL <i>Pnlr-1(-150;-1)::HisCl::SL2::mCherry</i> (pAN30) – linearized, 0.5ng/uL <i>Punc-122::dsred</i> – linearized, 4ng/uL	<i>acc-1</i> (<i>tm3268</i>) (<i>C. elegans</i> Deletion Mutant Consortium 2012; Wever, Farrington, and Dent 2015); <i>Pnlr-1</i> (Gendrel, Atlas, and Hobert 2016; Haklai-Topper et al. 2011) ; a gift from Drs. Marie Gendrel and Oliver Hobert
ZIM2317	Whole-brain imaging of <i>lgc-47</i> mutants	<i>lite-1</i> (<i>ce314</i>); <i>lgc-47</i> (<i>ok2963</i>); <i>mzmEx877</i> ; <i>mzmIs52</i>	<i>Punc-31::NLSGCaMP6f</i> (pTS100, codon-optimized and with introns) – linearized, 2.5ng/uL <i>Pnlr-1(-150;-1)::HisCl::SL2::mCherry</i> (pAN30) – linearized, 0.5ng/uL <i>Punc-122::dsred</i> – linearized, 4ng/uL	<i>lgc-47</i> (<i>ok2963</i>) (<i>C. elegans</i> Deletion Mutant Consortium 2012; Wever, Farrington, and Dent 2015);
ZIM2314	Whole-brain imaging of <i>acc-1</i> <i>lgc-47</i> mutants	<i>lite-1</i> (<i>ce314</i>); <i>acc-1</i> (<i>tm3268</i>); <i>lgc-47</i> (<i>ok2963</i>); <i>mzmEx877</i> ; <i>mzmIs52</i>	<i>Punc-31::NLSGCaMP6f</i> (pTS100, codon-optimized and with introns) – linearized, 2.5ng/uL <i>Pnlr-1(-150;-1)::HisCl::SL2::mCherry</i> (pAN30) – linearized, 0.5ng/uL <i>Punc-122::dsred</i> – linearized, 4ng/uL	<i>acc-1</i> (<i>tm3268</i>) (<i>C. elegans</i> Deletion Mutant Consortium 2012; Wever, Farrington, and Dent 2015); <i>lgc-47</i> (<i>ok2963</i>) (<i>C. elegans</i> Deletion Mutant Consortium 2012; Wever, Farrington, and Dent 2015); <i>Pnlr-1</i> (Gendrel, Atlas, and Hobert 2016; Haklai-Topper et al. 2011) ; a gift from Drs. Marie Gendrel and Oliver Hobert
ZIM2310	Whole-brain imaging, RIB inhibition	<i>lite-1</i> (<i>ce314</i>); <i>mzmEx1333</i> ; <i>mzmEx877</i> <i>MzmIs52</i> ;	<i>Psto-3::hisCl::mCherry</i> (pHK170) - 5ng/uL <i>Pflp-17::mCherry</i> (pMZ39) - 5ng/uL <i>Punc-31::NLSGCaMP6f</i> (pTS100, codon-optimized and with introns) – linearized, 2.5ng/uL <i>Pnlr-1(-150;-1)::HisCl::SL2::mCherry</i> (pAN30) – linearized, 0.5ng/uL <i>Punc-122::dsred</i> – linearized, 4ng/uL	<i>Psto-3</i> (Kato et al. 2015) <i>Pnlr-1</i> (Gendrel, Atlas, and Hobert 2016; Haklai-Topper et al. 2011) ; a gift from Drs. Marie Gendrel and Oliver Hobert

6.2. Population behavior assays

Behavior assays (Fig. 4.14, 4.15, 4.16) were performed as described previously (Kaplan et al. 2020). Approximately 20 young adult worms (containing 0 to 1 row of eggs) were picked onto an NGM plate without food, then onto 1mL S-basal buffer to remove food from their bodies, and again picked onto a 15cm assay plate (also without food). Prior to picking onto the assay plates, worms were incubated for 30-45min on NGM agar plates with either 20mM histamine (+His; histamine dihydrochloride, Sigma-Aldrich) or an equal volume of water (-His). These plates were seeded with OP50, which take up histamine from the NGM agar; the histamine-containing bacteria is then consumed by the animals. OP50 was seeded across the entire plate surface to enhance histamine uptake. Recordings were performed on +His and -His (Ctrl) assay plates. In the assay plate, a Whatman paper soaked with 20mM CuCl_2 was used to repel worms from the plate borders, resulting in a 36mm x 36mm arena. Constant gas flow of 21% O_2 was delivered using a custom transparent plexiglass device (25mL/min) of 39mm x 39mm x 0.7mm, which was placed on top of the arena (Hums et al. 2016). Gas flow was delivered using a static gas mixer connected to mass flow controllers (Vögtlin Instruments), managed by custom LabVIEW scripts (National Instruments). Gas mixtures were balanced with 79% N_2 to achieve constant gas flow. Sensory responses were examined in off-food assays by switching from 21% O_2 to 4% O_2 . Worms were set to acclimate for 5 minutes prior to recordings at a constant gas flow of 21% O_2 . Behavior arenas were illuminated with red LEDs and recorded at 10fps using 5 megapixel CMOS cameras (Teledyne DALSA), yielding a pixel resolution of 0.0129 mm/pixel.

Movie analysis and behavior detection was achieved using MATLAB-based (Mathworks) custom image processing and tracking code described previously (Ramot et al. 2008; Hums et al. 2016; Kaplan et al. 2020). Briefly, worm shapes and their centroids were detected using grey level thresholding. Their trajectories were calculated by connecting nearby centroid coordinates in adjacent frames and then used for quantifying speed, angular speed and reversal metrics. Bend angles were measured by analyzing these worm images as described in (Hums et al. 2016). Briefly, worm images were binarized and then skeletonized to produce splines that trace the worm midline. Splines were smoothed and segmented into 25 equally spaced body segments. For each frame in each worm's trajectory, angles between adjacent body segments were measured to produce 24 angle measurements. Head and tail positions were determined using the direction of centroid movement. Lastly, in experiments where manipulations resulted in a loss of movement, we excluded time-averaged background subtraction prior to gray level thresholding, and assigned head position manually. Because ventral and dorsal were not distinguishable in these recordings, angle signs were assigned randomly. Therefore, panels where we distinguish between ventral and dorsal were made using higher-resolution recordings acquired along with Ca^{2+} imaging (Fig. 4.18).

6.3. Ca²⁺ imaging in immobilized animals

Performed as described in (Kaplan 2020). Whole-brain and whole-nervous-system Ca²⁺ imaging experiments were performed using transgenic, young adult *C. elegans*, one day after larval L4 stage, containing 0-10 eggs. Neuronal activity was visualized by expressing nuclear-localized, genetically encoded calcium indicator NLS-GCaMP6f; pan-neuronal expression was achieved using the *Punc-31* promoter (T.-W. Chen et al. 2013). Neuronal activity was recorded as previously described (see (Kato et al. 2015)), with following modifications. We found that forward command states sometimes terminate in quiescence periods (Kato et al. 2015; Nichols et al. 2017); this study focused on behaviors and neuronal activities occurring during forward command states. Thus, to increase the occurrence of forward command states in immobilized recordings, we expressed hisCl, the *Drosophila* histamine-gated chloride channel (Pokala et al. 2014) in quiescence-promoting neuron RIS (Turek, Lewandrowski, and Bringmann 2013; Nichols et al. 2017) using the Pnlr-1 promoter (Haklai-Topper et al. 2011; Gendrel, Atlas, and Hobert 2016) in all whole-brain and whole-nervous-system experiments except for *unc-7 unc-9* mutant imaging experiments (Fig. 4.20, 4.21, 4.22).

In SMD inhibition experiments, the SMDs were silenced by cell-class-specific expression of hisCl using a Cre-lox strategy; we expressed Cre using the *Punc-7S* promoter and the *Pflp-22* promoter was used to express the *HisCl::SL2::mCherry* construct in a double inverted open reading frame (DIO) (T. A. Starich et al. 2009; Kim and Li 2004). The mCherry marker co-expressed with hisCl was used to confirm SMD identity and inhibition; worms with a residual SMD activity of over 50% were excluded from immobilized imaging analysis. However, worms with residual SMD activity were not excluded from freely-moving recordings, which may explain residual head-casting in SMD::hisCl animals (Fig. 4.14b). For body motor neuron inhibition experiments, we used the *Punc-17* promoter, which we refer to as VNC_{ACH}, to express hisCl and mCherry in cholinergic motor neuron classes AS, DA, DB, VA, VB in the ventral nerve cord (VNC) (Charlie et al. 2006). The mCherry marker was used to confirm that mCherry-positive neurons in the retrovesicular ganglion (RVG, where DB01 and DB02 nuclei are located) showed little to no activity.

Immobilized Ca²⁺ imaging experiments were performed with custom microfluidic two-layer PDMS devices to control O₂ and to immobilize and laterally align animals, as described previously ((Schrödel et al. 2013; Kato et al. 2015; Kaplan et al. 2020; Uzel, Kato, and Zimmer 2022)), with modifications. In addition to the curve in the worm channel used to align worms laterally (Cáceres et al. 2012), a second curve designed to fit a young adult worm was added. This curve was designed to align and bring closer together the animal's head and tail, therefore reducing the imaging area required to record the activity of all neurons in the *C. elegans* body in the case of whole-nervous-system recordings, but also decreasing the imaging area necessary for simultaneous imaging of the head, tail and several VNC neurons in the whole-brain imaging configuration. This channel also contains a narrowing in order to keep the animal's head in place. A technical drawing of the design can be found in Fig. 4.1a.

The microfluidic device assembly and worm loading procedure has been detailed previously, but the procedure is described next (Zimmer et al. 2009; Hums et al. 2016). The microfluidic device's worm channel was connected to a syringe containing nematode growth medium (NGM) buffer with 1 mM tetramisole and 20 mM histamine (his-tet-NGM) for all experiments, barring following exceptions: *unc-7 unc-9* imaging experiments were performed with only 1 mM tetramisole, no histamine, since these worms did not contain *Pnlr-1::hisCl*; *myo-2::*, *myo-3::hisCl* imaging experiments required only 20 mM histamine, no tetramisole, since these worms were paralyzed through muscle relaxation and not tetramisole paralysis. All components were connected using Tygon tubing (0.02 in ID, 0.06 in OD; Norton) and 23G Luer-stub adapters (Intramedic). Constant gas delivery (21% O₂, flow rate of 50ml/min) was achieved using a gas mixer attached to mass flow controllers (Vögtling Instruments) that mixed oxygen and nitrogen from pressurized gas tanks, using LabView software. Immobilized Ca²⁺ imaging experiments were done with well-fed, young adult *C. elegans* worms (0-10 eggs). In the case of worms with hisCl transgenes, they were transferred onto NGM agar plates seeded with OP50 *E. coli* mixed with 20 mM histamine to feed on for 30-45 minutes. Then, all animals were transferred into a drop of buffer on a food-free NGM agar plate and then onto a second NGM plate with buffer, to rid them of bacteria covering the body. Individual animals were loaded onto the microfluidic device by manually applying a vacuum with the syringe to suck up individual animals into Tygon tubing; this tubing was then reconnected to the worm inlet and the worm was pushed into the microfluidic device and arranged in the curved channel.

The fluorescence values were recorded 5-10 minutes after loading; the illumination and piezo stage were switched on 2-3 minutes before acquisition start. Animals were imaged at 21% O₂ for 30 minutes for all experiments except for the *unc-7 unc-9* imaging dataset, where worms were imaged for 18 minutes. High-resolution data of neuronal activity in the head ganglia (whole-brain recordings) was acquired with two different setups: an inverted UltraViewVoX spinning disk confocal microscope (PerkinElmer) using an EMCCD camera (C9100-13, Hamamatsu) and a 40x 1.3 NA EC Plan-Neofluar oil-immersion objective (Zeiss); and an inverted Axio Observer.Z1 (Zeiss) with attached CSU-X1 spinning disk (Yokogawa) and a Piezo stage (P-736 PI nano, Physik Instrumente GmbH), using an EMCCD camera (Photometrics Evolve 512) and a 40x 1.2 LD LCI Plan- Apochromat water-immersion objective (Zeiss) with Visiview software (Visitron Systems GmbH). The volume spanning the animals' head ganglia was recorded in 13-18 2 μm z-planes, each illuminated for 10ms or 20ms to record GCaMP6f fluorescence, resulting in acquisition rates of 1.55 - 3.07 volumes/sec.

Whole-nervous system neuronal activity of tetramisole-paralyzed animals was recorded using an inverted fluorescence microscope (Observer Z1, Zeiss) with a 25x 0.8 NA LCI Plan-Neofluar multi-immersion objective (Zeiss) and recorded with a scientific complementary metal-oxide-semiconductor (sCMOS) camera (pco.edge 4.2, PCO) using Visiview software (Visitron Systems). To record the entire nervous system, 30 1 μm z-planes were illuminated each for 10 ms, yielding an acquisition rate of 3.0303 volumes/sec. We used a deconvolution algorithm (classic maximum likelihood estimation)

using Huygens software to increase the contrast and resolution of the image data in the tetramisole paralysis, immobilized whole-nervous-system recordings exclusively, with following specifications: signal/noise ratio, 8; automatic background estimation; 40 iterations; 0.1 quality change stopping criterion. After deconvolution, the neuronal activity traces extracted from the deconvolved, whole-nervous-system recordings from tetramisole-paralyzed animals were compared to high-resolution whole-brain recordings acquired with spinning disk confocal microscopy in order to assess the quality of the whole-nervous-system data. This ‘ground truth’ comparison ensured that the deconvolution procedure did not introduce artifacts. Head-tail multi neuron imaging and all imaging in freely moving animals did not include image deconvolution post processing steps. Importantly, deconvolution was performed only for whole-nervous-system recordings in immobilized worms paralyzed with tetramisole because a standard spinning disk confocal microscope (Yokogawa CSU-X1 scanning head) did not provide the needed field of view.

Ca²⁺ imaging of whole-nervous-system activity in *myo-2::*, *myo-3::hisCl*-paralyzed animals was achieved in confocal resolution thanks to the installation of a 0.5x demagnification optical lens set (Achromat 200mm focal length and Achromat 100mm focal length) in the confocal imaging setup of the Zimmer lab (inverted Axio Observer.Z1 (Zeiss) with attached CSU-X1 spinning disk (Yokogawa) with Visiview software (Visitron Systems GmbH)). Prior to imaging, young adult, *myo-2::*, *myo-3::hisCl* transgenic animals (6-10 eggs) were transferred onto NGM agar plates seeded with OP50 *E. coli* mixed with 20 mM histamine to feed on for 30-60 minutes. We used a 25x 0.8 NA LCI Plan-Neofluar multi-immersion (water) objective (Zeiss) and recorded 2 μm z-planes illuminated with 20% laser power for 20 ms per plane, with a scientific complementary metal-oxide-semiconductor (sCMOS) camera (pco.edge 4.2, PCO), resulting in an acquisition rate of 2.94 volumes/sec. The inclusion of all neurons in the *C. elegans* head, tail and body was achieved with the use of microfluidic devices bonded onto circular dishes, which were positioned such that the worm body would lie diagonally across the field of view. The worm images were rotated to a horizontal orientation with the linear interpolation algorithm in Visiview (Visitron Systems GmbH)

6.4. Simultaneous imaging of neuronal activity and behavior

Performed as described in (Kaplan et al. 2020). Freely-moving imaging of neuronal activity and behavior was performed on young adult animals (0-6 eggs) expressing mCherry and GCaMP6f in SMD or DB02 neurons, as follows: worms were picked onto a foodless NGM agar plate, then, a ~40mm x 40mm area was cut around the worm; this chunk of agar was removed from the plate and covered with a coverglass (45mm x 50mm #1.5) to constrain the worm’s movement to 2D, as detailed in (Collins and Koelle 2013). This ‘coverglass-agar sandwich’ configuration leads to slower worm movement but qualitatively normal body shapes and behavior. The setup was then placed into a motorized stage with an associated controller (MS-2000-PhotoTrack, Applied Scientific Instrumentation). The worms were

allowed to acclimate for 5 minutes (including at least 2min excitation light exposure) and individually recorded for 8 minutes thereafter. Fluorescence images were acquired using an Axio Observer.Z1 inverted compound microscope (Zeiss) with two Evolve 512 Charge-Coupled Device cameras (Photometrics). A CoolLED pE-2 excitation system was used for dual wavelength excitation light generation (470 and 585 nm) with an ET-EGFP/mCherry filter set (59022x, Chroma) and dichroic (59022bs, Chroma). A 63x, 1.4 NA, Plan-Apochromat, oil-immersion objective (Zeiss) was used to stream unbinned single-plane fluorescence images at 33ms exposure time, with Visiview software (Visitron Systems GmbH), yielding an imaging frame rate of ~30Hz. Stable GCaMP expression specifically to neurons of interest (and few others) was achieved using sparse drivers. This was necessary for the unambiguous identification of specific neurons of interest and the subsequent extraction of their neuronal signals. The neuron(s) of interest were tracked in space and re-centered onto the objective using the system described in (Faumont, Lindsay, and Lockery 2012). Briefly, mCherry signals were used to center the neurons of interest as the animal moved through the agar. A dichroic mirror (620 spxr, Chroma) relayed the high-wavelength portion of the mCherry emission to a four-quadrant photomultiplier tube (Hamamatsu). The remaining emission light was split by a DualCam DC2 cube (565 lpxr, Photometrics) in mCherry signals (641/75nm, Brightline) and GCaMP signals (520/35nm, Brightline), and imaged by each CCD camera. Simultaneously, the worm's behavior was recorded under infrared illumination (780nm) using a Manta Prosilica GigE CCD camera (Applied Vision Technologies) at 4x magnification and 100ms exposure time. Approximately 8 minutes of data were acquired for each animal.

6.5 Neuronal time series extraction from immobilized pan-neuronal imaging experiments

Performed as described in (Kaplan et al. 2020). As described in (Kato et al. 2015), neuronal activity traces were obtained by tracking the intensity maxima in each volume over time and calculating the single-cell fluorescence intensities (F). F_0 was calculated as the mean fluorescence intensity across the trial. F/F_0 was calculated after background subtraction, for each neuron. For selected recordings showing an increased amount of bleaching, said bleaching was corrected for by detrending $\Delta F/F_0$ neural traces in a two-step procedure. This posterior detrending step gave qualitatively better results compared to the previously described method (Kato et al. 2015). The detrending went as described in (Kaplan et al. 2020): We performed an exponential fit to each trace, followed by fitting a single exponential function to peaks detected at the beginning and the end of the neural traces. This second step was aimed as a bleach-correction step (referred to as detrending), but it occasionally over-corrected the activity traces drastically, such that they were distorted in a small number of instances. Thus, we calculated the relative change in variance of each trace after the second detrending step ($\text{var}(\text{post-detrending}) - \text{var}(\text{pre-detrending}) / \text{var}(\text{pre-detrending})$) as a measure of distortion. We observed that the distribution of these measures across all neurons exhibited a long tail (not shown); we determined a relative change

of 8 as a cutoff for distorted traces. Neural activity traces with a variance change above the cutoff amounted to 3.31% of the neuronal traces analyzed; for these traces, we resorted to the (pre-detrending) single bleach-corrected version of the trace.

6.6 Neuronal identification (pan-neuronal imaging)

Performed as described in (Kaplan et al. 2020). In whole-brain Ca^{2+} imaging data, the activity of 113-129 neurons was detected in the head ganglia, which corresponds to 49.7 - 66.15% of expected neurons. The rest likely were constitutively inactive and thus showed very low fluorescence levels, or had to be excluded because of artifacts or the inability to separate the activities of very close-by neurons. Further, we cannot rule out that the transgene is not expressed in a small fraction of neurons. In whole-nervous system Ca^{2+} imaging data, 103-129 neurons were detected across the whole body (39.4 - 42.7%) in tetramisole-paralyzed worms, while 194-227 neurons were detected in *myo-2::*, *myo-3::hisCl* worms (64.2 - 75.2%). This discrepancy probably arises from the fact that *myo-2::*, *myo-3::hisCl* worms were imaged using a spinning disk confocal setup, profiting from much better resolution than widefield fluorescence microscopy.

The identification of neurons was done according to their activity patterns, anatomical location (www.wormatlas.org) and lab knowledge gathered with red fluorophore expression in specific marker lines reported in previous studies (Kato et al. 2015; Nichols et al. 2017; Skora, Mende, and Zimmer 2018), as well as recently with NeuroPAL (Uzel, Kato, and Zimmer 2022). We identified the SMD neurons by driving worm codon-optimized mCherry (wCherry) expression with the *Pflp-22* and *Punc-7s* promoters (Kawano et al. 2011). We were thus able to disambiguate the uncertainty regarding the cell class identity of these neurons that had been reported in previous studies (SMDD vs. SMB or RMF) (Schrödel et al. 2013; Kato et al. 2015). We identified the B-MNs along the VNC using the *Pacr-5* promoter to express wCherry (Winnier et al. 1999). Pre-anal ganglion neuron PDA was identified with Cre-lox, using the *Pflp-7* and *Pnmur-1* promoters (Kim and Li 2004; Maier et al. 2010). In certain cases, we reliably observed activity patterns in distinct locations, but could not be assign neuronal identities unambiguously; we denoted these cases as # and their neuronal identities and possible alternatives are shown in brackets: URY (URA, IL1), RMD (SAA, RIA, SIB, RIH), SIB (SIA, RMD, RMH).

B-MNs were identified by a combination of position, activity, and specific marker line information. Regarding the B-MNs in the retrovesicular ganglion (RVG), we consistently observed four neurons with heightened activity during forward command states; we labeled the most anterior one VB02 and the most posterior neuron DB01, consistent with previous IDs (www.wormatlas.org). One of the remaining two neurons showed activity patterns like DB01 and VB02 (i.e. slow rises following the fall of AVA activity and activity plateaus throughout forward command states); the fourth neuron showed more spike-like, unpredictable activity transients or peaks. The remaining potential B-MN IDs were DB02 and VB01. To disambiguate, we used *Pceh-12::mCherry* to label VB neurons (S. E. Von

Stetina et al. 2007) and recorded an immobilized, whole-brain imaging dataset and found that the spike-like neuron is VB01 and the former neuron is therefore DB02. The other B-MNs are reported to form a specific pattern along the VNC: DB03 and VB04 are posterior to the RVG and separated by cell bodies of other neuron classes, and posterior to VB04 is a repeating pattern of consecutive (i.e. uninterrupted by other cell bodies) VB/DB pairs followed by single VB neurons (2-1-2-1 pattern). We used *Pacr-5::mCherry* to label all B-MNs and their processes and confirmed this, since only DB and not VB neurons have commissures that cross to the dorsal side, making class identification straightforward. These recordings also showed that in the case of VB/DB pairs, the VB neuron is always anterior except for the most posterior pair, DB07 and VB11. In 11/20 animals we observed that DB07 was located anterior to VB11, thus we couldn't establish a relationship between their IDs unambiguously. In whole-nervous-system recordings, we found the expected number of neurons in the expected anatomical pattern showing heightened activity during forward command states. Thus, we could assign IDs to B-MNs except DB07 and VB11; since their positions were not unambiguous, we labeled the anterior neuron of this pair DB07a and the posterior VB11p.

In total, we were able to identify 37-48 neurons in whole-brain, tetramisole paralysis recordings (mean 42.8, std 4.324), 45-53 neurons in whole-nervous-system, tetramisole paralysis recordings (mean 50.4 std 3.715), and 53-59 neurons in whole-nervous-system, hisCl paralysis recordings (mean 55.2 std 2.683).

6.7 Principal Component Analysis (PCA; immobilized pan-neuronal imaging)

Performed as described in (Kaplan et al. 2020). Previous work from the Zimmer lab has performed PCA on the time derivatives of neuronal activity traces to extract global motor commands dominating the nervous system (Kato et al. 2015; Nichols et al. 2017; Skora, Mende, and Zimmer 2018). However, studies in freely-moving worms revealed that some behavioral parameters, like motor state and turning strength, are better decoded by the neuron's original Ca^{2+} activity trace rather than its time derivative (Kato et al. 2015). Thus, in this study, in a departure from previous work, we have modified the previous PCA method to now include both neuronal activity traces and their derivatives. We believe that this modification makes the PCA procedure less biased, because we include both instantaneous Ca^{2+} -levels (original activity trace) and the dynamics of the neuron over time (time derivative). This method results in each neuron being represented by two variables, where each recording frame is one observation. First, we detrended the neuronal activity traces, as detailed in section 6.5, and then calculated the time derivatives of the detrended $\Delta F/F_0$ using the total variation regularized differentiation method (Chartrand 2011). In order for the activity traces and their time derivatives to have equal variance, the neural traces were then normalized. We performed PCA on the detrended $\Delta F/F_0$ neural traces together with their time derivatives using the MATLAB (Mathworks) `pca` function, which also calculated variance explained for each PC. A 10-sample sliding average filter was applied to the

PCA-phase plot trajectories for visualization purposes. Phase plot trajectories were colored according to command states similarly to what has been described previously (Kato et al. 2015). In short, the activities of three key neurons—AVA, SMDD and SMDV—were used to assign behavior state commands to population neuronal activity. For this, RISE, HIGH, FALL and LOW phases were identified in the time derivatives of the neurons' activity traces, as follows: RISE and FALL phases were defined as time points when their time derivative was greater than a small positive threshold or smaller than a negative threshold, respectively. The remaining time points were assigned to HIGH and LOW phases based on behavioral state order and a threshold. The time points in the phase plot trajectory were then colored by AVA phase exclusively, where AVA rise and high are defined as reversal, AVA fall as a post-reversal turn, and AVA low as forward command (Fig. 4.2, Fig.4.3 Fig. 4.10, Fig. 4.26). Note that AVA falls were coupled to either SMDV or SMDD rises and these were mutually exclusive in 100% of all detected AVA falls in wildtype animals (Fig. 4.24c).

For Figs. 4.3, the neuronal traces from whole-nervous-system Ca^{2+} imaging (tetramisole-paralysed) animals were divided into neuronal subsets for subsequent PCA analysis. These were categorized as interneurons, motor neurons or other neurons. For the inter neuron category, identified interneurons in the head and tail regions, as well as unidentified neurons located in the tail ganglion were included; for the motor neuron category, identified motor neurons innervating the muscles in the head and neck, all neurons located in the VNC, as well as unidentified neurons located in the pre-anal ganglion (PAG) were included. All other neurons not belonging to these two subsets, like amphid sensory neurons, were categorized as "other neurons". After categorization, PCA was performed as described above. This categorization was also used for assessing the reconstruction quality for neuronal subsets in Fig. 4.4 (see section 6.10.9) .

6.8 Neuronal time series extraction and behavior analysis (freely moving imaging)

GCaMP and mCherry signals from behaving worms were acquired at 30 Hz, and the mCherry signal was used for tracking position of the nucleus or cell body of interest over time, using Metamorph software (Molecular Devices). Then, these coordinates of the tracked regions were used to extract the average of the 50 brightest pixels, using custom MATLAB code (Mathworks). Background subtraction was performed using one background measurement close to the tracked neuron, from the first frame for each channel. The GCaMP/mCherry ratio, termed "R", was used to calculate an R_0 value, the average of the lowest 10% of the R values. R/R_0 was then calculated as $(R - R_0) / R_0$. For subsequent analyses, peaks were detected as detailed in section 6.10. Data were further normalized by the 95th percentile in each recording for Fig. 4.17b and Fig. 4.24b. We manually identified reversals by inspecting infrared behavior movies, all time points not categorized as reversals were considered forward states. For subsequent skeletonization, a binary worm image was extracted from each frame using custom MATLAB scripts (Mathworks) that employed a combination of edge detection and gray level

thresholding, as described in (Hums et al. 2016). These binarized images were then used to quantify 24 angle measurements, which were linearly interpolated to match the 30 Hz Ca^{2+} recording and manually checked for correct ventral/dorsal assignment.

6.9 Propagation analysis and head-bend type classification (behavior assays and freely moving imaging)

For this study, only forward states were analyzed. Kymograms from either population behavior assays or simultaneous Ca^{2+} imaging and behavior experiments were smoothed and gaps $< 1\text{s}$ were filled by linear interpolation in the case of poor skeletonization. For each angle timeseries, local maxima and minima were detected using a parameter delta (see section 6.10 for a detailed explanation of peak detection and the delta parameter). Each angle timeseries was transformed into an “angle peak timeseries” where each frame was categorized as a maximum ($= 1$), a minimum ($= -1$), or neither ($= 0$). This resulted in a matrix of all angle peak timeseries, or “peak kymogram”, of the same size as the original kymogram, which was analyzed to determine head-bend propagation as follows. Peaks in the second angle were initially defined as head-bends. Head-bends were then analyzed in temporal order; for each head-bend (angle #2 peak), if the previous peak in angle #1 (i.e. backward or simultaneous in time) is of the same sign as the current head-bend (maximum, $= 1$, or minimum, $= -1$), and hasn't been assigned to a previous head-bend, then that peak is assigned to the current head-bend. Similarly, if the next peak in angle #3 is of the same sign as the current head-bend, and hasn't been assigned to a previous-head-bend, then that peak is assigned to the current head-bend. This process is iterated posteriorly until the final angle or until the propagation is terminated. The head-bend is terminated if the next peak is of the opposite sign as the current head-bend. If the next posterior peak (a) occurs $>10\text{s}$ following the previous peak and/or (b) occurs following at least two unassigned peaks in the previous angle, the head-bend propagation is terminated. In both of these cases, the head-bend is whose final propagation angle was less than or equal to angle #13 were categorized as a head-cast. If the final propagation angle was greater than angle #13, the head-bend is categorized as a propagated-bend. Reversals and missing data also terminated the head-bend, in which case, the head-bend was assigned as a propagated-bend if the final propagation angle is greater than #13, but discarded as ambiguous if less than angle #14. Unconnected head-bends were also discarded. For further details please refer to (Kaplan et al. 2020).

6.10 Quantifications and statistical analyses

All quantifications were performed using custom MATLAB (Mathworks) code, except for the coincident peak categorization of *acc-1* mutant whole-brain imaging, which was done manually (see below). Standard statistical tests were done using Graphpad Prism 7. Specifications of which statistical

test was performed, along with the value of n and what n represents, are reported in the figure legends. Additional tests are described in the following sections.

6.10.1 Command state identification and quantification of command state durations (immobilized pan-neuronal imaging)

Performed as described in (Kaplan et al. 2020). Reverse and forward command states were inferred from the activity of interneuron AVA, as previously described (Kato et al. 2015). Shortly, timepoints of rising Ca^{2+} transients and high intensity Ca^{2+} signals were defined as reversal command states. Timepoints of falling Ca^{2+} transients and low intensity AVA Ca^{2+} signals were defined as forward command states. This was the case for all immobilized imaging datasets where the animal's quiescence-promoting neuron RIS was inhibited through RIS::hisCl, as RIS activity periods (and therefore quiescence periods) occur during AVA low states, making a categorization of AVA low states as forward command periods valid only if RIS was inhibited. *unc-7 unc-9* mutants and the corresponding control animals did not contain the RIS::hisCl transgene; for these immobilized imaging experiments, RISE, HIGH, FALL and LOW phases were identified in the RIS time derivatives, and all timepoints of rising and falling RIS Ca^{2+} transients and high intensity RIS Ca^{2+} signals were excluded from forward command states. Forward and reversal command states were quantified as the mean of all command state durations per animal (Figs. 4.20, 4.25, 4.34, 4.35), except for cumulative distribution plots (Figs. 4.25c, 4.32, 4.34b, 4.35e).

6.10.2 Mean activity difference quantification

Performed as described in (Kaplan et al. 2020). We assessed whether neuronal activity levels are modulated by the forward/reverse command state by calculating, for each neuron, the mean $\Delta F/F_0$ of the Ca^{2+} imaging activity traces in all forward command states, the mean $\Delta F/F_0$ of the Ca^{2+} imaging activity traces in all reverse command states, and calculated the difference (Fig. 4.5). As for the peak frequency quantification (see below), only neurons identified in at least three recordings were taken into account. Significant differences between a neuron's mean activity levels in the forward vs. reverse command states were determined with a paired T-test (p-values reported in Table 4.1).

6.10.3 Peak frequency quantification (immobilized pan-neuronal imaging and freely moving imaging)

We noticed that the distribution of forward command state durations was bimodal (data not shown); and very short forward command states rarely allowed for more than one fluctuation per state. Thus, we set a cutoff value of 50 seconds to exclude forward command states shorter than 50 seconds in order to avoid a bias in our analysis because of lack of data. This cutoff was used for all frequency quantifications. The following peak detection method was used to quantify neuronal activity data shown in Figures 4.7-4.9, 4.11-4.13, 4.17, 4.19, 4.22, 4.23, 4.24, 4.28-4.29, 4.31-4.33, 4.35-4.36. For Figures

4.7-4.9, 4.12-4.13 only, peaks were detected on derivative timeseries, for all other figures mentioned above, peaks were detected on the neuronal activity traces. Peak detection and frequency quantification were performed as described in (Kaplan et al. 2020). Briefly: The smoothed time derivatives of neuronal activity traces were calculated with the total variation regularized differentiation method (Chartrand 2011). For all peak detections, derivative and non-derivative, we took the following approach. Local maxima and local minima were detected for each trace as follows:

A maximum peak was defined as a maximal value that had been preceded by a minimum value and followed by a minimum value; there had to be an amplitude difference between the minima and the maximum of at least δ , a key parameter. The δ value was determined automatically by first performing peak detection on the neuronal trace with a wide range of δ s (spanning from too liberal, which detect many false positives due to detection of noise, to too conservative, which fails to detect large amplitude peaks). Then, the number of peaks detected was plotted as a function of δ ; the shape of this plot often resembles a piecewise linear function of two parts, with a high slope at low δ values (many false positives) and a low slope at high δ values (many false negatives). Therefore, the slope of the curve at high δ values is much closer to 0 than at low δ values. We determined the change point between these using the MATLAB (Mathworks) function *findchangepts*, with the 'linear' option; this outputs the index of the curve at which both the mean and slope change most abruptly and thereby the optimal δ parameter. We found that a single range of δ s to look for the optimal change point works well for all data in a particular noise (e.g. sampling rate, degree of smoothing) and amplitude (e.g. derivative or non-derivative) regime. We used a different δ range for different types of datasets, as follows. For peak detection on derivatives from immobilized worm recordings (Figs. 4.7-4.9, Figs. 4.12-4.13), the δ range went from 10^{-4} to 0.03 in steps of 5×10^{-5} . For peak detection on raw traces of immobilized worm recordings at 1.5-3 Hz (Fig. 4.17c, Fig. 4.19c), the δ range went from 0.001 to 0.5 in steps of 0.001. For peak detection on raw traces of immobilized worm recordings performed with the inverted Axio Observer.Z1 spinning disk confocal setup, (Figs. 4.22-4.23, Figs. 4.31-4.33, Figs. 4.35-4.36), the δ range went from 0.08 to 0.3 in steps of 0.0001, 3% conservative. For peak detection on raw traces of immobilized worm recordings from *unc-9* mutants and controls, a δ range from 0.08 to 2 in steps of 0.005, 20% conservative had to be employed to avoid the detection of noise as peaks. For freely moving imaging recordings (Fig. 4.17b, Fig. 4.19b, Fig. 24b, Fig. 4.28, Fig. 4.29), the δ range went from 0.001 to 1 in steps of 0.001. For detecting peaks across all neurons in brain-wide or nervous-system-wide recordings, peak detection on the derivatives performed better than on raw traces; this required two additional steps: (1) peaks with amplitudes less than 0 were excluded, because these are changes in the slope of a fall rather than rises; (2) the second of two subsequent maxima was only included if the intervening minimum fell below 0. If the intervening minimum did not fall below 0, the two peaks correspond to changes in slope rather than individual calcium peaks, and the second peak was therefore excluded.

Peak frequency quantification and statistical analysis for all identified neurons (pan-neuronal imaging)

Peak frequency quantifications of all neurons within one recording were calculated as follows. As mentioned previously, only neurons that were identified in at least three pan-neuronal imaging recordings were taken into account. For peak frequency quantifications in Fig. 4.7, we tested whether the inter-peak interval distribution between detected peaks was significantly different from random, across all forward (Fig. 4.7a) or reversal command states (Fig. 4.7b), as follows. For each command state, the same number of spike times were randomly selected to accumulate a random inter-peak interval distribution. This procedure was reiterated 10^6 times to obtain an average random distribution. Then, we summed the absolute difference, bin-by-bin, between the average random distribution and the actual inter-peak interval distribution, thereby measuring the magnitude of deviation from random distribution. This measure was also determined for each of the 10^6 resampled distributions. The p-values in Table 4.1 denote the fraction of resampled distributions with at least as large of a deviation from random as the actual distribution. Multiple comparisons correction was performed by determining statistical significance with the Benjamini-Hochberg-Yekutieli procedure (Yekutieli and Benjamini 2001).

Peak frequency quantification for single neurons (pan-neuronal imaging)

Peak frequencies for single neurons were calculated as the number of maximum peaks within each forward command state divided by the duration of each forward command state for each neuron for quantifications shown in Figs. 4.7a,b; 4.12b,d; 4.13b, instances where a neuron was identified but no peaks were detected were counted as zero. For Figs. 4.11, 4.22, 4.23, 4.33, 4.36, frequencies were calculated as the number of maximum peaks occurring within all forward/reversal command states divided by the total time spent in forward/reversal command states.

Since RIB was not fully inhibited in RIB::hisCl recordings, these recordings contained periods of full RIB inhibition and periods of incomplete RIB inhibition, termed ‘RIB low’ and ‘RIB high’, respectively. We quantified SMD peak frequency and amplitude by first detecting forward command states, then categorizing each timepoint within them as ‘RIB low’ if RIB showed no activity and ‘RIB high’ if RIB showed activity. Then, SMD peak frequencies were quantified by counting all SMD peaks during RIB high or RIB low and dividing by the total time spent in RIB high or RIB low states per recording (Fig. 36).

6.10.4 Covariogram analysis (immobilized pan-neuronal imaging)

Covariograms were calculated for all neurons that could be reliably identified across at least three immobilized worm recordings. Covariograms can be thought of as a measure of cross-correlation between sparse signals; they indicate the frequency of peaks of a "target" neuron at different time delays relative to the peaks of a "reference" neuron, relative to chance levels. Covariograms were computed as described in (Brody 1999), but with modifications to correct for the different durations of forward

command states. Here, as well, forward command states shorter than 50s were not analyzed and we used peaks detected as described in section 6.10. Raw cross-correlogram counts were calculated for neuron pairs as follows: as described in (Kaplan et al. 2020), for each peak in the reference neuron (rows in Fig. 4.8 and 4.9), all peaks in the target neuron (columns in Fig. 4.8 and 4.9) during the same forward command state were considered; in 10-second bins, we accumulated the time delays of the target neuron peaks relative to the reference peak were accumulated. This procedure was iterated using all reference peaks within each state, and ultimately accumulated to the full raw cross-correlogram across all forward command states across all recordings. To account for the different command state lengths, these values were then converted to frequencies by dividing them by the number of available data for each bin (i.e. the number of possible frames in each bin in which spikes could have occurred). We computed resampled cross-correlograms by randomly selecting the same number of peak times of the target neuron at each forward state and normalizing them in the same way (resampled 10^6 times). This resampling procedure accounts for co-fluctuations in the frequencies of neuronal activity from trial to trial that may be independent of the spike-time relationships but unintentionally cause peaks in the cross-correlogram (Brody 1999). Lastly, the average of the resampled cross-correlograms were subtracted from the actual raw cross-correlograms to obtain the final covariograms.

We used the actual cross-correlograms and the resampled ones for determining statistical significance. First, we assessed, across all time bins for each correlogram, whether the covariograms represented a positive or a negative relationship, depending on whether the largest absolute value between the maximum or the minimum of each correlogram was the maximum (a positive relationship) or the minimum (a negative relationship, marked with “(-)” in Fig. 4.8). Then, each of the 10^6 resampled distributions were analyzed to determine the probability of finding correlations with absolute values as large as either the maximum or minimum value observed in the actual covariogram (depending on if it was determined a positive or a negative relationship). The p-value reported in Table 4.2 is the fraction of maxima or minima from resampled distributions that are at least as large in absolute value as that obtained from the actual distribution. Multiple comparisons correction was performed by determining statistical significance with the Benjamini-Hochberg-Yekutieli procedure (Yekutieli and Benjamini 2001).

6.10.5 Post-reversal SMD peak identification, amplitude quantification

Post-reversal SMD peaks were found by detecting peaks on both SMDD and SMDV traces and finding SMD peaks immediately following the end of each reversal command. If SMDD peaked first, the post-reversal turn command was categorized as dorsal, those where SMDV peaked first were categorized as ventral. Then, ‘ambiguous’ turn commands were identified as those command states that began with SMDD+SMDV coincident peaks (only for Fig. 4.31). Post-reversal SMD peak amplitudes were calculated as the average of all post-reversal peaks in one recording, for each SMD separately. The relative onset of SMD peaks in dorsal/ventral turn commands (Fig. 4.32) was calculated by finding

the first SMDD and first SMDV peak following each reversal command end, then subtracting the time point when the SMDV peak was detected from the time point when the SMDD peak was detected (for ‘dorsal turn’ commands, Fig. 4.32 left) and vice versa for ‘ventral turn’ commands (Fig. 4.32 right).

6.10.6 Coincident peak categorization and quantification (*acc-1* immobilized imaging)

acc-1 mutant whole-brain imaging recordings were acquired and peak detection was performed as described above. Then, we manually identified ‘coincident peaks’, which were peaks in an SMD trace that occurred simultaneously with peaks in a different SMD trace. Peaks were categorized as ‘coincident’ if the rise of a detected peak in one trace occurred within 10 frames of the rise of a detected peak in the second trace. Due to a mistake in the acquisition procedure, timing information was lost, thus we set the threshold for coincident peaks at 10 frames instead of a threshold in seconds. Then, the proportions of coincident peaks were calculated for all pairs between the 4 SMDs by dividing the number of coincident peaks by the total number of detected peaks of each neuron (Fig. 4.31a). For Fig. 4.31b, only SMDD+SMDV coincident peaks were categorized depending on the motor command state they occurred in, and used to calculate the proportion of coincident peaks for each motor command state.

6.10.7 Triggered averages of SMD activity

After post-reversal turn commands were categorized as dorsal/ ventral/ ambiguous, we extracted SMDD and SMDV activity at reversal command ends (timepoint 0) \pm 10 seconds (time was calculated with theoretical frames/second) and calculated triggered averages of SMD activity. For Figs. 4.24a,c, the triggered average calculation was performed as described above, but with following modifications: we used the measured acquisition frame rate (not the theoretical frame rate), we then interpolated SMD traces to have an equal amount of timepoints.

6.10.8 Cycle period quantifications (immobilized panneuronal and freely moving imaging)

Peaks were detected as described in section 6.10; phases in Fig. 4.19b-c were quantified by linearly interpolating between detected peaks for each half cycle (similar to (Eliav et al. 2018)). Through interpolation, we could calculate the phase of the SMD alternation cycle independently from non-alternating SMD oscillations, as follows. 0 to π was interpolated from the first SMDD peak following an SMDV peak (i.e. SMDD alternating peak) to the first SMDV peak following an SMDD peak, ignoring any intervening SMDD peaks. Similarly, π to 2π was interpolated from the first SMDV peak following an SMDD peak to the first SMDD peak following an SMDV peak, also ignoring any intervening SMDV peaks. Because of this definition, SMDD-only and SMDV-only oscillations were each restricted to half cycles. To best compare to behavioral phase quantifications from (Kaplan et al. 2020), we used the first trough of each SMDD-only or SMDV-only oscillation (i.e. minimum, see Fig.

4.18e, $t \sim 0$ s) to create the histograms, as these corresponded to the first head-cast following a propagated-bend.

6.10.9 Reconstruction quality for neuronal subsets (pan-neuronal imaging)

To assess how well the activity of interneuron and motor neuron pools was captured in the top PC dimensions, we calculated Pearson's linear correlation coefficient between the original activity traces and their derivatives (i.e. the original data), and the reconstructed traces after PCA, for each neuron (Fig. 4.4). These reconstructed traces were calculated through matrix multiplication of the PC coefficients with the PC loadings of the top ($i = 1$ to 5) PCs and then adding the mean of the original data, as follows:

$$Data_{recon} = [PC_{Coeff}^1: PC_{Coeff}^i] \times [PC_{Load}^1: PC_{Load}^i] + \text{mean}(\text{OrigData})$$

To measure how similar reconstructed traces are to their original counterparts, we used the average correlation coefficient for all the traces of a neuronal cell type— interneurons, motor neurons or other neurons (categorization as in section 6.7) — in a recording. This measure is insensitive to the magnitude of neuronal activity traces and was therefore preferred over mean-square-error.

6.10.10 Polar histogram statistics

We tested the significance of the distributions in Fig. 19b-c by resampling. First, we determined the probability of obtaining by chance such a skewed distribution as the distribution from the real data, as follows. For each half-cycle from which the real data had been extracted, we randomly selected one phase and generated a distribution of phases matching in number to the real distribution. Peak detection relied on the parameter delta, thus we restricted the time points that could be selected to those at least delta away from the previous peak, since in timepoints less than delta away it would have been impossible for peaks to be detected. We then binned the data like the real data and quantified the absolute difference, bin-by-bin, between the resampled distribution and the all-phases distribution, which was calculated using the same phases from which the random data was selected. Sample distribution skewness was measured as the total difference between the resampled data and the all-phases distribution, calculated as the sum of all bin-by-bin absolute differences. This procedure was repeated 10^6 times and the skewness of the real distribution was measured the same way. The p-value is the fraction of randomly sampled distributions that were at least as skewed as the actual distribution.

7. References

- Akerboom, Jasper, Tsai-Wen Chen, Trevor J. Wardill, Lin Tian, Jonathan S. Marvin, Sevinç Mutlu, Nicole Carreras Calderón, et al. 2012. “Optimization of a GCaMP Calcium Indicator for Neural Activity Imaging.” *The Journal of Neuroscience: The Official Journal of the Society for Neuroscience* 32 (40): 13819–40.
- Alkema, Mark J., Melissa Hunter-Ensor, Niels Ringstad, and H. Robert Horvitz. 2005. “Tyramine Functions Independently of Octopamine in the *Caenorhabditis Elegans* Nervous System.” *Neuron* 46 (2): 247–60.
- Altun, Z.F. and Hall, D.H. 2021. Handbook of *C. elegans* Anatomy. In *WormAtlas* <http://www.wormatlas.org/hermaphrodite/hermaphroditehomepage.htm>
- Altun, Zeynep F., Bojun Chen, Zhao-Weng Wang, and David H. Hall. 2009. “High Resolution Map of *Caenorhabditis Elegans* gap Junction Proteins.” *Developmental Dynamics: An Official Publication of the American Association of Anatomists* 238 (8): 1936–50.
- Ayali, A., and R. M. Harris-Warrick. 1999. “Monoamine Control of the Pacemaker Kernel and Cycle Frequency in the Lobster Pyloric Network.” *The Journal of Neuroscience: The Official Journal of the Society for Neuroscience* 19 (15): 6712–22.
- Bargmann, C. I. 1998. “Neurobiology of the *Caenorhabditis Elegans* Genome.” *Science* 282 (5396): 2028–33.
- Ben Arous, Juliette, Sophie Laffont, and Didier Chatenay. 2009. “Molecular and Sensory Basis of a Food Related Two-State Behavior in *C. Elegans*.” *PloS One* 4 (10): e7584.
- Berman, Gordon J., William Bialek, and Joshua W. Shaevitz. 2016. “Predictability and Hierarchy in *Drosophila* Behavior.” *Proceedings of the National Academy of Sciences* 113 (42): 11943–48.
- Brenner, S. 1974. “The Genetics of *Caenorhabditis Elegans*.” *Genetics* 77 (1): 71–94.
- Brody, C. D. 1999. “Correlations without Synchrony.” *Neural Computation* 11 (7): 1537–51.
- Brown, T. G. 1914. “On the Nature of the Fundamental Activity of the Nervous Centres; Together with an Analysis of the Conditioning of Rhythmic Activity in Progression, and a Theory of the Evolution of Function in the Nervous System.” *The Journal of Physiology* 48 (1): 18–46.
- Bucher, Dirk, Gal Haspel, Jorge Golowasch, and Farzan Nadim. 2015. “Central Pattern Generators.” *eLS. John Wiley & Sons, Ltd: Chichester*, December. <https://doi.org/10.1002/9780470015902.a0000032.pub2>.
- Buzsáki, György, and Andreas Draguhn. 2004. “Neuronal Oscillations in Cortical Networks.” *Science* 304 (5679): 1926–29.
- Cáceres, Ivan de Carlos, Nicholas Valmas, Massimo A. Hilliard, and Hang Lu. 2012. “Laterally Orienting *C. Elegans* Using Geometry at Microscale for High-Throughput Visual Screens in Neurodegeneration and Neuronal Development Studies.” *PloS One* 7 (4): e35037.
- Calhoun, Adam J., Sreekanth H. Chalasani, and Tatyana O. Sharpee. 2014. “Maximally Informative Foraging by *Caenorhabditis Elegans*.” *eLife* 3 (December): e04220.
- C. elegans* Deletion Mutant Consortium. 2012. “Large-Scale Screening for Targeted Knockouts in the *Caenorhabditis Elegans* Genome.” *G3* 2 (11): 1415–25.
- Chalfie, M., J. E. Sulston, J. G. White, E. Southgate, J. N. Thomson, and S. Brenner. 1985. “The Neural Circuit for Touch Sensitivity in *Caenorhabditis Elegans*.” *Journal of Neuroscience* 5.
- Chalfie, M., and J. White. 1988. “The Nervous System.” In *The Nematode Caenorhabditis Elegans*, edited by W. B. Wood. Cold Spring Harbor, NY: Cold Spring Harbor Laboratory Press.
- Charlie, Nicole K., Michael A. Schade, Angela M. Thomure, and Kenneth G. Miller. 2006. “Presynaptic UNC-31 (CAPS) Is Required to Activate the G Alpha(s) Pathway of the *Caenorhabditis Elegans* Synaptic Signaling Network.” *Genetics* 172 (2): 943–61.
- Chartrand, Rick. 2011. “Numerical Differentiation of Noisy, Nonsmooth Data.” *International Scholarly Research Notices* 2011 (May). <https://doi.org/10.5402/2011/164564>.
- Chen, Beth L., David H. Hall, and Dmitri B. Chklovskii. 2006. “Wiring Optimization Can Relate Neuronal Structure and Function.” *Proceedings of the National Academy of Sciences of the United States of America* 103 (12): 4723–28.

- Chen, Tsai-Wen, Trevor J. Wardill, Yi Sun, Stefan R. Pulver, Sabine L. Renninger, Amy Baohan, Eric R. Schreiter, et al. 2013. "Ultrasensitive Fluorescent Proteins for Imaging Neuronal Activity." *Nature* 499 (7458): 295–300.
- Clemens, Stefan, Denis Combes, Pierre Meyrand, and John Simmers. 1998. "Long-Term Expression of Two Interacting Motor Pattern-Generating Networks in the Stomatogastric System of Freely Behaving Lobster." *Journal of Neurophysiology* 79 (3): 1396–1408.
- Cochella, Luisa, and Oliver Hobert. 2012. "Embryonic Priming of a miRNA Locus Predetermines Postmitotic Neuronal Left/right Asymmetry in *C. Elegans*." *Cell* 151 (6): 1229–42.
- Collins, Kevin M., and Michael R. Koelle. 2013. "Postsynaptic ERG Potassium Channels Limit Muscle Excitability to Allow Distinct Egg-Laying Behavior States in *Caenorhabditis Elegans*." *The Journal of Neuroscience: The Official Journal of the Society for Neuroscience* 33 (2): 761–75.
- Cook, Steven J., Travis A. Jarrell, Christopher A. Brittin, Yi Wang, Adam E. Bloniarz, Maksim A. Yakovlev, Ken C. Q. Nguyen, et al. 2019. "Whole-Animal Connectomes of Both *Caenorhabditis Elegans* Sexes." *Nature* 571 (7763): 63–71.
- Croll, Neil A. 1975. "Components and Patterns in the Behaviour of the Nematode *Caenorhabditis Elegans*." *Journal of Zoology* 176 (2): 159–76.
- Dawkins, Marian. 1971. "Perceptual Changes in Chicks: Another Look at the 'search Image' Concept." *Animal Behaviour* 19 (3): 566–74.
- Dawkins, Richard. 1976. "Hierarchical Organisation: A Candidate Principle for Ethology." *Growing Points in Ethology*. Oxford, England: Cambridge U Press.
- Delcomyn, F. 1980. "Neural Basis of Rhythmic Behavior in Animals." *Science* 210 (4469): 492–98.
- Deng, Lan, Jack E. Denham, Charu Arya, Omer Yuval, Netta Cohen, and Gal Haspel. 2021. "Inhibition Underlies Fast Undulatory Locomotion in *Caenorhabditis Elegans*." *eNeuro* 8 (2). <https://doi.org/10.1523/ENEURO.0241-20.2020>.
- Donnelly, Jamie L., Christopher M. Clark, Andrew M. Leifer, Jennifer K. Pirri, Marian Haburcak, Michael M. Francis, Aravinthan D. T. Samuel, and Mark J. Alkema. 2013. "Monoaminergic Orchestration of Motor Programs in a Complex *C. Elegans* Behavior." *PLoS Biology* 11 (4): e1001529.
- Edwards, Stacey L., Nicole K. Charlie, Marie C. Milfort, Brandon S. Brown, Christen N. Gravlin, Jamie E. Knecht, and Kenneth G. Miller. 2008. "A Novel Molecular Solution for Ultraviolet Light Detection in *Caenorhabditis Elegans*." *PLoS Biology* 6 (8): e198.
- Eisen, J. S., and E. Marder. 1984. "A Mechanism for Production of Phase Shifts in a Pattern Generator." *Journal of Neurophysiology* 51 (6): 1375–93.
- Eliav, Tamir, Maya Geva-Sagiv, Michael M. Yartsev, Arseny Finkelstein, Alon Rubin, Liora Las, and Nachum Ulanovsky. 2018. "Nonoscillatory Phase Coding and Synchronization in the Bat Hippocampal Formation." *Cell* 175 (4): 1119–30.e15.
- Faumont, S., T. H. Lindsay, and S. R. Lockery. 2012. "Neuronal Microcircuits for Decision Making in *C. Elegans*." *Current Opinion in Neurobiology* 22 (4): 580–91.
- Flavell, Steven W., Navin Pokala, Evan Z. Macosko, Dirk R. Albrecht, Johannes Larsch, and Cornelia I. Bargmann. 2013. "Serotonin and the Neuropeptide PDF Initiate and Extend Opposing Behavioral States in *C. Elegans*." *Cell* 154 (5): 1023–35.
- Fouad, Anthony D., Shelly Teng, Julian R. Mark, Alice Liu, Pilar Alvarez-Illera, Hongfei Ji, Angelica Du, et al. 2018. "Distributed Rhythm Generators Underlie *Caenorhabditis Elegans* Forward Locomotion." *eLife* 7: e29913.
- Fox, Lyle E., David R. Soll, and Chun-Fang Wu. 2006. "Coordination and Modulation of Locomotion Pattern Generators in *Drosophila* Larvae: Effects of Altered Biogenic Amine Levels by the Tyramine Beta Hydroxylase Mutation." *The Journal of Neuroscience: The Official Journal of the Society for Neuroscience* 26 (5): 1486–98.
- Fujiwara, Manabi, Piali Sengupta, and Steven L. McIntire. 2002. "Regulation of Body Size and Behavioral State of *C. Elegans* by Sensory Perception and the EGL-4 cGMP-Dependent Protein Kinase." *Neuron* 36 (6): 1091–1102.
- Gallagher, Thomas, Theresa Bjorness, Robert Greene, Young-Jai You, and Leon Avery. 2013. "The Geometry of Locomotive Behavioral States in *C. Elegans*." *PloS One* 8 (3): e59865.
- Gao, Shangbang, Sihui Asuka Guan, Anthony D. Fouad, Jun Meng, Taizo Kawano, Yung-Chi Huang, Yi Li, et al. 2018. "Excitatory Motor Neurons Are Local Oscillators for Backward Locomotion." *eLife* 7: e29915.

- Gendrel, Marie, Emily G. Atlas, and Oliver Hobert. 2016. "A Cellular and Regulatory Map of the GABAergic Nervous System of *C. Elegans*." *eLife* 5 (October): 1395.
- Gill, Robert E., T. Lee Tibbitts, David C. Douglas, Colleen M. Handel, Daniel M. Mulcahy, Jon C. Gottschalck, Nils Warnock, Brian J. McCaffery, Philip F. Battley, and Theunis Piersma. 2009. "Extreme Endurance Flights by Landbirds Crossing the Pacific Ocean: Ecological Corridor rather than Barrier?" *Proceedings. Biological Sciences / The Royal Society* 276 (1656): 447–57.
- Glaze, Christopher M., and Todd W. Troyer. 2006. "Temporal Structure in Zebra Finch Song: Implications for Motor Coding." *The Journal of Neuroscience*. US: Society for Neuroscience. <https://doi.org/10.1523/JNEUROSCI.3387-05.2006>.
- Gomez-Marin, Alex, Greg J. Stephens, and André E. X. Brown. 2016. "Hierarchical Compression of *Caenorhabditis Elegans* Locomotion Reveals Phenotypic Differences in the Organization of Behaviour." *Journal of the Royal Society, Interface / the Royal Society* 13 (121): 20160466.
- Gong, Jianke, Yiyuan Yuan, Alex Ward, Lijun Kang, Bi Zhang, Zhiping Wu, Junmin Peng, Zhaoyang Feng, Jianfeng Liu, and X. Z. Shawn Xu. 2016. "The *C. Elegans* Taste Receptor Homolog LITE-1 Is a Photoreceptor." *Cell* 167 (5): 1252–63.e10.
- Goodman, M. B., D. H. Hall, L. Avery, and S. R. Lockery. 1998. "Active Currents Regulate Sensitivity and Dynamic Range in *C. Elegans* Neurons." *Neuron* 20 (4): 763–72.
- Gordus, Andrew, Navin Pokala, Sagi Levy, Steven W. Flavell, and Cornelia I. Bargmann. 2015. "Feedback from Network States Generates Variability in a Probabilistic Olfactory Circuit." *Cell* 161 (2): 215–27.
- Goulding, Martyn. 2009. "Circuits Controlling Vertebrate Locomotion: Moving in a New Direction." *Nature Reviews. Neuroscience* 10 (7): 507–18.
- Goulding, Martyn. 2012. "Motor Neurons That Multitask." *Neuron*.
- Grant, Robyn A., Ben Mitchinson, Charles W. Fox, and Tony J. Prescott. 2009. "Active Touch Sensing in the Rat: Anticipatory and Regulatory Control of Whisker Movements during Surface Exploration." *Journal of Neurophysiology* 101 (2): 862–74.
- Gray, Jesse M., Joseph J. Hill, and Cornelia I. Bargmann. 2005. "A Circuit for Navigation in *Caenorhabditis Elegans*." *Proceedings of the National Academy of Sciences of the United States of America* 102 (9): 3184–91.
- Ha, Heon-Ick, Michael Hendricks, Yu Shen, Christopher V. Gabel, Christopher Fang-Yen, Yuqi Qin, Daniel Colón-Ramos, Kang Shen, Aravinthan D. T. Samuel, and Yun Zhang. 2010. "Functional Organization of a Neural Network for Aversive Olfactory Learning in *Caenorhabditis Elegans*." *Neuron* 68 (6): 1173–86.
- Haklai-Topper, Liat, Jürgen Soutschek, Helena Sabanay, Jochen Scheel, Oliver Hobert, and Elinor Peles. 2011. "The Neurexin Superfamily of *Caenorhabditis Elegans*." *Gene Expression Patterns: GEP* 11 (1-2): 144–50.
- Haley, Jessica A., David Hampton, and Eve Marder. 2018. "Two Central Pattern Generators from the Crab, *Cancer borealis*, Respond Robustly and Differentially to Extreme Extracellular pH." *eLife* 7 (December): e41877.
- Hardege, Iris, Julia Morud, Amy Courtney, and William R. Schafer. 2022. "A Novel and Functionally Diverse Class of Acetylcholine-Gated Ion Channels." *bioRxiv*. <https://doi.org/10.1101/2021.10.06.463318>.
- Harris-Warrick, Ronald M., Eve Marder, Allen I. Selverston, and Maurice Moulins, eds. 1992. "Dynamic Biological Networks: The Stomatogastric Nervous System." *Computational Neuroscience*. 328. <https://psycnet.apa.org/fulltext/1992-98791-000.pdf>.
- Hart, Anne C., Shannon Sims, and Joshua M. Kaplan. 1995. "Synaptic Code for Sensory Modalities Revealed by *C. Elegans* GLR-1 Glutamate Receptor." *Nature* 378 (6552): 82–85.
- Haspel, Gal, and Michael J. O'Donovan. 2011. "A Perimotor Framework Reveals Functional Segmentation in the Motoneuronal Network Controlling Locomotion in *Caenorhabditis Elegans*." *The Journal of Neuroscience: The Official Journal of the Society for Neuroscience* 31 (41): 14611–23.
- Haspel, Gal, Michael J. O'Donovan, and Anne C. Hart. 2010. "Motoneurons Dedicated to Either Forward or Backward Locomotion in the Nematode *Caenorhabditis Elegans*." *The Journal of Neuroscience: The Official Journal of the Society for Neuroscience* 30 (33): 11151–56.
- Hendricks, Michael, Heonick Ha, Nicolas Maffey, and Yun Zhang. 2012. "Compartmentalized Calcium Dynamics in a *C. Elegans* Interneuron Encode Head Movement." *Nature* 487 (7405): 99–103.

- Hills, Thomas, Penelope J. Brockie, and Andres V. Maricq. 2004. "Dopamine and Glutamate Control Area-Restricted Search Behavior in *Caenorhabditis Elegans*." *The Journal of Neuroscience: The Official Journal of the Society for Neuroscience* 24 (5): 1217–25.
- Hinde, R. A. 1953. "Appetitive Behaviour, Consummatory Act, and the Hierarchical Organisation of Behaviour: With Special Reference to the Great Tit (*Parus Major*)." *Behaviour* 5 (3): 189–224.
- Hobert, Oliver, Robert J. Johnston, and Sarah Chang. 2002. "Left–right Asymmetry in the Nervous System: The *Caenorhabditis Elegans* Model." *Nature Reviews. Neuroscience* 3 (8): 629–40.
- Hooper, S. L., and E. Marder. 1987. "Modulation of the Lobster Pyloric Rhythm by the Peptide Proctolin." *The Journal of Neuroscience: The Official Journal of the Society for Neuroscience* 7 (7): 2097–2112.
- Hums, Ingrid, Julia Riedl, Fanny Mende, Saul Kato, Harris S. Kaplan, Richard Latham, Michael Sonntag, Lisa Traunmüller, and Manuel Zimmer. 2016. "Regulation of Two Motor Patterns Enables the Gradual Adjustment of Locomotion Strategy in *Caenorhabditis Elegans*." *eLife* 5 (May): 1951.
- Jiang, Jingyuan, Yifan Su, Ruilin Zhang, Haiwen Li, Louis Tao, and Qiang Liu. 2022. "C. *Elegans* Enteric Motor Neurons Fire Synchronized Action Potentials Underlying the Defecation Motor Program." *Nature Communications* 13 (1): 1–15.
- Kaplan, Harris S., Oriana Salazar Thula, Niklas Khoss, and Manuel Zimmer. 2020. "Nested Neuronal Dynamics Orchestrate a Behavioral Hierarchy across Timescales." *Neuron* 105 (3): 562–76.e9.
- Katakura, N., L. Jia, and Y. Nakamura. 1995. "NMDA-Induced Rhythmical Activity in XII Nerve of Isolated CNS from Newborn Rats." *Neuroreport* 6 (4): 601–4.
- Kato, Saul, Harris S. Kaplan, Tina Schrödel, Susanne Skora, Theodore H. Lindsay, Eviatar Yemini, Shawn Lockery, and Manuel Zimmer. 2015. "Global Brain Dynamics Embed the Motor Command Sequence of *Caenorhabditis Elegans*." *Cell* 163 (3): 656–69.
- Kawano, Taizo, Michelle D. Po, Shangbang Gao, George Leung, William S. Ryu, and Mei Zhen. 2011. "An Imbalancing Act: Gap Junctions Reduce the Backward Motor Circuit Activity to Bias C. *Elegans* for Forward Locomotion." *Neuron* 72 (4): 572–86.
- Kiehn, Ole. 2011. "Development and Functional Organization of Spinal Locomotor Circuits." *Current Opinion in Neurobiology* 21 (1): 100–109.
- Kim, Kyuhyung, and Chris Li. 2004. "Expression and Regulation of an FMRFamide-Related Neuropeptide Gene Family in *Caenorhabditis Elegans*." *The Journal of Comparative Neurology* 475 (4): 540–50.
- Kleinfeld, David, Jeffrey D. Moore, Fan Wang, and Martin Deschênes. 2014. "The Brainstem Oscillator for Whisking and the Case for Breathing as the Master Clock for Orofacial Motor Actions." *Cold Spring Harbor Symposia on Quantitative Biology* 79: 29–39.
- Kocabas, Askin, Ching-Han Shen, Zengcai V. Guo, and Sharad Ramanathan. 2012. "Controlling Interneuron Activity in *Caenorhabditis Elegans* to Evoke Chemotactic Behaviour." *Nature* 490 (7419): 273–77.
- Kortlandt, A. 1956. "Aspects and Prospects of the Concept of Instinct." *Archives Néerlandaises de Zoologie* 11 (2): 155–284.
- Kurnikova, Anastasia, Jeffrey D. Moore, Song-Mao Liao, Martin Deschênes, and David Kleinfeld. 2017. "Coordination of Orofacial Motor Actions into Exploratory Behavior by Rat." *Current Biology: CB* 27 (5): 688–96.
- Laurent, Patrick, Zoltan Soltesz, Geoffrey M. Nelson, Changchun Chen, Fausto Arellano-Carbajal, Emmanuel Levy, and Mario de Bono. 2015. "Decoding a Neural Circuit Controlling Global Animal State in C. *Elegans*." *eLife* 4 (March): e04241.
- Lee, Harksun, Myung-Kyu Choi, Daehan Lee, Hye-Sung Kim, Hyejin Hwang, Heekyeong Kim, Sungsu Park, Young-Ki Paik, and Junho Lee. 2011. "Nictation, a Dispersal Behavior of the Nematode *Caenorhabditis Elegans*, Is Regulated by IL2 Neurons." *Nature Neuroscience* 15 (1): 107–12.
- Lindsay, Theodore H., Tod R. Thiele, and Shawn R. Lockery. 2011. "Optogenetic Analysis of Synaptic Transmission in the Central Nervous System of the Nematode *Caenorhabditis Elegans*." *Nature Communications* 2 (1): 1–9.
- Liu, He, Wenxing Yang, Taihong Wu, Fengyun Duan, Edward Soucy, Xin Jin, and Yun Zhang. 2018. "Cholinergic Sensorimotor Integration Regulates Olfactory Steering." *Neuron* 97 (2): 390–405.e3.
- Liu, Jie, Alex Ward, Jingwei Gao, Yongming Dong, Nana Nishio, Hitoshi Inada, Lijun Kang, et al. 2010. "C. *Elegans* Phototransduction Requires a G Protein–dependent cGMP Pathway and a Taste Receptor Homolog." *Nature Neuroscience* 13 (6): 715–22.
- Liu, Qiang, Philip B. Kidd, May Dobosiewicz, and Cornelia I. Bargmann. 2018. "C. *Elegans* AWA Olfactory Neurons Fire Calcium-Mediated All-or-None Action Potentials." *Cell* 175 (1): 57–70.e17.

- Li, Wei, Lijun Kang, Beverly J. Piggott, Zhaoyang Feng, and X. Z. Shawn Xu. 2011. "The Neural Circuits and Sensory Channels Mediating Harsh Touch Sensation in *Caenorhabditis Elegans*." *Nature Communications* 2: 315.
- Li, Zhaoyu, Jie Liu, Maohua Zheng, and X. Z. Shawn Xu. 2014. "Encoding of Both Analog- and Digital-like Behavioral Outputs by One *C. elegans* Interneuron." *Cell* 159 (4): 751–65.
- Loeb, J. 1918. "Forced Movements, Tropisms and Animal Conduct." <https://psycnet.apa.org › Record><https://psycnet.apa.org › Record>, Pp.209.
- Long, Michael A., Dezhe Z. Jin, and Michale S. Fee. 2010. "Support for a Synaptic Chain Model of Neuronal Sequence Generation." *Nature* 468 (7322): 394–99.
- Lorenzo, Ramiro, Michiho Onizuka, Matthieu Defrance, and Patrick Laurent. 2020. "Combining Single-Cell RNA-Sequencing with a Molecular Atlas Unveils New Markers for *Caenorhabditis Elegans* Neuron Classes." *Nucleic Acids Research* 48 (13): 7119–34.
- Luo, Linjiao, Quan Wen, Jing Ren, Michael Hendricks, Marc Gershow, Yuqi Qin, Joel Greenwood, et al. 2014. "Dynamic Encoding of Perception, Memory, and Movement in a *C. Elegans* Chemotaxis Circuit." *Neuron* 82 (5): 1115–28.
- Maier, Wolfgang, Bakhtiyor Adilov, Martin Regenass, and Joy Alcedo. 2010. "A Neuromedin U Receptor Acts with the Sensory System to Modulate Food Type-Dependent Effects on *C. Elegans* Lifespan." *PLoS Biology* 8 (5): e1000376.
- Marder, E., and J. S. Eisen. 1984. "Electrically Coupled Pacemaker Neurons Respond Differently to Same Physiological Inputs and Neurotransmitters." *Journal of Neurophysiology* 51 (6): 1362–74.
- Marder, Eve. 2011. "Variability, Compensation, and Modulation in Neurons and Circuits." *Proceedings of the National Academy of Sciences* 108 (supplement_3): 15542–48.
- Marder, Eve, and Dirk Bucher. n.d. "Central Pattern Generators and the Control of Rhythmic Movements" 11 (23): R986–96.
- Marder, Eve, Dirk Bucher, David J. Schulz, and Adam L. Taylor. 2001. "Invertebrate Central Pattern Generation Moves along" 15 (17): R685–99.
- Marques, João C., Simone Lackner, Rita Félix, and Michael B. Orger. 2018. "Structure of the Zebrafish Locomotor Repertoire Revealed with Unsupervised Behavioral Clustering." *Current Biology: CB* 28 (2): 181–95.e5.
- Marr, David. 1982. *Vision: A Computational Investigation into the Human Representation and Processing of Visual Information*. Oxford University Press.
- McIntire, S. L., E. Jorgensen, J. Kaplan, and H. R. Horvitz. 1993. "The GABAergic Nervous System of *Caenorhabditis Elegans*." *Nature* 364 (6435): 337–41.
- Moore, Jeffrey D., Martin Deschênes, Takahiro Furuta, Daniel Huber, Matthew C. Smear, Maxime Demers, and David Kleinfeld. 2013. "Hierarchy of Orofacial Rhythms Revealed through Whisking and Breathing." *Nature* 497 (7448): 205–10.
- Moore, Jeffrey D., David Kleinfeld, and Fan Wang. 2014. "How the Brainstem Controls Orofacial Behaviors Comprised of Rhythmic Actions." *Trends in Neurosciences* 37 (7): 370–80.
- Nakai, Junichi, Masamichi Ohkura, and Keiji Imoto. 2001. "A High Signal-to-Noise Ca²⁺ Probe Composed of a Single Green Fluorescent Protein." *Nature Biotechnology* 19 (2): 137–41.
- Nakamura, Y., N. Katakura, and M. Nakajima. 1999. "Generation of Rhythmical Ingestive Activities of the Trigeminal, Facial, and Hypoglossal Motoneurons in in Vitro CNS Preparations Isolated from Rats and Mice." *Journal of Medical and Dental Sciences* 46 (2): 63–73.
- Nguyen, Jeffrey P., Frederick B. Shipley, Ashley N. Linder, George S. Plummer, Mochi Liu, Sagar U. Setru, Joshua W. Shaevitz, and Andrew M. Leifer. 2016. "Whole-Brain Calcium Imaging with Cellular Resolution in Freely Behaving *Caenorhabditis Elegans*." *Proceedings of the National Academy of Sciences* 113 (8): E1074–81.
- Nichols, Annika L. A., Tomáš Eichler, Richard Latham, and Manuel Zimmer. 2017. "A Global Brain State Underlies *C. Elegans* Sleep Behavior." *Science* 356 (6344): eaam6851.
- Pattee, Howard. 1973. "Hierarchy Theory: The Challenge of Complex Systems." *The American Biology Teacher* 35 (7): 428–29.
- Pereira, Laura, Paschalis Kratsios, Esther Serrano-Saiz, Hila Sheftel, Avi E. Mayo, David H. Hall, John G. White, et al. 2015. "A Cellular and Regulatory Map of the Cholinergic Nervous System of *C. Elegans*." *eLife* 4: e12432.

- Pierce-Shimomura, Jonathan T., Beth L. Chen, James J. Mun, Raymond Ho, Raman Sarkis, and Steven L. McIntire. 2008. "Genetic Analysis of Crawling and Swimming Locomotory Patterns in *C. Elegans*." *Proceedings of the National Academy of Sciences* 105 (52): 20982–87.
- Piggott, Beverly J., Jie Liu, Zhaoyang Feng, Seth A. Wescott, and X. Z. Shawn Xu. 2011. "The Neural Circuits and Synaptic Mechanisms Underlying Motor Initiation in *C. Elegans*." *Cell* 147 (4): 922–33.
- Pirri, Jennifer K., and Mark J. Alkema. 2012. "The Neuroethology of *C. Elegans* Escape." *Current Opinion in Neurobiology* 22 (2): 187–93.
- Pirri, Jennifer K., Adam D. McPherson, Jamie L. Donnelly, Michael M. Francis, and Mark J. Alkema. 2009. "A Tyramine-Gated Chloride Channel Coordinates Distinct Motor Programs of a *Caenorhabditis Elegans* Escape Response." *Neuron* 62 (4): 526–38.
- Pokala, Navin, Qiang Liu, Andrew Gordus, and Cornelia I. Bargmann. 2014. "Inducible and Titratable Silencing of *Caenorhabditis Elegans* Neurons in Vivo with Histamine-Gated Chloride Channels." *Proceedings of the National Academy of Sciences* 111 (7): 2770–75.
- Powell, Daniel, Sara A. Haddad, Srinivas Gorur-Shandilya, and Eve Marder. 2021. "Coupling between Fast and Slow Oscillator Circuits in *Cancer Borealis* Is Temperature-Compensated." *eLife* 10 (February): e60454.
- Prevedel, Robert, Young-Gyu Yoon, Maximilian Hoffmann, Nikita Pak, Gordon Wetzstein, Saul Kato, Tina Schrödel, et al. 2014. "Simultaneous Whole-Animal 3D Imaging of Neuronal Activity Using Light-Field Microscopy." *Nature Methods* 11 (7): 727–30.
- Prinz, Astrid A., Vatsala Thirumalai, and Eve Marder. 2003. "The Functional Consequences of Changes in the Strength and Duration of Synaptic Inputs to Oscillatory Neurons." *Journal of Neuroscience* 23 (3): 943–54.
- Putrenko, Igor, Mahvash Zakikhani, and Joseph A. Dent. 2005. "A Family of Acetylcholine-Gated Chloride Channel Subunits in *Caenorhabditis Elegans*." *The Journal of Biological Chemistry* 280 (8): 6392–98.
- Raizen, David M., John E. Zimmerman, Matthew H. Maycock, Uyen D. Ta, Young-Jai You, Meera V. Sundaram, and Allan I. Pack. 2008. "Lethargus Is a *Caenorhabditis Elegans* Sleep-like State." *Nature* 451 (7178): 569–72.
- Ramot, Daniel, Brandon E. Johnson, Tommie L. Berry Jr, Lucinda Carnell, and Miriam B. Goodman. 2008. "The Parallel Worm Tracker: A Platform for Measuring Average Speed and Drug-Induced Paralysis in Nematodes." *PloS One* 3 (5): e2208.
- Rekling, J. C., and J. L. Feldman. 1998. "PreBötzing Complex and Pacemaker Neurons: Hypothesized Site and Kernel for Respiratory Rhythm Generation." *Annual Review of Physiology* 60: 385–405.
- Richards, Kathryn S., William L. Miller, and Eve Marder. 1999. "Maturation of Lobster Stomatogastric Ganglion Rhythmic Activity." *Journal of Neurophysiology* 82 (4): 2006–9.
- Ringstad, Niels, Namiko Abe, and H. Robert Horvitz. 2009. "Ligand-Gated Chloride Channels Are Receptors for Biogenic Amines in *C. Elegans*." *Science* 325 (5936): 96–100.
- Roberts, William M., Steven B. Augustine, Kristy J. Lawton, Theodore H. Lindsay, Tod R. Thiele, Eduardo J. Izquierdo, Serge Faumont, et al. 2016. "A Stochastic Neuronal Model Predicts Random Search Behaviors at Multiple Spatial Scales in *C. Elegans*." *eLife* 5: e12572.
- Ruijtenberg, Suzan, and Sander van den Heuvel. 2015. "G1/S Inhibitors and the SWI/SNF Complex Control Cell-Cycle Exit during Muscle Differentiation." *Cell* 162 (2): 300–313.
- Salvador, Liliana C. M., Frederic Bartumeus, Simon A. Levin, and William S. Ryu. 2014. "Mechanistic Analysis of the Search Behaviour of *Caenorhabditis Elegans*." *Journal of the Royal Society, Interface / the Royal Society* 11 (92): 20131092.
- Satterlie, R. A. 1985. "Reciprocal Inhibition and Postinhibitory Rebound Produce Reverberation in a Locomotor Pattern Generator." *Science* 229 (4711): 402–4.
- Savage, Patrick E., Psyche Loui, Bronwyn Tarr, Adena Schachner, Luke Glowacki, Steven Mithen, and W. Tecumseh Fitch. 2020. "Music as a Coevolved System for Social Bonding." *The Behavioral and Brain Sciences* 44 (August): e59.
- Schaffer, Evan S., Neeli Mishra, Matthew R. Whiteway, Wenzhe Li, Michelle B. Vancura, Jason Freedman, Kripa B. Patel, et al. 2021. "Flygenectors: The Spatial and Temporal Structure of Neural Activity across the Fly Brain." *bioRxiv*. <https://doi.org/10.1101/2021.09.25.461804>.
- Schmitt, Cornelia, Christian Schultheis, Navin Pokala, Steven J. Husson, Jana F. Liewald, Cornelia I. Bargmann, and Alexander Gottschalk. 2012. "Specific Expression of Channelrhodopsin-2 in Single Neurons of *Caenorhabditis Elegans*." *PloS One* 7 (8): e43164.

- Schrödel, Tina, Robert Prevedel, Karin Aumayr, Manuel Zimmer, and Alipasha Vaziri. 2013. “Brain-Wide 3D Imaging of Neuronal Activity in *Caenorhabditis Elegans* with Sculpted Light.” *Nature Methods* 10 (10): 1013–20.
- Seeds, Andrew M., Primoz Ravbar, Phuong Chung, Stefanie Hampel, Frank M. Midgley Jr, Brett D. Mensh, and Julie H. Simpson. 2014. “A Suppression Hierarchy among Competing Motor Programs Drives Sequential Grooming in *Drosophila*.” *eLife* 3 (August): e02951.
- Shen, Yu, Quan Wen, He Liu, Connie Zhong, Yuqi Qin, Gareth Harris, Taizo Kawano, et al. 2016. “An Extrasynaptic GABAergic Signal Modulates a Pattern of Forward Movement in *Caenorhabditis Elegans*.” *eLife* 5 (May). <https://doi.org/10.7554/eLife.14197>.
- Shtonda, Boris Borisovich, and Leon Avery. 2006. “Dietary Choice Behavior in *Caenorhabditis Elegans*.” *The Journal of Experimental Biology* 209 (Pt 1): 89–102.
- Shui, Yuan, Ping Liu, Haiying Zhan, Bojun Chen, and Zhao-Wen Wang. 2020. “Molecular Basis of Junctional Current Rectification at an Electrical Synapse.” *Science Advances* 6 (27): eabb3076.
- Simon, Herbert A. 1962. “The Architecture of Complexity.” *Proceedings of the American Philosophical Society* 106 (6): 467–82.
- Skora, Susanne, Fanny Mende, and Manuel Zimmer. 2018. “Energy Scarcity Promotes a Brain-Wide Sleep State Modulated by Insulin Signaling in *C. Elegans*.” *Cell Reports* 22 (4): 953–66.
- Smith, Jeffrey C., Howard H. Ellenberger, Klaus Ballanyi, Diethelm W. Richter, and Jack L. Feldman. 1991. “Pre-Bötzinger Complex: A Brainstem Region That May Generate Respiratory Rhythm in Mammals.” *Science* 254 (5032): 726–29.
- Sohal, Vikaas S., Feng Zhang, Ofer Yizhar, and Karl Deisseroth. 2009. “Parvalbumin Neurons and Gamma Rhythms Enhance Cortical Circuit Performance.” *Nature* 459 (7247): 698–702.
- Starich, Todd A., Ji Xu, I. Martha Skerrett, Bruce J. Nicholson, and Jocelyn E. Shaw. 2009. “Interactions between Innexins UNC-7 and UNC-9 Mediate Electrical Synapse Specificity in the *Caenorhabditis Elegans* Locomotory Nervous System.” *Neural Development* 4 (1): 16.
- Starich, Todd, Melissa Sheehan, Joy Jadrlich, and Jocelyn Shaw. 2009. “Innexins in *C. Elegans*.” *Cell Communication & Adhesion* 8 (4-6): 311–14.
- Sulston, J. E., and H. R. Horvitz. 1977. “Post-Embryonic Cell Lineages of the Nematode, *Caenorhabditis Elegans*.” *Developmental Biology* 56 (1): 110–56.
- Tarr, Bronwyn, Jacques Launay, Emma Cohen, and Robin Dunbar. 2015. “Synchrony and Exertion during Dance Independently Raise Pain Threshold and Encourage Social Bonding.” *Biology Letters* 11 (10). <https://doi.org/10.1098/rsbl.2015.0767>.
- Taylor, Seth R., Gabriel Santpere, Alexis Weinreb, Alec Barrett, Molly B. Reilly, Chuan Xu, Erdem Varol, et al. 2021. “Molecular Topography of an Entire Nervous System.” *Cell* 184 (16): 4329–47.e23.
- Tinbergen, Nikolaas. 1951. “The Study of Instinct.” *Oxford University Press* 115 (2990): 438–39.
- Towlson, Emma K., Petra E. Vértés, Sebastian E. Ahnert, William R. Schafer, and Edward T. Bullmore. 2013. “The Rich Club of the *C. Elegans* Neuronal Connectome.” *The Journal of Neuroscience: The Official Journal of the Society for Neuroscience* 33 (15): 6380–87.
- Turek, Michal, Ines Lewandrowski, and Henrik Bringmann. 2013. “An AP2 Transcription Factor Is Required for a Sleep-Active Neuron to Induce Sleep-like Quiescence in *C. Elegans*.” *Current Biology: CB* 23 (22): 2215–23.
- Uzel, Kerem, Saul Kato, and Manuel Zimmer. 2022. “A Set of Hub Neurons and Non-Local Connectivity Features Support Global Brain Dynamics in *C. Elegans*.” *Current Biology: CB* 32 (16): 3443–59.e8.
- Varshney, Lav R., Beth L. Chen, Eric Paniagua, David H. Hall, and Dmitri B. Chklovskii. 2011. “Structural Properties of the *Caenorhabditis Elegans* Neuronal Network.” *PLoS Computational Biology* 7 (2): e1001066.
- Venkatachalam, Vivek, Ni Ji, Xian Wang, Christopher Clark, James Kameron Mitchell, Mason Klein, Christopher J. Tabone, et al. 2016. “Pan-Neuronal Imaging in Roaming *Caenorhabditis Elegans*.” *Proceedings of the National Academy of Sciences* 113 (8): E1082–88.
- Vidal-Gadea, Andrés G., and Jonathan T. Pierce-Shimomura. 2012. “Conserved Role of Dopamine in the Modulation of Behavior.” *Communicative & Integrative Biology* 5 (5): 440–47.
- Vidal-Gadea, Andrés, Stephen Topper, Layla Young, Ashley Crisp, Leah Kressin, Erin Elbel, Thomas Maples, et al. 2011. “*Caenorhabditis Elegans* Selects Distinct Crawling and Swimming Gaits via Dopamine and Serotonin.” *Proceedings of the National Academy of Sciences of the United States of America* 108 (42): 17504–9.

- Von Stetina, S. E., R. M. Fox, K. L. Watkins, T. A. Starich, J. E. Shaw, and D. M. Miller. 2007. "UNC-4 Represses CEH-12/HB9 to Specify Synaptic Inputs to VA Motor Neurons in *C. Elegans*." *Genes & Development* 21 (3): 332–46.
- Von Stetina, Stephen E., Millet Treinin, and David M. Miller 3rd. 2006. "The Motor Circuit." *International Review of Neurobiology* 69: 125–67.
- Wakabayashi, Tokumitsu, Izumi Kitagawa, and Ryuzo Shingai. 2004. "Neurons Regulating the Duration of Forward Locomotion in *Caenorhabditis Elegans*." *Neuroscience Research* 50 (1): 103–11.
- Wang, Tianyan. 2015. "A Hypothesis on the Biological Origins and Social Evolution of Music and Dance." *Frontiers in Neuroscience* 9 (February): 30.
- Wang, Yuan, Xiaoqian Zhang, Qi Xin, Wesley Hung, Jeremy Florman, Jing Huo, Tianqi Xu, et al. 2020. "Flexible Motor Sequence Generation during Stereotyped Escape Responses." *eLife* 9 (June): 227–47.
- Welker, W. I. 1964. "Analysis of Sniffing of the Albino Rat." *Behaviour* 22 (3/4): 223–44.
- Wen, Quan, Michelle D. Po, Elizabeth Hulme, Sway Chen, Xinyu Liu, Sen Wai Kwok, Marc Gershow, et al. 2012. "Proprioceptive Coupling within Motor Neurons Drives *C. Elegans* Forward Locomotion." *Neuron* 76 (4): 750–61.
- Wever, Claudia M., Danielle Farrington, and Joseph A. Dent. 2015. "The Validation of Nematode-Specific Acetylcholine-Gated Chloride Channels as Potential Anthelmintic Drug Targets." *PloS One* 10 (9): e0138804.
- White, J. G., D. G. Albertson, and M. A. R. Anness. 1978. "Connectivity Changes in a Class of Motoneurone during the Development of a Nematode." *Nature* 271 (5647): 764–66.
- White, J. G., E. Southgate, J. N. Thomson, and S. Brenner. 1976. "The Structure of the Ventral Nerve Cord of *Caenorhabditis Elegans*." *Philosophical Transactions of the Royal Society of London. Series B, Biological Sciences* 275 (938): 327–48.
- White, J. G., E. Southgate, J. N. Thomson, and S. Brenner. 1986. "The Structure of the Nervous System of the Nematode *Caenorhabditis Elegans*." *Philosophical Transactions of the Royal Society of London. Series B, Biological Sciences* 314 (1165): 1–340.
- White, John. 2018. "Clues to Basis of Exploratory Behaviour of the *C. Elegans* Snout from Head Somatotropy." *Philosophical Transactions of the Royal Society of London. Series B, Biological Sciences* 373 (1758). <https://doi.org/10.1098/rstb.2017.0367>.
- Wilson, Donald M. 1961. "The Central Nervous Control of Flight in a Locust" 38 (2): 471–90.
- Wiltschko, Alexander B., Matthew J. Johnson, Giuliano Iurilli, Ralph E. Peterson, Jesse M. Katon, Stan L. Pashkovski, Victoria E. Abreira, Ryan P. Adams, and Sandeep Robert Datta. 2015. "Mapping Sub-Second Structure in Mouse Behavior." *Neuron* 88 (6): 1121–35.
- Winnier, A. R., J. Y. J. Meir, J. M. Ross, N. Tavernarakis, M. Driscoll, T. Ishihara, I. Katsura, and D. M. Miller. 1999. "UNC-4/UNC-37-Dependent Repression of Motor Neuron-Specific Genes Controls Synaptic Choice in *Caenorhabditis Elegans*." *Genes & Development* 13 (21): 2774–86.
- Witvliet, Daniel, Ben Mulcahy, James K. Mitchell, Yaron Meirovitch, Daniel R. Berger, Yuelong Wu, Yufang Liu, et al. 2021. "Connectomes across Development Reveal Principles of Brain Maturation." *Nature* 596 (7871): 257–61.
- Xu, Tianqi, Jing Huo, Shuai Shao, Michelle Po, Taizo Kawano, Yangning Lu, Min Wu, Mei Zhen, and Quan Wen. 2018. "Descending Pathway Facilitates Undulatory Wave Propagation in *Caenorhabditis Elegans* through Gap Junctions." *Proceedings of the National Academy of Sciences of the United States of America* 115 (19): E4493–4502.
- Yekutieli, Daniel, and Yoav Benjamini. 2001. "The Control of the False Discovery Rate in Multiple Testing Under Dependency." *Annals of Statistics* 29 (4): 1165–88.
- Yeon, Jihye, Jinmahn Kim, Do-Young Kim, Hyunmin Kim, Jungha Kim, Eun Jo Du, Kyeongjin Kang, Hyun-Ho Lim, Daewon Moon, and Kyuhung Kim. 2018. "A Sensory-Motor Neuron Type Mediates Proprioceptive Coordination of Steering in *C. Elegans* via Two TRPC Channels." *PLoS Biology* 16 (6): e2004929.
- Zimmer, Manuel, Jesse M. Gray, Navin Pokala, Andy J. Chang, David S. Karow, Michael A. Marletta, Martin L. Hudson, David B. Morton, Nikos Chronis, and Cornelia I. Bargmann. 2009. "Neurons Detect Increases and Decreases in Oxygen Levels Using Distinct Guanylate Cyclases." *Neuron* 61 (6): 865–79.